REPORT DOCUMENTATION PAGE	Form Approved OMB NO. 0704-0188

Public Reporting burden for this collection of information is estimated to average 1 hour per response, including the time for reviewing instructions, searching existing data sources, gathering and maintaining the data needed, and completing and reviewing the collection of information. Send comment regarding this burden estimates or any other aspect of this collection of information, including suggestions for reducing this burden, to Washington Headquarters Services, Directorate for information Operations and Reports, 1215 Jefferson Davis Highway, Suite 1204, Arlington, VA 22202-4302, and to the Office of Management and Budget, Paperwork Reduction Project (0704-0188,) Washington, DC 20503.

1. AGENCY USE ONLY (Leave Blank)	2. REPORT DATE March 2005	3. REPORT TYPE AND DATES COVERED Final Report April 1 2002-Sept. 30 2004

4. TITLE AND SUBTITLE Synthetic Multi-functional materials for Structural + Ballistic and blast Protection	5. FUNDING NUMBERS DAAD19-00-1-0511

6. AUTHOR(S)
Professor Kenneth S. Vecchio

7. PERFORMING ORGANIZATION NAME(S) AND ADDRESS(ES) The Regents of the University of California, Office of Contracts and Grants Department of Mechanical and Aerospace engineering 9500 Gilman Drive LaJolla, CA 92093-0411	8. PERFORMING ORGANIZATION REPORT NUMBER

9. SPONSORING / MONITORING AGENCY NAME(S) AND ADDRESS(ES) U. S. Army Research Office P.O. Box 12211 Research Triangle Park, NC 27709-2211	10. SPONSORING / MONITORING AGENCY REPORT NUMBER 41597.1-MS

11. SUPPLEMENTARY NOTES
The views, opinions and/or findings contained in this report are those of the author(s) and should not be construed as an official Department of the Army position, policy or decision, unless so designated by other documentation.

12 a. DISTRIBUTION / AVAILABILITY STATEMENT Approved for public release; distribution unlimited.	12 b. DISTRIBUTION CODE

13. ABSTRACT (Maximum 200 words)

This program was part of the DARPA program on Synthetic Multi-Functional Materials focused on structural plus ballistic and blast protection. During the first period of this program we have been focusing on developing both intrinsic and embedded functionality into a class of metal-intermetallic laminate (MIL) composites based on the Ti-Al system. These layered composites were initially developed as part of an Army MURI program at the University of CA, San Diego as a lightweight armor material. These MIL composites offer a unique combination of excellent specific mechanical properties such as high strength, high hardness, and high fracture toughness, with the ability to be formed into complex shaped penetration resistance structural materials. The addition of sensing, control, enhanced vibration damping, self-healing and possibly power generation could make these materials a valuable part of future defense systems.

14. SUBJECT TERMS			15. NUMBER OF PAGES
			16. PRICE CODE

17. SECURITY CLASSIFICATION OR REPORT **UNCLASSIFIED**	18. SECURITY CLASSIFICATION ON THIS PAGE **UNCLASSIFIED**	19. SECURITY CLASSIFICATION OF ABSTRACT **UNCLASSIFIED**	20. LIMITATION OF ABSTRACT **UL**

NSN 7540-01-280-5500

Standard Form 298 (Rev.2-89)
Prescribed by ANSI Std. 239-18
298-102

2

TABLE OF CONTENT   **PAGE**

LIST OF FIGURES

crack front shown here is nearly 2 mm ahead of the crack tip in the Ti layer (measured by the CP gage), suggesting tunneling of the cracks into the brittle Al$_3$Ti layer. The cross-section also shows extensive non-coplanar cracking and hence a dominant or single crack front is difficult to define. (b) The crack front at nearly 3 mm ahead of the apparent crack tip. The arrows indicate cracks that have tunneled through the brittle layer; only a few are identified. The images refer to the cross-section BB$^|$ in Figure 3-11. Similar sectioning of the sample further ahead of the crack tip revealed almost no cracking of the intermetallic phase.

Figure 3-10.   SEM images of fracture surface in the 33Ti laminate. (a) Fracture surfaces of Ti and Al$_3$Ti layers. (b) Ti-Al$_3$Ti interface. Observe the near interfacial cracking in the brittle phase. (c) The dotted curve separates the fatigue pre-cracked region from the monotonic fracture surface. A change from flat, transgranular crack growth to a more ductile dimpled failure can be observed in Ti layer. (d) predominantly mixed-mode intra-granular and intergranular fracture of Al$_3$Ti.

Figure 3-11.   Schematic diagram illustrating crack morphology variation due to orientation effects in laminate composites: (a) crack arrester orientation (b) crack divider orientation. Planes AA$^|$ and BB$^|$ indicate cross sections of the laminate composite near the crack tip (see Figure 3-9 and Figure 3-20). The arrows between the planes indicate bridging tractions over the length b.

Figure 3-12.   R-curve behavior under SSB and LSB conditions. (a) crack growth prior to reaching steady state bridging length. (b) crack growth and bridging ligaments after the attainment of steady state bridging length. (c) R-curve calculated under LSB conditions. (d) R-curve calculated under SSB conditions. Notice the saturation of R-curve under SSB to a steady state value, K_{SS}, compared to monotonically increasing function under LSB. K_N is the crack initiation toughness.

Figure 3-13.   Plots showing the LSB R-curve predictions (for a finite crack). The Ti volume fraction varied between 18% - 40%, indicated on the plots. The bridging length values used for the fit are given in Table 3-2. R-curve data for monolithic Ti-6-4 is also included in each plot for comparison.

Figure 3-14.   Plots showing the R-curve predictions under SSB conditions. The Ti volume fraction varied between 18% - 40%, indicated on the plots. The bridging length and specimen width values used for the fit are given in Table 3-2.

Figure 3-15.   The toughness values calculated from Equation 17 and 18 compared with those obtained from experiments (K_{COD} and K_{CP}) as a function of ductile phase volume fraction.

Figure 3-16.   Plots showing the effects of LSB on the R-curve behavior. The SSB R-curve is also drawn for comparison.

LIST OF TABLES

Statement of Problem Studied

The problem studied was the development of multi-functional versions of metallic-intermetallic laminate composites that possessed attractive structural and ballistic performance, while also incorporating functions such as impact detection, impact location determination, vibration damping, damage detection, etc.

Summary of the Most Important Results

We successfully developed methods and technologies for incorporating a large number of different embedded functionalities into these metallic-intermetallic laminate composites, while optimizing the large scale production methods for these laminates, and finding approaches to enhance the ballistic resistance of these materials.

Listing of All Publications and Technical Reports supported under this Contract

(a) Papers published in peer-reveiwed journals

1. T. Li, F. Grignon, D. Benson, K. Vecchio, E. Olevsky, M. Meyers, Modeling the elastic properties and damage evolution in Ti-6-4-Al_3Ti metal intermetallic laminate (MIL) composites, Material Science and Engineering A, 2004, 374: 10-26.

2. Rohatgi, A., Vecchio, K.S., Nguyen, P., Kosmatka, J.B., "Development of Vibration Damping Techniques in Metallic-Intermetallic Laminate (MIL) Composites," Presented in the symposium on materials processing and manufacturing: Processing and Properties of Lightweight Cellular Metals and Structures, TMS annual meeting, February 17-21, 2002, Seattle, Washington. Processing and Properties of Lightweight Cellular Metals and Structures, eds. A. Ghosh, T. Sanders and D. Claar, p. 288.

3. Kosmatka, J.B. and P. Nguyen; "Detecting Impact Damage and Location in Multifunctional Metallic-Intermetallic Laminate (MIL) Composites," Proceedings of Structural Health Monitoring 2003, Stanford, CA, 2003, pp. 1-8.

4. Raghavendra R. Adharapurapu, Kenneth S. Vecchio, Fengchun Jiang, Aashish Rohatgi, "Effects Of Ductile Laminate Thickness, Volume Fraction And Orientation On Fatigue-Crack Propagation In Ti-Al_3ti Metal-Intermetallic Laminate (Mil) Composites" Metallurigical and Materials Transaction A, in press.

5. Fengchun Jiang, Aashish Rohatgi, Kenneth S. Vecchio[*] and Justin L. Cheney, Analysis of the Dynamic Responses for A Pre-cracked Three-point Bend Specimen, International Journal of Fracture, (2004)

6. Fengchun Jiang, Kenneth Vecchio, Aashish Rohatgi, Analysis of Modified Split Hopkinson Pressure bar Dynamic Fracture Test Using an Inertia Model, International Journal of Fracture, 126: 143-164, (2004).

7. Fengchun Jiang, Aashish Rohatgi, Kenneth Vecchio, Raghavendra R. Adharapurapu, Crack Length Calculation for Bend Specimens under Static and Dynamic Loading, Engineering Fracture Mechanics, 71 (2004) 1971-1985.

8. Aashish Rohatgi, David J. Harach, Kenneth S. Vecchio, and Kenneth P. Harvey, "Resistance-curve and fracture behavior of Ti-Al_3Ti metallic-intermetallic laminate (MIL) composites" Acta Materialia, Vol. 51 (2003) 2933-2957.

9. Kenneth S. Vecchio, "Synthetic Multi-Functional Metallic-Intermetallic Laminate (MIL) Composites" Journal of Metal, March 2005

10. Raghavendra R. Adharapurapu, Kenneth S. Vecchio, Aashish Rohatgi, Fengchun Jiang, "Fracture Of Ti-Al_3ti Metal-Intermetallic Laminate (Mil) Composites: Effects Of Lamination On R-Curve Behavior" Metallurgical and Materials Transaction A, in press.

(b) Papers published in non-peer reviewed journals or in conference proceedings

A. Rohatgi, J.B. Kosmatka, K.S. Vecchio, K.P. Harvey, P. Nguyen, and D.J. Harach "Development of Multifunctional Metallic-Intermetallic Laminate (MIL) Composites with Particulate-based Damping" <u>Proceedings of the 16th Annual Technical Conference of the American Society for Composites</u>, September 9-12, 2001, Virginia Tech.

(c) Papers presented at meetings, but not published in conference proceedings

1. SAMPE talk, San Diego, 2004, Mechanical Behavior Of Ti-6-4-Al$_3$ti Metal Intermetallic Laminate (Mil) CompositeS, T. Li, K. Vecchio, E. Olevsky, M. Meyers.

2. TMS talk, SF, 2005, An investigation of mechanical behavior and damage evolution in Ti-Al$_3$Ti metal intermetallic laminate (MIL) composites. T. Li, K. Vecchio, E. Olevsky, M. Meyers.

(d) Manuscripts submitted, but not published

1. Nguyen, P, J. B. Kosmatka, and K. Vecchio; "Passive Vibration Damping in Multifunctional Metallic-Intermetallic Laminates Using an Embedded Particle Impact Damper," <u>Journal of Composite Materials,</u> (submitted).

2. Nguyen, P, and J. B. Kosmatka; "An Improved Analytical Model for Embedded Particle Vibration Dampers," <u>Journal of Sound and Vibration,</u> (submitted).

3. Nguyen, P, J. B. Kosmatka, K. Vecchio; "Using Embedded Sensors to Detect Impact Damage and Location in Multifunctional Metallic-Intermetallic Laminates," <u>Journal of Smart Materials and Structures,</u> (submitted).

4. Nguyen, P, J. B. Kosmatka, and K. Vecchio; "Passive Vibration Damping in Multifunctional Metallic-Intermetallic Laminates Using an Embedded PZT Shunt Circuit," <u>Journal of Composite Materials,</u> (to be submitted).

5. Technical reports submitted to ARO

1. "Synthetic Multi-Functional Materials for Structural plus Blast and Ballistic Protection" Year III Interim Progress Report for Contract Number DAAD19-00-1-0511, February 2003
2. "Synthetic Multi-Functional Materials for Structural plus Blast and Ballistic Protection" Year II Interim Progress Report for Contract Number DAAD19-00-1-0511, March 2002
3. "Synthetic Multi-Functional Materials for Structural plus Blast and Ballistic Protection" Year I Interim Progress Report for Contract Number DAAD19-00-1-0511, March 2001

List of All Participating scientific personnel showing advanced degrees earned by them while employed on the project

      (a) T. Li, Ph.D. expected 2005

      (b) Raghavendran Adharapurupu, M.S. 2003

      (c) Phu Nguyyen, M.S. 2003

Report of Inventions (by Title only)

1. DESIGN AND FABRICATION OF CONFINED METAL-INTERMETALLIC LAMINATE COMPOSITES.

2. CREATING A HARD, WEAR, AND CORROSION RESISTANT SURFACE LAYER FOR METAL ALLOYS.

3. DESIGN AND FABRICATION OF VIBRATION-DAMPED MATERIALS.

4. FABRICATION TECHNIQUE FOR EMBEDDING SENSORS IN METALLIC MATERIALS.

INTRODUCTION TO FINAL REPORT

This report summaries and details the research conducted at UC San Diego, under the direction of Professor Kenneth S. Vecchio, on Metallic-Intermetallic Lamiante (MIL) Composites, funded under the DARPA program entitled "Synthetic Multi-Functional Materials". This research was focused on three main aspects of these novel laminate composites: (1) Structural properties of MIL Composites (primarily strength, stiffness, fracture toughness, and fatigue behavior), (2) Embedded functionalities to enhance the utility of these materials for high performance application of interest to the DoD, and (3) Embedded sensors for active evaluation of impact locations and impact magnitude.

This report is divided into several different sections to address each of these areas of focus. Section 1is an overview of many of the attractive properties of MIL composites as well as various embedded features we developed in these MIL composites that have been investigated in this research program. Section 2 is an in-depth discussion of the fatigue behavior of these MIL composites with emphasis on relationships between volume fractions of the metal and intermetallic layers, thickness of the layers, and the orientation of the layers with respect to the crack plane and the fracture resistance of the composites. Comparison of the fatigue resistance of the MIL composites with respect to other typical engineering materials is also included. Section 3 of the report addresses the measurement of fracture toughness in these MIL composites, again with emphasis on relationships between volume fractions of the metal and intermetallic layers, thickness of the layers, and the orientation of the layers with respect to the crack plane and the fracture resistance of the composites. Due to the metal layers bridging the crack opening regions leading to enhanced fracture resistance, a detailed analysis of small-scale and large-scale bridging effects is presented to allow proper assessment of the apparent fracture toughness of these materials. Lastly, Section 4 presents a summary of our work on embedded sensors in these MIL composites. This section discusses the methods for embedding the sensors, and techniques for measuring the response from the sensors for impact location determination as well as impact magnitude assessment.

SECTION 1: OVERVIEW OF SYNTHETIC MULTI-FUNCTIONAL METALLIC-INTERMETALLIC LAMIANTE COMPOSITES

INTRODUCTION

The field of material microstructural design to achieve a set of targeted mechanical + functional properties has become a mainstay of new material development strategies.   Structural materials, which by their very nature are intended to carry mechanical loads in service, can be designed to provide additional performance enhancing functions through tailoring of meso-, micro-, or nano-structures.   Structural materials with these performance-enhancing capabilities have been termed "Synthetic Multi-functional Materials" [1].   Structural composites, by their multi-phase nature, offer many opportunities for the design of performance enhancing multi-functional materials. Recently, a new class of structural materials has been developed at the University of CA, San Diego, termed 'Metallic-Intermetallic Laminate (MIL) Composites [2].   The goal of this materials development effort was to extrapolate upon the positive engineering properties exhibited by hierarchical multiphase complex natural composites such as shells [3,4], to design and synthesize multi-functional composites tailored to optimize specific structural properties, while facilitating low cost, designable and functional microstructures.

Biological systems often exhibit a wide array of multi-functional materials, and offer great biomimetic motivation to develop synthetic multi-functional materials. For example, mollusk shells are known to possess hierarchical structures highly optimized for toughness.   The two mollusks that have been studied most extensively are Haliotis rufescens (abalone) and Pinctata (conch) shells. Considering the weak constituents the shells are made from – namely calcium carbonate ($CaCO_3$) and a series of organic binders, the mechanical properties of these shells are outstanding.   Their tensile strength varies between 100 and 300 MPa, and fracture toughness between 3 and 7 MPa-m$^{1/2}$. $CaCO_3$ has corresponding strength and toughness values of 30 MPa and < 1 MPa-m$^{1/2}$, respectively [5-9].   These mollusks owe their extraordinary mechanical properties to a hierarchically organized structure starting with single crystals of $CaCO_3$, with dimensions of 4~5 nm (nanostructure), and proceeding with "bricks" with dimensions of 0.5~10μm (microstructure, see Figure 1-1a), and finishing with layers of ~0.2-0.5 mm (mesostructure, see Figure 1b).

16

By building on the laminate microstructure design found in shells, metallic-intermetallic (Ti-Al$_3$Ti) laminate (MIL) composites have been produced to mimic these structures from elemental titanium and aluminum foils by a novel one-step process utilizing a controlled reaction at elevated temperature and pressure [2]. The novelty of this fabrication process lies in the fact that it is performed in open air and produces a fully dense laminate composite. Figure 1-2 shows an illustration of the processing setup for fabrication of the MIL composites using a simple open-air heated platen press. The thickness of the original titanium and aluminum foils is chosen to ensure that the entire aluminum layer is consumed upon reaction with the adjacent titanium layers. Such a layering scheme results in a composite with alternate layers of Al$_3$Ti (to mimic the hard CaCO$_3$ layers in shells) and residual Ti (to mimic the tough protein layers in shells), and the thickness of the final layers are dependent upon the thickness of the original Ti and Al foils. The above process is highly flexible since metal/alloy foils other than Ti can be used individually, or in combination, within the same composite, to produce their respectivmetal/metal-aluminide combinations. For example, MIL composites using Fe-based, Ni-based, and Co-based alloys as the starting metal layer (instead of Ti) have been successfully fabricated using the above technique. The MIL composites produced by this method are not hierarchical structures in the manner that natural shells are, but are rather 2-D laminate structures, in which the scale of the layering can be controlled, tailored, sub-divided, and compositionally altered to achieve a set of desired properties and functions.

(a)   (b)
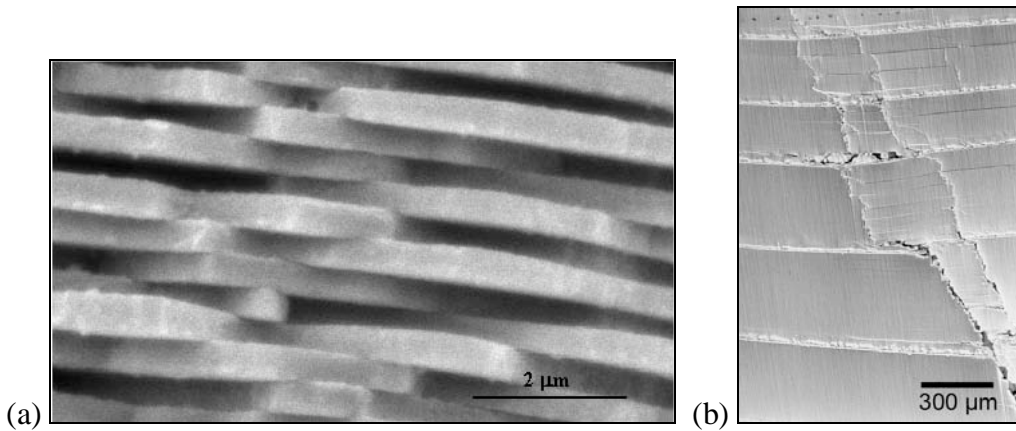
Figure 1-1. (a) SEM micrograph of fracture surface of an abalone shell showing the individual hexagonal aragonite tiles comprising the microstructure. (b) Optical micrograph of the mesoscale laminate structure of the abalone shell in a bend fracture sample showing the crack deflection achieved in this multi-layered material.

The composition, physical, and mechanical properties of the MIL composites can be varied and tailored within the thickness of the composite by simply varying the individual foil compositions, thickness, and layering sequence. The fabrication of metallic-intermetallic laminate (MIL) composites using this approach has several key advantages that make it ideally suited for the production of commercially-scalable structural materials, as well as microstructures designed for specific functionalities.

1. Since the initial materials utilized are in the form of commercially available metallic foils, the initial material cost is reasonably low, compared to many of the exotic material processing routes that are commonly pursued in small-scale research environments. This also means that a wide array of compositions can be ready produced, although for this paper we will focus on the Ti-Al system because of their high specific properties.

2. The use of initially ductile metallic foils enables the layers to be formed into complex shapes. This opens the door for non-planar structures, such as rods, tubes, shafts, and cones, as well as simple machining of individual foils for complex, 3-dimensional structures, and near-net shape forming of parts. The use of initial metallic foils also allows the individual foils to be machined to contain cavities and pathways facilitating the incorporation of embedded functionalities, such as passive damping [5] or sensors, prior to processing.

3. The processing conditions, in terms of temperature, pressure and atmosphere are very modest. Processing temperatures, in the case of Al-foil containing samples are below 700°C, and the processing pressures are below 4 MPa [2]. Perhaps the most remarkable feature of the processing of these metallic-intermetallic laminate composites is that the processing is carried out in open air, no special inert gas or vacuum chamber facilities are necessary. The combination of these various processing features makes the processing method itself very low cost, allows for complex shape fabrication and is easily amenable to computer control.

4. The microstructure of the metallic-intermetallic laminate composites is determined by the foil thickness and composition and the processing condition. Since the material make-up is based on the selection of the metal foils, it is possible to completely tailor the microstructure from one surface to the other. In addition, the physical and mechanical properties of the

MIL composites can be tailored by selection of the foil composition and thickness making the MIL composite material system ideally suited for engineering the microstructure to achieve the specific performance goals.
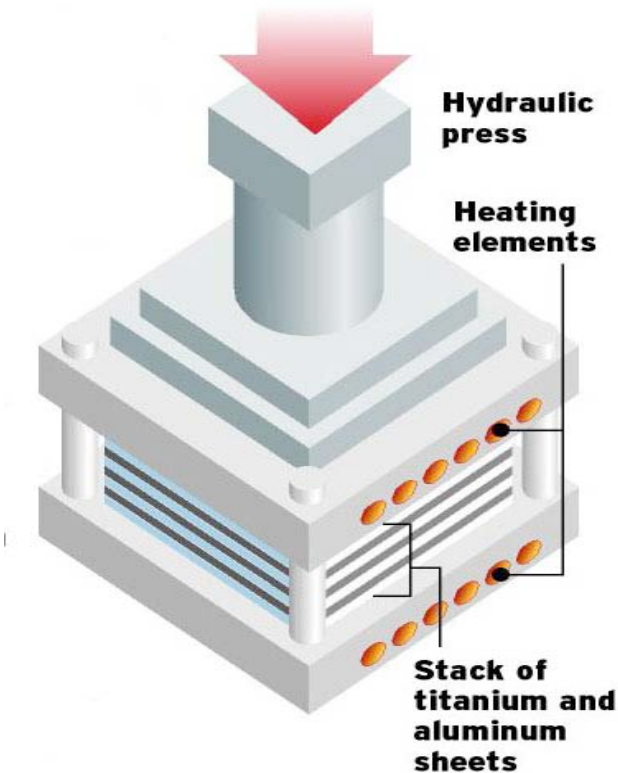
Figure 1-2.   Illustration of metallic-intermetallic laminate composite heated platen press apparatus for fabrication of planar laminates. Complex platen designs can be used to fabricate 3-D, near net-shape MIL composites in the same one-step, open-air operation.

Of the various possible aluminides in the Ti-Al system, the formation of the intermetallic Al_3Ti is thermodynamically and kinetically favored over the formation of other aluminides when reacting Al directly with Ti. This preferential formation of Al_3Ti is fortuitous as its Young's modulus (216 GPa) and oxidation resistance are higher, and the density (3.3 g/cm^3) lower than that of the other titanium aluminides such as Ti_3Al and TiAl [10]. The high compressive strength and stiffness of Al_3Ti (and intermetallics, in general) result from their high bond strength.   However, intermetallics are brittle at low temperatures due to the limited mobility of dislocations (and paired superdislocations with anti-phase boundaries), insufficient number of

slip or twinning systems, and/or very low surface energy resulting in little to no plastic deformation at crack tips. For example, Al_3Ti is extremely brittle at room temperature and has a very low fracture toughness of ~2 MPa√m [11].

The unique properties of MIL composites arise from the combination of the high hardness and stiffness of the intermetallic-aluminide phase alternatively layered with the high strength, toughness, and ductility of metal alloys. Figure 1-3 shows two examples of the microstructure of Ti-Al_3Ti MIL composites with significantly different layer thickness.
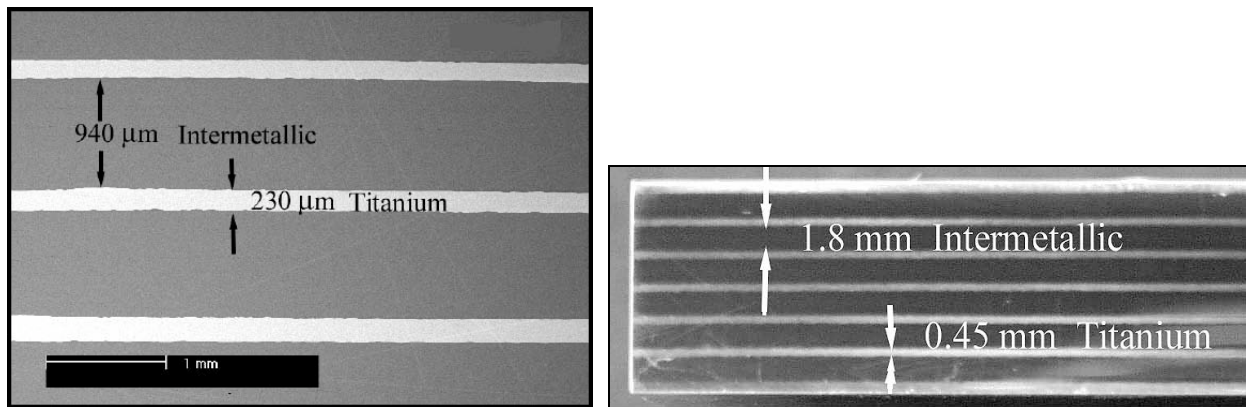
Figure 1-3. Microstructures typical of Ti-Al_3Ti MIL composites.

STRUCTURAL PERFORMANCE ATTRIBUTES

In the case of Ti-Al_3Ti MIL composites, the specific stiffness (modulus/density) is nearly twice that of steel, the specific toughness and specific strength are similar or better than nearly all metallic alloys, and specific hardness is on par with many ceramic materials. An interesting comparison of material properties for the MIL Composites can be obtained using a material property map. Figure 1-4 shows a plot having as the x-axis the specific modulus of a material on a log scale and the y-axis the specific compressive strength on a log scale. In this plot numerous material locations are shown, and in terms of optimizing these properties (combined compressive strength and stiffness), the upper right-hand corner represents the goal. The location of the MIL composites (red ellipse) is shown to the right (higher specific modulus) of the typical structural metals such as steels, Ti alloys, Ni-superalloys, Al-alloys, and Ti-based intermetallics. The only metallic materials of higher specific stiffness are the beryllium alloys. Several ceramic materials

are shown, which have higher specific stiffness than the MIL composites, including SiC, B_4C, Al_2O_3, and diamonds. Clearly, the MIL composites possess tremendous potential for structural applications, particularly for demanding high specific stiffness applications.

The good fracture toughness of the MIL composites is derived from the combination of the highly anisotropic layered structure of the material and the need for crack re-initiation at each successive metal layer. Figure 1-5a shows an example the fracture behavior of three different volume fraction Ti-Al₃Ti MIL composites. In samples with as little as 20% remnant Ti, the crack cannot propagate through the samples without being diverted and bifurcated at each Ti metal layer. Figure 1-5b shows a plot of the fatigue crack growth curves for Ti-Al₃Ti MIL composites having different volume fractions of intermetallic phase. The crack growth curves for these MIL composites very closely overlap similar data for monolithic Ti alloys such as Ti-6-4. Since the MIL composites have higher stiffness and lower density that the monolithic Ti alloys, with similar crack growth resistance, enhanced performance can be obtained for demanding aerospace applications.
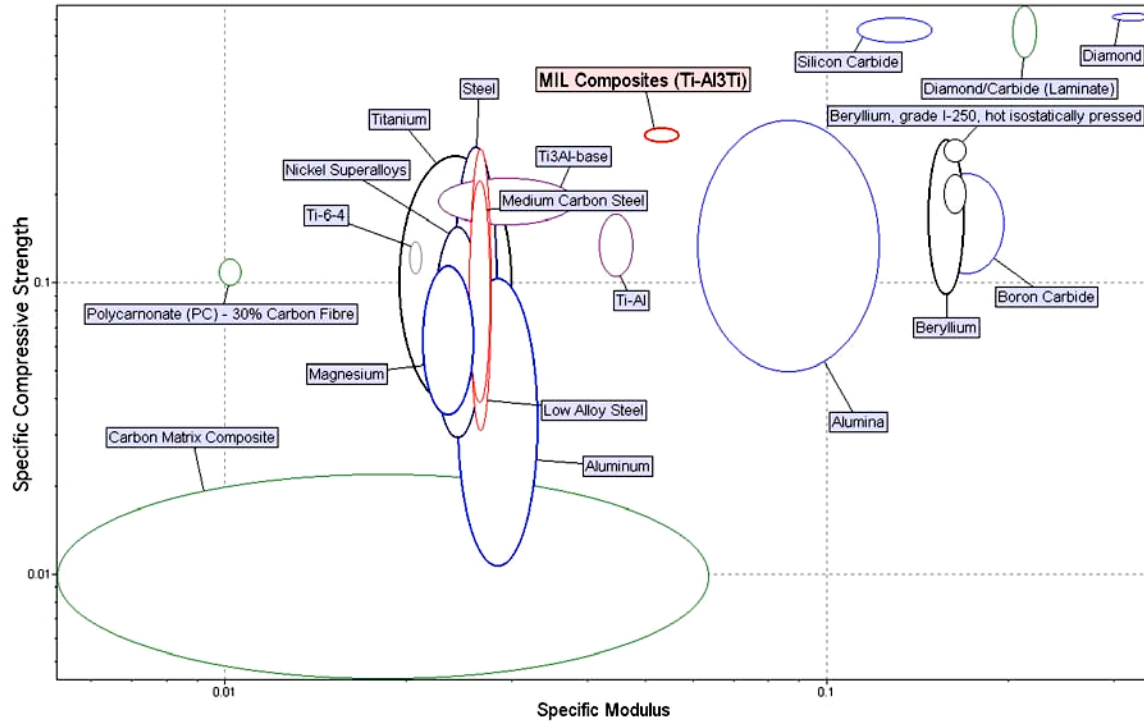
Figure 1-4.   Materials property map comparing specific compressive strength versus specific material stiffness.

Figure 1-6 plots the specific fracture toughness vs. the specific modulus of various engineering materials, including the MIL composites (shown by the dark grey ellipse). Several other laminates are identified as light gray region in Figure 1-6. It can be seen that the Ti/Al$_3$Ti laminate composites have higher specific toughness than other laminate systems and the Ti/Al$_3$Ti specific modulus is surpassed only by the metal/Al$_2$O$_3$ system. Relative to γ-TiAl/TiNb, MIL composites have higher specific fracture toughness and a higher specific modulus for the same volume fraction of the ductile phase. Further, relative to the various metal/Al$_2$O$_3$ systems, the MIL composites have higher specific fracture toughness for the same volume fraction of the ductile phase. Thus, owing to the ease of fabrication of Ti/Al$_3$Ti laminates, low fabrication costs, and their attractive mechanical properties, MIL (Ti/Al$_3$Ti) composites are an excellent candidate for engineering applications requiring a combination of low density, high strength, high toughness and high stiffness.
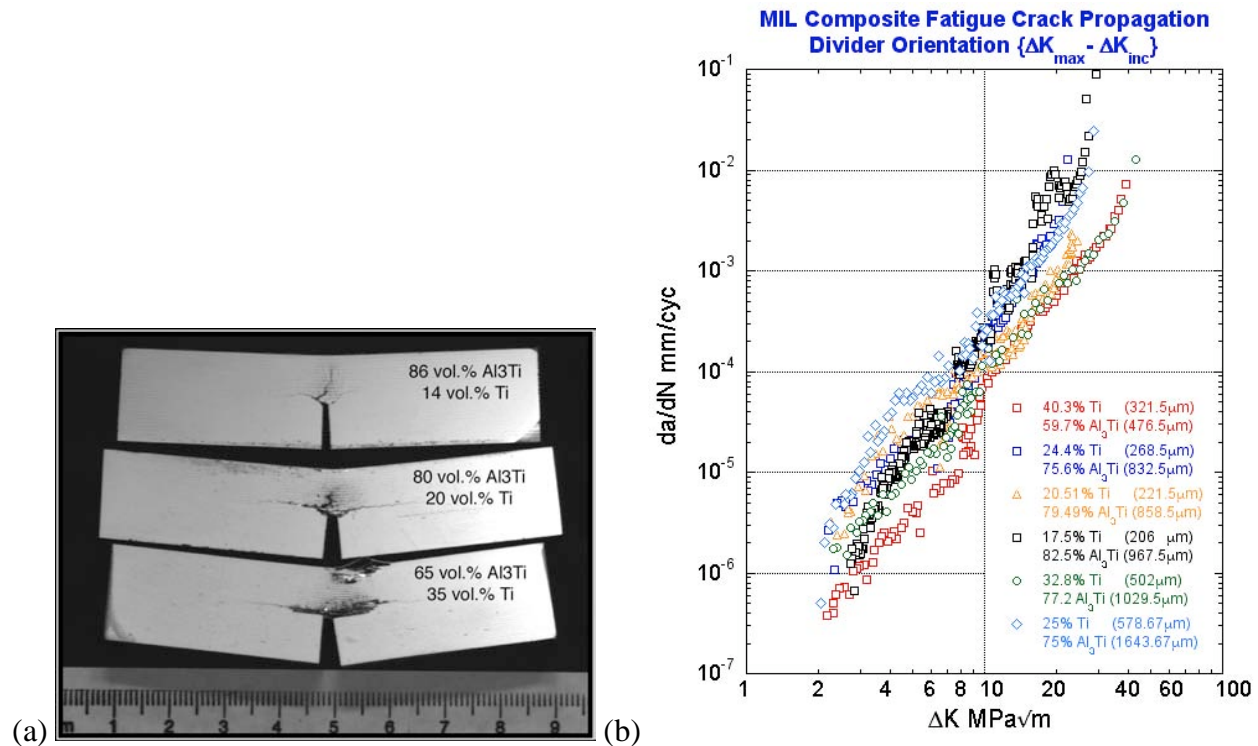
Figure 1-5. (a) Quasi-Static Three-point bend Samples for Fracture Toughness Measurements, and (b) fatigue crack growth curves for various MIL composites.

STRUCTURAL PLUS BALLISTIC ATTRIBUTES

The above discussion on the specific physical and mechanical properties of the MIL composites makes them an attractive material for structural applications. However, the ballistic performance of these materials is also quite impressive, when compared on the basis of areal density for a given threat, against other structural materials. Figure 1-7 shows a photograph of a cross-section through the impact location from a ballistic test on a MIL composite. The sample is a 20% Ti-6-4 and 80% Al_3Ti laminate with an initial thickness of approximately 2 cm. This composition produces a sample with a density of 3.5 g/cm^3 and therefore the specific target shown in this figure would have an areal density of 7 g/cm^2. The penetrator used was a tungsten heavy alloy rod (93W-7FeCo) with a mass of approx. 10 grams and initial diameter of 6.15 mm, and the penetrator was fired at a velocity of 900 m/s (2950 ft/s) at the target in a normal incidence depth-of-penetration (DOP) orientation. The depth of penetration within the MIL target is less than 1 cm. The demonstrated mechanical properties of the MIL composites make them suitable for structural application, while the ballistic performance makes them attractive for armor applications, creating a multi-functional (structural + ballistic) material. The ballistic performance of these MIL composites can be further enhanced by the incorporation of harder constituent phases, such as ceramics. MIL composites have been successfully fabricated using Al-based ceramic particulate reinforced metal-matrix composites (MMCs), as well as direct incorporation of ceramic fibers and ceramic disks and plates within the intermetallic layer by layering the ceramics between Al sheets prior to reaction sintering of the MIL composites.

STRUCTURAL PLUS THERMAL MANAGEMENT ATTRIBUTES

For applications such as structural heat sinks, a high performing material must possess the structural attributes described above, in addition to a high specific heat capacity to store the thermal energy and a high thermal conductivity to transport the heat throughout the structural heat sink. Figure 7 shows a plot of the product of thermal conductivity and specific heat capacity (on the y-axis) versus the product of specific modulus and fracture toughness (on the x-axis). The product of specific modulus and fracture toughness was chosen because it represents an optimum for many structural applications wherein high stiffness and high fracture toughness are

desired. This combination of properties is usually difficult to achieve considering the highest stiffness materials, such as ceramics, usually possess the lowest fracture toughness. In terms of thermal management properties, the highest stiffness materials, such as ceramics, are usually poor thermal conductors, and the high thermal conductivity materials such as Al-alloys and Cu-alloys, have relatively low specific stiffness. The exception to these trends is beryllium alloys, which possess high specific stiffness, high thermal conductivity and high heat capacity. On the other hand, Be alloys have significant drawbacks to their widespread use, such as the limited availability of Be, the high cost of Be alloys, and the serious health concerns with Be manufacturing. As such, alternatives to Be alloys for combined structural plus thermal management applications are in great demand. Examination of Figure 8 shows that MIL composites are second only to Be alloys, in terms of thermal management capacity, for an equivalent structural property level. In terms of thermal management capacity, the MIL composites are only surpassed by Be-alloys, some Al-alloys, and diamond. Given the high cost of diamonds and the inability to produce structural components from them, we can eliminate diamonds as a choice. Furthermore, the specific structural performance of MIL composites is nearly 3 times greater than Al-alloys, which can be critical for high performance aerospace applications. As such, Ti-Al MIL composites offer an attractive alternative to Be alloys for structural heat sink (multi-functional structural + thermal) applications.

MULTI-FUNCTIONAL METALLIC-INTERMETALLIC LAMINATE (MIL) COMPOSITES

In addition to the multi-functional nature of MIL composites described above, it is possible to incorporate additional functionalities into the materials. These functionalities are readily incorporated into the MIL composites due to the layer-by-layer assembly nature to the materials. Since each layer of the MIL composite starts out as a metal foil, it is possible to create holes and slits in these layers forming 'open space' in individual layers or multiple layers. Within these cavities and slits, additional functionalities can be embedded to further enhance the properties of the MIL composites. The approach follows, to some extent, a multi-layer electronic circuit board methodology with interconnections occurring either within a given layer or between layers, creating a 3-D architecture to the structure of embedded functionalities. Below are

described some of the initial concepts for these types of functionalities envisioned for these materials.
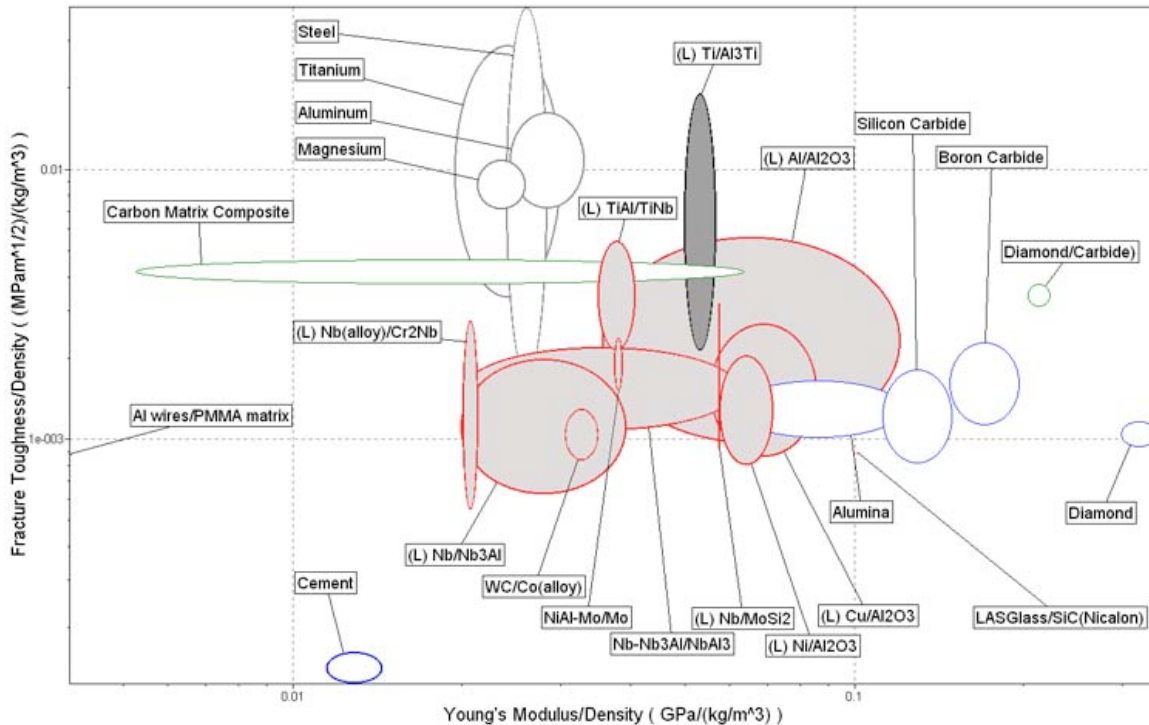
Figure 1-6.   Specific Fracture Toughness versus Specific Modulus Property map for an array of structural materials. Plot includes MIL (Ti-Al₃Ti) composites (dark gray colored) and other laminate systems (identified by (L) and colored in light gray), metals, alloys and composites.
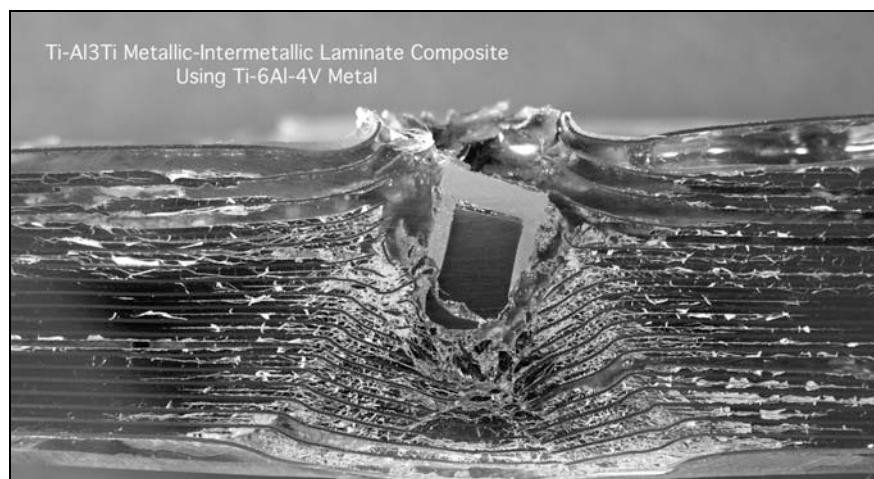
Figure 1-7.   Cross-section through the impact location from a ballistic test on a MIL composite (the plate thickness is 2 cm).
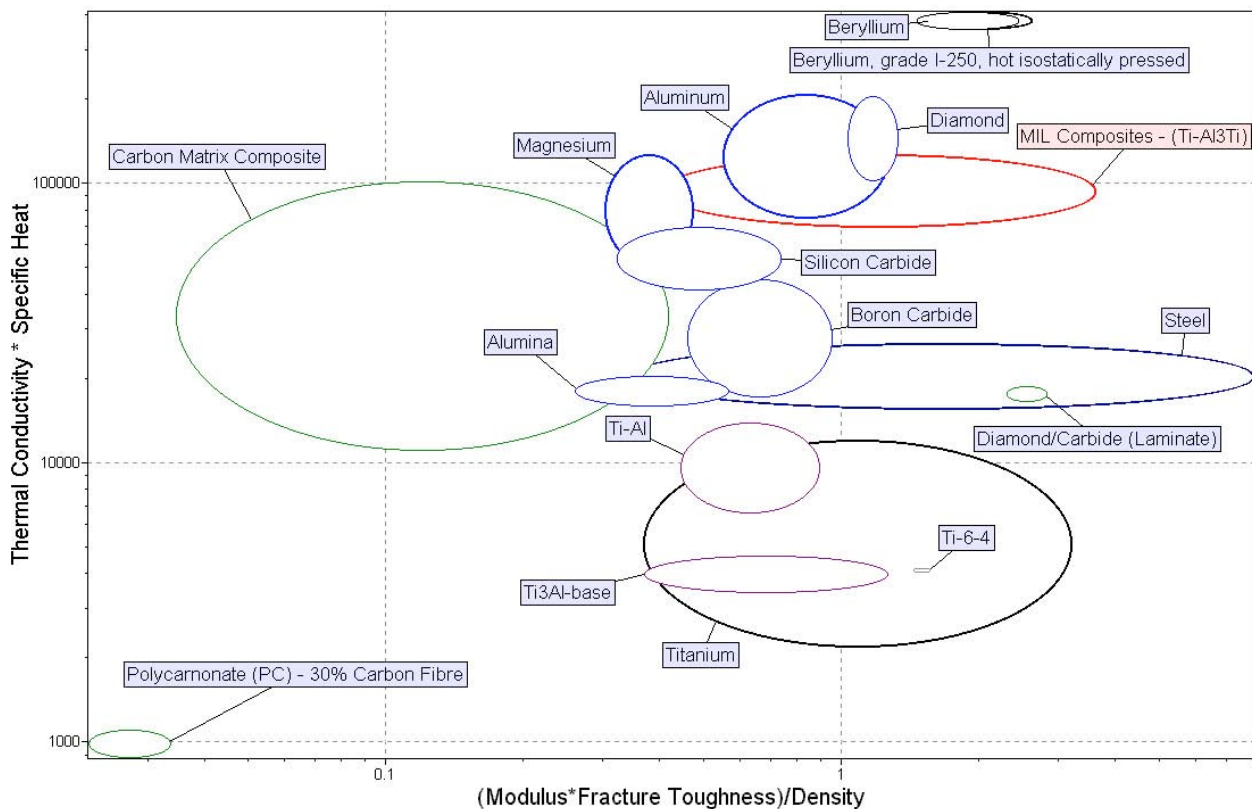
Figure 1-8. Specific Heat Capacity and Thermal Conductivity versus Specific Modulus and Fracture Toughness Property map for an array of structural materials. Plot includes MIL (Ti-Al$_3$Ti) composites (red ellipse), which overlaps diamond and aluminum at the lower end of the structural performance range for the MIL composites and lies below Be alloys in terms of the thermal properties for a similar specific stiffness/fracture toughness value.

Synthesis of MIL composites having meso-scale cavities to incorporate vibration damping

By designing cavities within the Al layers and filling these cavities with granular material, it is possible to produce MIL composites with tailored vibration damping within the intermetallic layers [11]. Figure 1-9 shows an example of the presence of these cavities within a Ti-Al$_3$Ti MIL composite. The size, distribution, and location of the cavities within the MIL composite hierarchy can be selected in the material design process by the placement of the cavities within the individual aluminum layers, and the placement of these layers within the foil stack. These cavities can be filled with granular materials to serve as particle dampers. Figure 10 shows an example of a MIL composite fabricated with a large cavity filled with steel beads to demonstrate

the concept of a particle filled cavity. Initial damping results have been presented elsewhere [11].
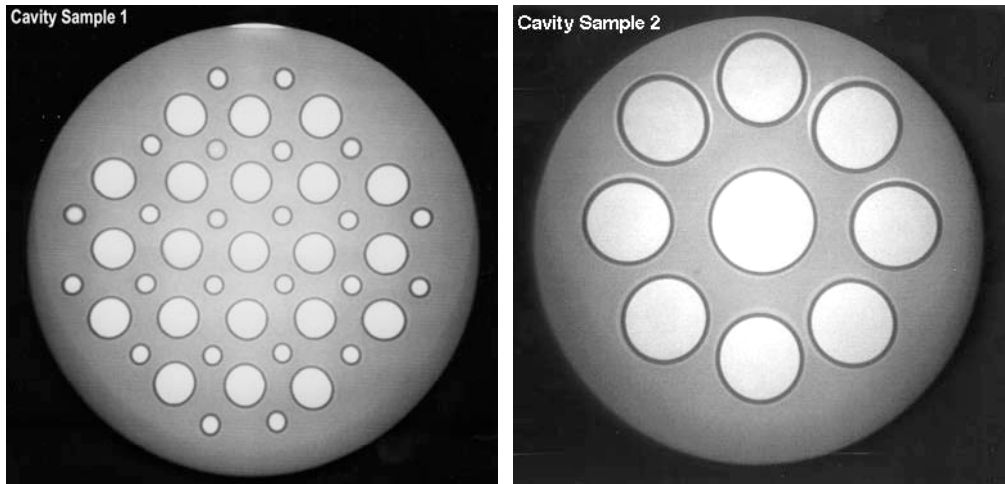
Figure 1-9. X-ray fluoroscope images through-thickness of cavities created within the intermetallic layer of a Ti-Al$_3$Ti MIL composite. The grey circular regions are approx. 13 cm in diameter.
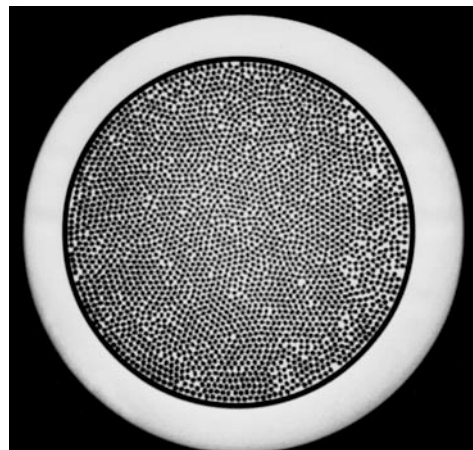
Figure 1-10. X-ray fluoroscope image through-thickness of a large (10 cm diameter) cavity filled with steel beads created within the intermetallic layer of a Ti-Al$_3$Ti MIL composite.

Enhanced Energy Absorbing or Fluid Conduit Modified MIL Composites

By embedding tubes between various layers of MIL composites it is possible to incorporate energy absorbing capacity into these materials, specifically for blast mitigation. These tubes would deform during impact and absorb the incident shock energy. Figure 1-11 illustrates the concept for this energy absorbing MIL composite system. In addition, the embedding of tubes

within the MIL composites would facilitate the passage of fluids or gases within the structure, which might be used for heat exchange, fluid transport, or embedded reactions.
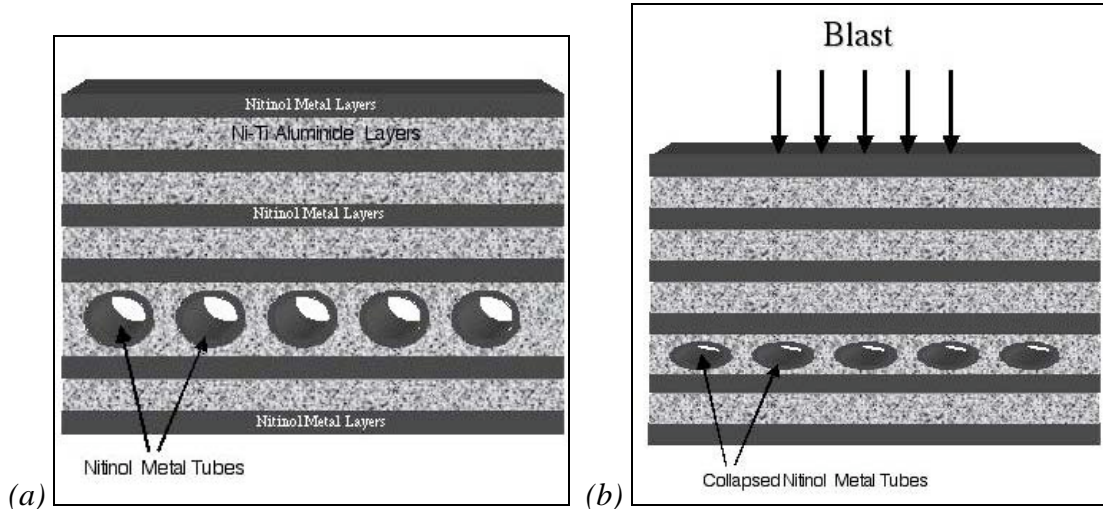
Figure 1-11.   Schematic diagrams of MIL composites containing embedded tubes within the intermetallic layers, (a) initial microstructure, and (b) microstructure with collapsed tubes following blast.

MIL Composites with Embedded Sensing Capability

Synthesis of in-plane embedded wires and tubes as electrical and/or optical pathways for damage detection and life monitoring can make these MIL composites truly multi-functional.   By creating slots in the aluminum foils prior to MIL synthesis, it is possible to introduce metal wires, metal or ceramic tubes, ceramic tubes containing metal wires, optical fibers, etc.   By suitable monitoring of the wires or fibers, it is possible to monitor and detect damage within the intermetallic layers.   In the case of the embedded wires, these wires also serve as 'micro-rebars' within the intermetallic layers to further toughen these layers.   Figure 1-12 shows an example of embedded ceramic tubes in the intermetallic layers.   The embedded ceramic tube has 2 wires within it that are electrically isolated from the sample itself.

Synthesis of MIL composites having through-thickness wires or tubes

Since metal foils are used as the starting material, it is possible to machine the foils individually or in-group to facilitate fabrication steps.   By drilling a hole through the entire foil stack and placing in the hole either a wire or tube, it is possible to create a through-thickness-strengthening

feature. Figure 1-13 shows an example of a through-thickness Ti wire embedded in a Ti-Al MIL composite plate. The location and distribution of these wires can be designed to regulate the balance between through-thickness and transverse strength. These wires can also serve as embedded electrical resistors for strain sensors or damage detection. Replacing the wires with tubes provides a method to introduce rivet-type attachment holes, and through-thickness fiber optics for imaging or environmental sensing.
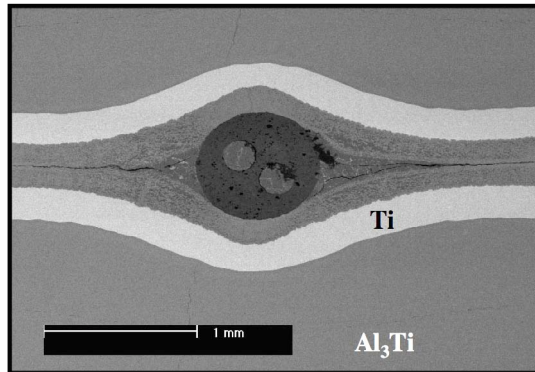
Figure 1-12. Micrograph of a Ti-Al$_3$Ti MIL composite containing a ceramic tube filled with 2 metal wires.
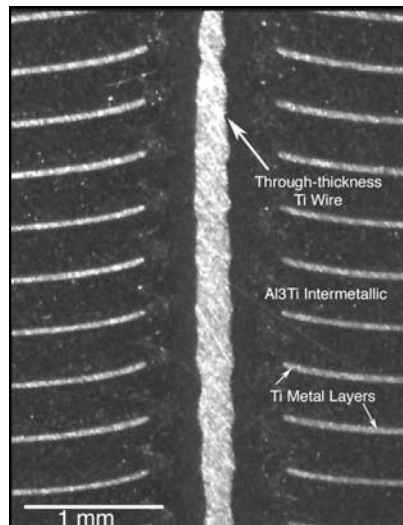
Figure 1-13. Micrograph showing an example of a through-thickness Ti wire embedded in a Ti-Al MIL composite plate.

Fully-Functional MIL Composites

The next step to 'Multi-functional' MIL composites having meso-scale cavities and electrical conduits to incorporate sensing devices, such as piezoelectric devices, accelerometers,

gyroscopes, and MEMS devices is to combine the technology of embedded cavities with the concept of embedded electrical pathways. Figure 1-14 shows an x-ray fluoroscope image of a MIL composite containing a series of cavities with interconnected electrical insulators and a pair of wires running through the cavities. These cavities can also be filled with suitable high temperature capable devices such as lithium niobate piezoelectric crystals that can be used for detection of mechanical impulses, or conversely excited electrically to produce mechanical vibration of the material. Figure 1-15 shows an illustration of a MIL composite having an embedded piezoelectric sensor within its structure and a photo of an actual embedded sensor prior to reaction of the MIL Composite. Figure 1-16 shows the voltage output from four piezoelectric sensors embedded within a MIL composite following reacting of the plate. The responses of the sensors are identical to their responses before embedding in the plate. The signals from this array of sensors have been used to perform impact location determination and through modal analysis of the signals determine the magnitude of the impact force.
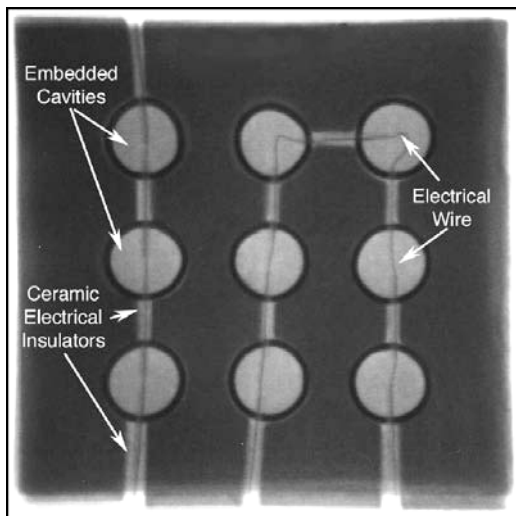
Figure 1-14.   X-ray fluoroscope image through-thickness of cavities, interconnected by ceramic insulators containing wires created within the intermetallic layer of a Ti-Al$_3$Ti MIL composite.

CONCLUSIONS

Building on the field of micro- and meso-structural design to achieve a set of targeted mechanical + functional properties, a new class of structural materials has been developed to embody and exploit this concept, termed 'Metallic-Intermetallic Laminate (MIL) Composites. The development of this novel, light-weight, multi-functional, structural composites that have the

potential to perform various other functions, such as: thermal management, ballistic protection, blast mitigation, heat exchange, vibration damping, sensing of various types through embedded devices, has been presented. From the perspective of manufacturability, this new materials system is relatively low cost, environmentally benign, capable of near net-shape processing, and allows for the material properties to be designed and tailored to the specific performance requirements of the application. Many of the additional functionalities that these materials offer are inherent in the architecture and physical properties of the material's individual phases. The fabrication approach allows these properties to be tailored, both in-plane and through-thickness in the materials.

For the active sensing functions, the design approach follows the methodologies used in the electronic materials field for fabrication of circuit boards and devices. The materials are assembled layer by layer, with the functional features incorporated primarily within the intermetallic layers, and interconnections are completed within a given layer and between layers using electrically insulated wires.

Constitutive and damage evolution models are actively being developed that could be integrated into large-scale computer codes to predict the accuracy and effectiveness of the various performance indices. The current modeling efforts also focus on determining the "Rules and Tools" for designers to utilize these inherent and embedded functionalities, their distribution and density within the material, with experimental verification of the models in progress.

(a)   (b)
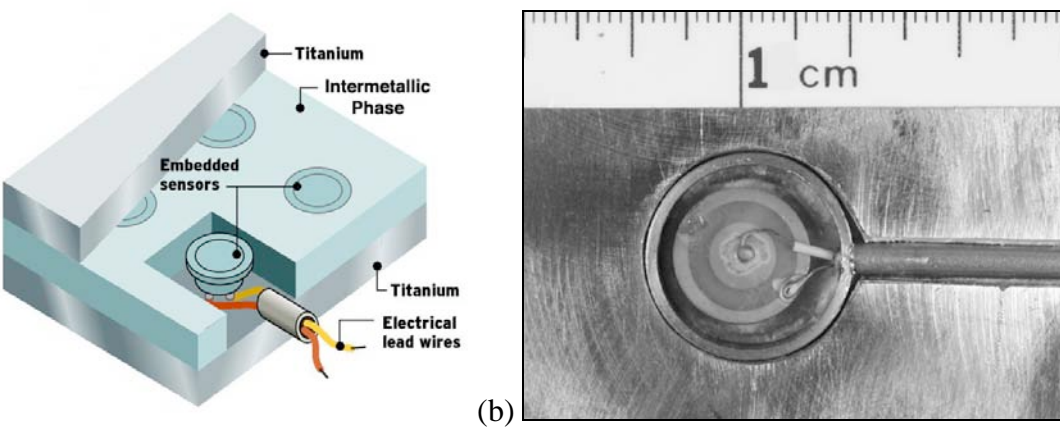
Figure 1-15.   (a) An illustration of a MIL composite having an embedded piezoelectric sensor within its structure, and (b) Photo of embedded piezoelectric sensors prior to reaction.
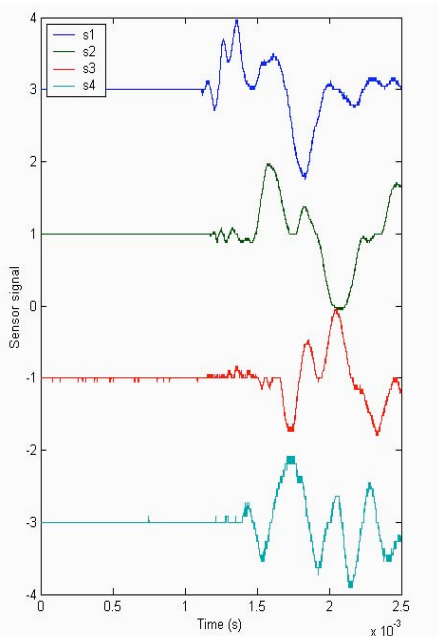
Figure 1-16.   Voltage signals recorded simultaneously from four piezoelectric sensors embedded within the MIL composites following reacting of the plate.

REFERENCES TO SECTION 1

1.   L. Christodoulou and J. D. Venables, "Multifunctional Material Systems: The First Generation, Journal of Metals, Dec. 2003, pp. 39-45.

2.   Harach, David J. and Kenneth S. Vecchio, "Microstructure Evolution in Metal-Intermetallic Laminate (MIL) Composites Synthesized by Reactive Foil Sintering in Air", Metallurgical and Materials Transactions, **32A**, 2001, pp. 1493-1505.

3.   R. Menig, M.H. Meyers, M.A. Meyers, and K.S. Vecchio, "Quasi-static and Dynamic Mechanical Response of Haliotis Rufescens (Abalone) Shells", Acta Materialia, **48** (2000) 2383-2398.

4.   R. Menig, M.H. Meyers, M.A. Meyers, and K.S. Vecchio, "Quasi-Static and dynamic mechanical response of Strombus gigas (conch) shells", Mater. Sci. & Eng., **A297** (2001) pp. 203-211.

5.   M. Sarikaya, An Introduction to Biomimetics: A Structural Viewpoint, *Microscopy Research and Technique, 1994, 27, 360 – 375.*

6.   M. Sarikaya and I. A. Aksay, in Results and Problems in Cell Differentiation in Biopolymers, *S. Case ed., Springer Verlag, Amsterdam, 1992, 1-25.*

7.   M. Sarikaya, K. E. Gunnison, M. Yasrebi, and J. A. Aksay, *Materials Research Society,*

*Pittsburgh Pa, **174** (1990) 109-116*.

8. M. Yasrebi, G. H. Kim, K. E. Gunnison, D. L. Milius, M. Sarikaya, and I. A. Aksay, Mat. Res. Soc. Symp. Proc., Vol.180, p.625.

9. M. Sarikaya, Microsc. Res. Techn. 27(1994) 369.

10. Sauthoff G., Intermetallics, Weinheim, Federal Republic of Germany: VCH Publishers, 1995. p.14.

11. Varin RA, Zbroniec L, Czujko T, Song Y-K. Materials Science and Engineering A 2001; A300:1.

12. A. Rohatgi, J.B. Kosmatka, K.S. Vecchio, K.P. Harvey, P. Nguyen, and D.J. Harach "Development of Multifunctional Metallic-Intermetallic Laminate (MIL) Composites with Particulate-based Damping" Proceedings of the 16th Annual Technical Conference of the American Society for Composites, September 9-12, 2001, Virginia Tech.

SECTION 2: EFFECTS OF DUCTILE LAMINATE THICKNESS, VOLUME FRACTION AND ORIENTATION ON FATIGUE-CRACK PROPAGATION IN Ti-Al$_3$Ti METAL-INTERMETALLIC LAMINATE (MIL) COMPOSITES

I.   INTRODUCTION

The design of structural components through micro-structural tailoring is no longer a paradigm shift; rather it has become an exciting avenue for inter-disciplinary research leading to the development of unique materials systems; metal-intermetallic laminate (MIL) composites are novel examples of such an effort [1]. The aim of the present work is to utilize the excellent complementary properties of constituent materials to create a composite endowed with optimal, application-specific properties. The concept of ductile phase toughening of brittle material, originally proposed by Kristic [2], utilizes the work of plastic stretching of a ductile component embedded in a brittle matrix to increase energy dissipation, thus leading to increased toughness. Since the original work of Kristic, there have been considerable efforts to improve the toughness of brittle materials through ductile phase reinforcements. Over the last decade, composites with different ductile reinforcement morphologies, which included particles, wires and laminates, were developed, and the effect of these ductile reinforcements on the mechanical properties has been extensively investigated for aerospace and structural applications that required optimization in weight and enhanced toughness [3-27]. A systematic study of various factors affecting the composite properties has since been accomplished. These include, the interfacial properties between phases involved that determine the extent of constraint on the ductile inclusions by the stiff brittle phase [2, 9, 28-32], the effect of reinforcement morphology (shape and size) and the volume fraction of reinforcement [3-9, 11, 12, 15-21, 33].

The concept of laminating various metals and alloys resulting in composites that exploit unique properties of the constituent materials has been known for a very long time [34]. Nevertheless, in the development of structural intermetallic composites, the idea has been embraced as a potential new engineering concept. Over the past decade, a number of diverse brittle intermetallics and ceramics have been toughened with various ductile metal laminates [15-20, 23-27, 35-62]. A number of these laminate systems were originally conceived and developed with an aim of increasing crack propagation resistance in brittle components used for high temperature aerospace applications [63-66].

In spite of such rapid progress towards understanding these novel materials, a review of the available literature indicates very few references that explored fatigue damage response of brittle/ductile laminate composites. The only metal/intermetallic systems characterized with respect to fatigue crack growth failure are $Nb/MoSi_2$ [47], Nb/Cr_2Nb [25] and Nb/Nb_3Al [19]. Fatigue crack growth rate data of $Nb/MoSi_2$ indicated a Paris exponent of ~ 9.4, compared to ~ 2-4 for typical structural metals and between 15 to 50 for ceramics. It was observed that toughening occurred by a combination of crack-tip blunting and crack bridging in the low ΔK regime, however crack bridging was absent in the high ΔK regime. It was noticed that shielding contributions from crack bridging were very limited under cyclic loading. Heathcote *et. al*. [25] measured fatigue behavior in Nb/Cr_2Nb laminates similar to that observed for monolithic Nb metal and suggested that since cracks tunnel rapidly through the brittle matrix, fatigue crack propagation is largely controlled by the metal layers. Even among other laminated metal composites, a limited number of studies have been done in elucidating the fatigue crack growth response: Al/304 stainlesss steel laminates studied by Chawla and Liaw [67] and 6090/SiC/25p-5182 studied by Huffman *et al.* [68]. More recently, Hassan *et al.* [69] investigated the effects of laminate thickness on fatigue-crack propagation in 6090/SiC/25p-6013 laminates in the arrester orientation.

Effects of cyclic loading on ductile reinforced brittle matrix composites have been studied with respect to reinforcement morphology and thickness. Despite an increase in plane-strain fracture toughness values of Nb_3Al/Nb from 2 MPa√m (pure Nb_3Al) to ~6-8 MPa√m, on cyclic testing the composites sustained stable crack growth below the toughness values, with a fatigue threshold range between 2-3 MPa√m [70]. Moreover, Nb particles in the composite that failed by ductile rupture under monotonic fracture, exhibited brittle failure mechanisms under cyclic loading [71, 72]. The absence of significant Nb-phase bridging was due to premature failure of Nb particles at stress intensities as low as 3 MPa√m, which naturally reduced any ductile-phase toughening from the deforming Nb particles. In another disc-reinforced γ-TiAl/TiNb composite system, toughening effects improved the critical stress intensity factor from 8 MPa√m to about 25-30 MPa√m, whereas fatigue-crack propagation was observed at stress intensity as low as 6 MPa√m. Moreover, crack bridging by TiNb particles was not observed to within ~150μm of the crack tip compared to bridging zones approaching ~4mm at steady state toughness conditions

under monotonic loading [4, 9]. The measured Paris exponents for the *da/dN-ΔK* curves were between 10-20 and were found to decrease with higher ductile phase content, but independent of particle thickness [7]. Under monotonic loading, stronger β-TiNb particles provided greater toughening than Nb reinforcements in brittle γ-TiAl intermetallic.

The effect of reinforcement orientation was studied in great detail for γ-TiAl/TiNb and γ-TiAl/Nb composite systems [6]. Although fatigue crack growth resistance was improved in the face (or arrester) orientation, in the edge (or divider) orientation TiNb particles actually degraded the fatigue threshold (ΔK_{TH}) relative to γ-TiAl. In contrast, Nb particles yielded better fatigue crack growth resistance over TiNb particles, which is a result of extensive debonding of Nb particles from the γ-TiAl matrix, and intrinsically higher fatigue resistance of Nb over γ-TiNb

The effect of reinforcement morphology was investigated in the $MoSi_2$/Nb system, where Nb reinforcements were either spherical particles (Nb_p) or high-aspect ratio wire mesh (Nb_m) [12, 21]. Compared to the toughness of unreinforced $MoSi_2$ at ~3 MPa√m, $MoSi_2$/Nb_p exhibited unstable fracture at ~5 MPa√m, whereas, $MoSi_2$/Nb_m exhibited rising R-curve with K_{SS} of ~13 MPa√m. The particulate reinforced composite exhibited a fatigue threshold (K_{TH}) of ~2 MPa√m, whereas the mesh-reinforced composite did not experience crack growth below a K_{TH} of 7 MPa√m.

To date, Nb/Nb_3Al is the only ductile reinforced brittle intermetallic laminate composite to be extensively studied with regards to fatigue behavior in terms of layer thickness and orientation effects [17, 19, 20]. Fatigue crack growth resistance in divider laminates, with 20% volume fraction of Nb, increased with an increase in reinforcement layer thickness and lies between the fatigue crack growth data for monolithic Nb_3Al and Nb, but closer to Nb metal. Threshold (ΔK_{TH}) values improved from ~3.5 to 7 MPa√m as Nb thickness was increased from 50 to 250µm. Although, the bridging length decreased under cyclic loading, it provided substantial toughening through bridging tractions of the ductile layers.

Designing against fatigue is crucial towards developing structural intermetallic composites, since cyclic loading is present in many of the intended applications. Failure to account for the cyclic

load history may prove detrimental to any progress towards structural uses. Since metals are susceptible to sub-critical crack growth forces, the large toughness improvements observed under static fracture may be severely reduced when the ductile metal ligaments fail under cyclic loading. Such susceptibility to sub-critical crack growth may reduce or even completely eliminate any beneficial crack tip shielding by the metallic phase and will lead to failure of structures at stress intensity levels well below toughness values. Hence, in the current work effects of ductile layer thickness, volume fraction, and orientation on the fatigue crack-growth resistance of Ti-Al$_3$Ti MIL composites are investigated.

II. EXPERIMENTAL PROCEDURES

A. Materials and laminate processing

Sheet metal of Ti-6Al-4V or Ti-3Al-2.5V and 1100 aluminum were used to fabricate Metal-Intermetallic (Ti-Al$_3$Ti) Laminate (MIL) composites by a novel one-step process that utilizes a controlled reaction at elevated temperature and pressure [1]. Alternating layers of titanium and aluminum were stacked between the platens of a screw-driven load frame in a configuration such that titanium occupied bottom and top position of the stack, see Figure 2-1. The initial thickness of starting foils was chosen in such a way that all of the aluminum was consumed in the reaction with the adjacent titanium to form the aluminide (Al$_3$Ti), while leaving some unreacted Ti. Hence, the final structure of the MIL composite consists of alternating layers of titanium and titanium aluminide with their thickness dictated by the thickness of the starting Ti and Al foils. Two batches of MIL composites were produced from various combinations of titanium and aluminum alloys starting foil thickness. From the first batch, SE(B) (Single edge-notched bend) specimen and compact tension (CT) specimens were fabricated in crack-divider orientation (see Figure 2-) and the representative MIL composite composition is listed in Table 2-. The second batch was used to fabricate SE(B) specimen in crack-arrester orientation and the layer makeup is given in

Table 2-. Henceforth, the samples will be designated by the volume fraction of Ti followed by the crack orientation (with respect to the layering geometry). For example, a 20Ti-D refers to a SE(B) specimen or CT specimen with a Ti volume fraction of 20% in a crack-divider orientation. No differences in fatigue data was observed between the SE(B) sample geometry and the compact tension (CT) geometry, for the same laminate orientation (divider). CT specimens were

only tested in the crack divider orientation. The resulting layered structure of the MIL composites are shown in Figure 2-. The average grain size of Al_3Ti (see Figure 2-4) in the MIL composites was estimated using ASTM E 112 line-intercept procedure; the optical micrographs of the corresponding ductile phase microstructure are also shown.
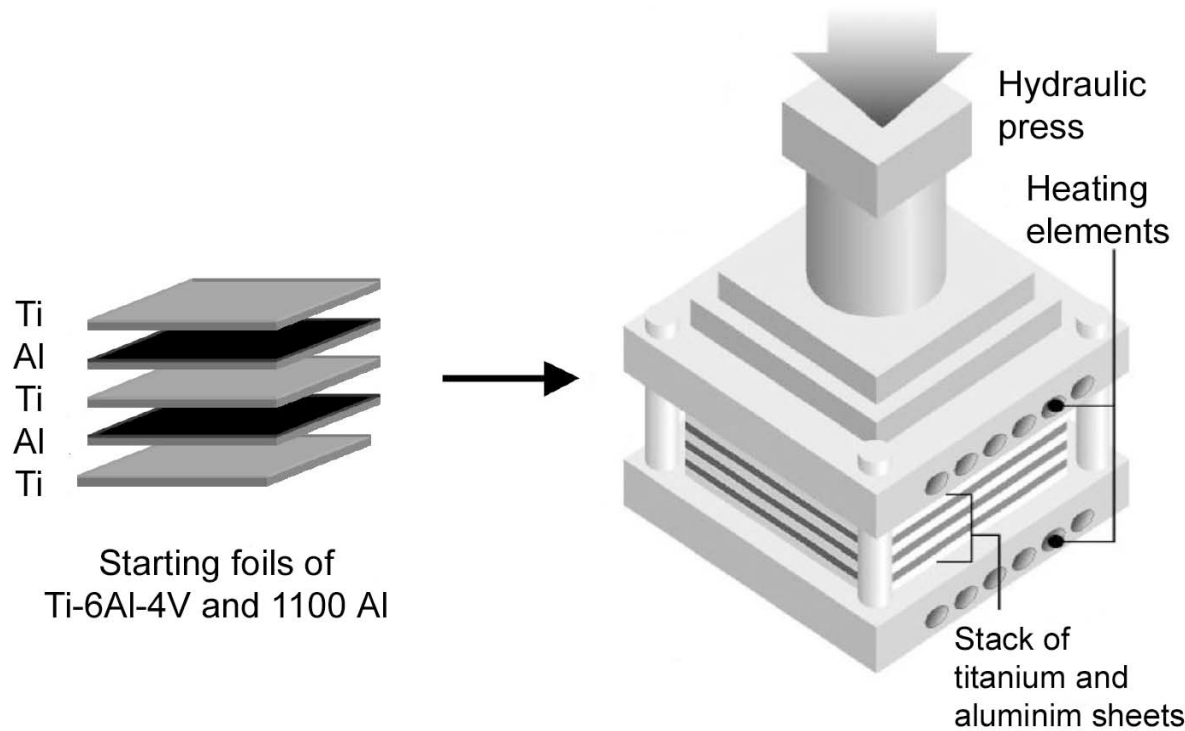
Figure 2-1.   Schematic diagram of metal-intermetallic laminate (MIL) composite fabrication apparatus.
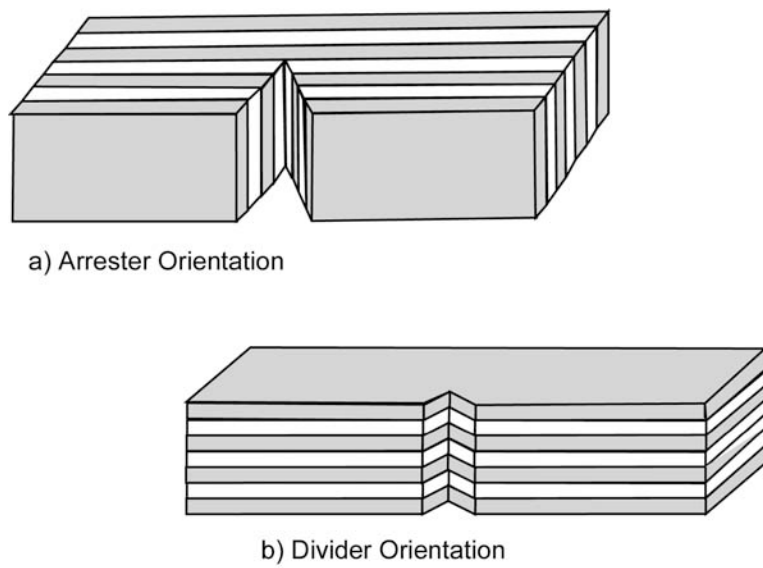
Figure 2-2. Schematic diagrams of (a) Arrester and (b) Divider Orientation in laminate composites.

Table 2-1. Measured thickness and volume fraction of constituent layers in MIL composites fabricated in divider orientation of SE(B) and CT geometry.

Sample	Starting foil thickness (µm)		Final layer thickness (µm)		Volume fraction (%)		No. of layers		Measured density
SE(B)	Ti	Al	Ti	Al$_3$Ti	Ti	Al$_3$Ti	Ti	Al$_3$Ti	g/cc
18Ti-D	508	813	206	968	17.5	82.5	10	9	3.55
21Ti-D	508	610	222	859	20.5	79.5	10	9	3.43
24Ti-D	508	508	269	833	24.4	75.6	10	9	3.60
25 Ti-D	1016	1270	579	1644	25.0	75.0	6	5	3.64
33 Ti-D	862	813	502	1030	32.8	67.2	9	8	3.70
40 Ti-D	508	381	322	477	40.3	59.7	22	21	3.83
CT									
20Ti-6-4	508	610	206	968	17.5	82.5	10	9	3.55
20Ti-3-2.5	508	813	222	859	20.5	79.5	10	9	3.43

Table 2-2. Measured thickness and volume fraction of constituent layers in MIL composites fabricated in arrester orientation of SE(B) geometry.

Sample	Starting foil thickness (µm)		Final layer thickness (µm)		Volume fraction (%)		No. of layers		Measured density
SE(B)	Ti	Al	Ti	Al$_3$Ti	Ti	Al$_3$Ti	Ti	Al$_3$Ti	g/cc
18Ti-A	508	813	238	1049	18.5	81.5	15	14	3.51
22Ti-A	508	610	253	912	21.7	78.3	17	16	3.52
33Ti-A	508	508	305	615	33.2	76.8	19	18	3.71
33Ti-A	1016	1270	671	1328	33.6	76.4	12	11	3.66
48Ti-A	508	381	415	453	47.8	52.2	22	21	3.82
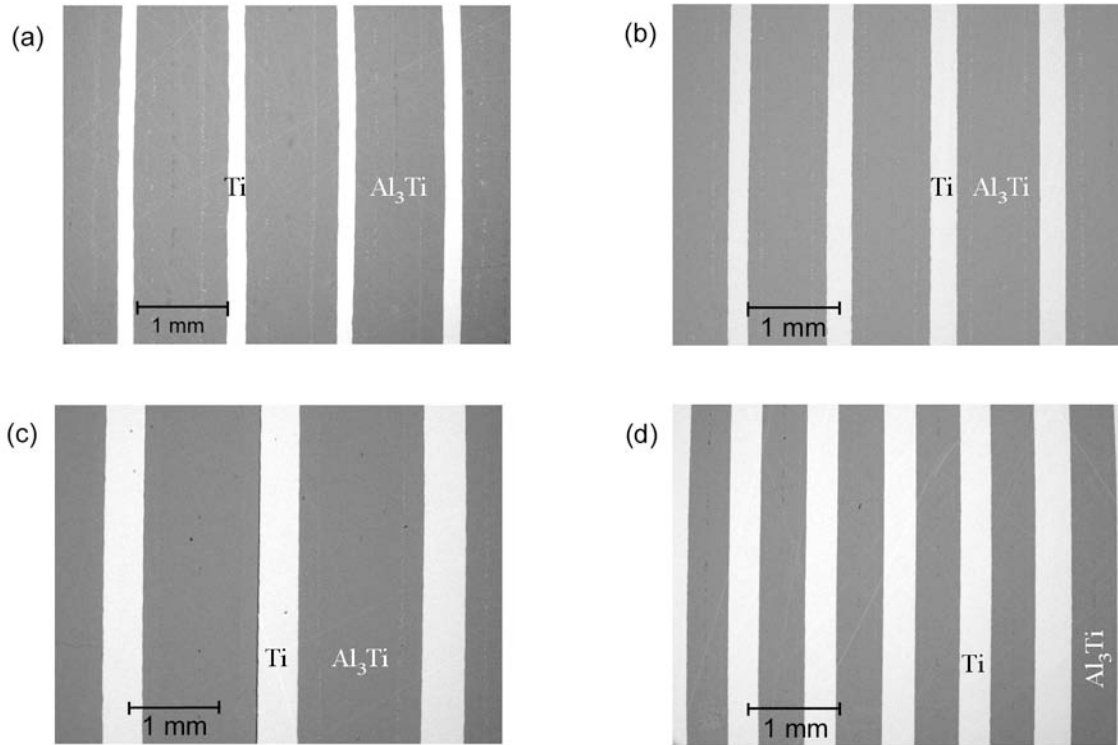
Figure 2-3.   Scanning electron micrographs of MIL composites fabricated (through-thickness section). (a) 18Ti-D (b) 24Ti-D (c) 33Ti-D (d) 40Ti-D.

B.   Specimen Preparation and Mechanical Testing

Fatigue-crack propagation tests in MIL laminates was performed on both compact tension (CT) and single-edged-notch bend {SE(B)} samples according to ASTM standard E647-98 specifications.   Compact tension (CT) samples were prepared from MIL composite plates fabricated from Ti-3Al-2.5V or Ti-6Al-4V and 1100 Al starting foils. Additionally, CT samples were machined from monolithic Ti-6Al-4V and tested under fatigue to compare the fatigue-crack growth rates with the MIL composites. The general specimen dimensions for the CT specimen, shown in Figure 2-5, were in the range of width (W) = 76 to 78mm, thickness (B) = 9 to 10 mm. The CT specimens were notched by electro discharge machining (EDM) and later tested under increasing stress intensity (ΔK), decreasing ΔK and constant K_{max} control using a closed-loop automated test system utilizing the Instron "*da/dN* program" for test control and data acquisition. Similar tests were conducted on single edge-notched bend, SE(B), specimens prepared from MIL composites, with compositions given in Table 2-1 and 2-2 and in both divider and arrester orientations.

40
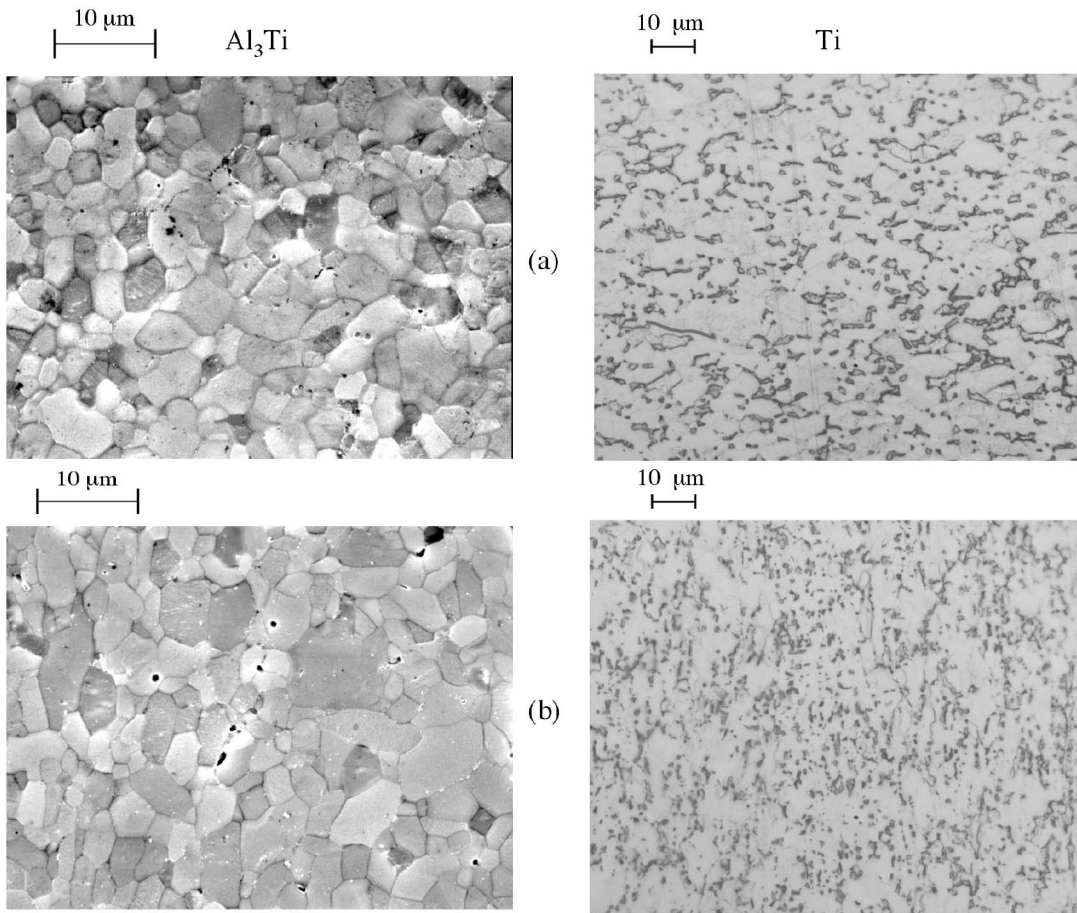
Figure 2-4.   Microstructure of Al$_3$Ti (secondary electron SEM image) and Ti (optical microscopy) in MIL composite: (a) 21Ti-D (2.6 μm Al$_3$Ti) (b) 33Ti-D (3.5 μm Al$_3$Ti)

The general specimen dimensions for SE(B) specimen were in the range of width (W) = 18 to 26mm, thickness (B) = 9 to 14 mm, and span (S) = 77 or 107.2 mm (see Figure 2-5). All samples were fatigue tested at room temperature (22°C) at a cyclic frequency of 10 Hz (sine wave). Increasing ΔK ($\Delta K \uparrow$) and decreasing ΔK ($\Delta K \downarrow$) tests were performed at a stress ratio (K_{min}/K_{max}) $R = 0.1$, in order to generate both high crack growth rate (1 x $10^{-1} > da/dN > 1$ x 10^{-5} mm/cycle) and low crack growth rate (1 x $10^{-5} > da/dN > 1$ x 10^{-7} mm/cycle) data, respectively. ΔK in all the tests was controlled according to standard load shedding techniques and is given by the equation:

$$\Delta K = \Delta K_0 \exp(-C(a_{i+1} - a_i))$$

where ΔK is the stress intensity factor range, ΔK_0 is the initial stress intensity factor range, C is the stress intensity factor gradient, and a_{i+1} , a_i are the instantaneous and initial crack lengths

respectively. For ΔK decreasing tests, C values between -0.08 mm^{-1} to -0.15 mm^{-1} were used and C values between 0.08 mm^{-1} to 0.25 mm^{-1} were used in ΔK increasing tests. Stress intensity gradients of -0.2 mm^{-1} to -0.4 mm^{-1} were used in constant K_{max} experiments. Constant K_{max} tests were conducted in such a way that the stress ratio, R, varied between 0.05 to 0.7 during the entire course of the test. The threshold stress-intensity level was defined at a crack growth rate of 10^{-7} mm/cycle. In conventional ΔK decreasing tests, both K_{max} and K_{min} are varied in such a manner that the mean stress ratio (R) remains constant. In constant K_{max} tests, only K_{min} is varied and this leads to an increasing mean stress ratio with decreasing ΔK level. There are two incentives for such a constant K_{max} tests: one is that it produces conservative low-growth-data due to higher mean stress ratio levels, and second is that the data acquisition is faster compared to ΔK decreasing tests.
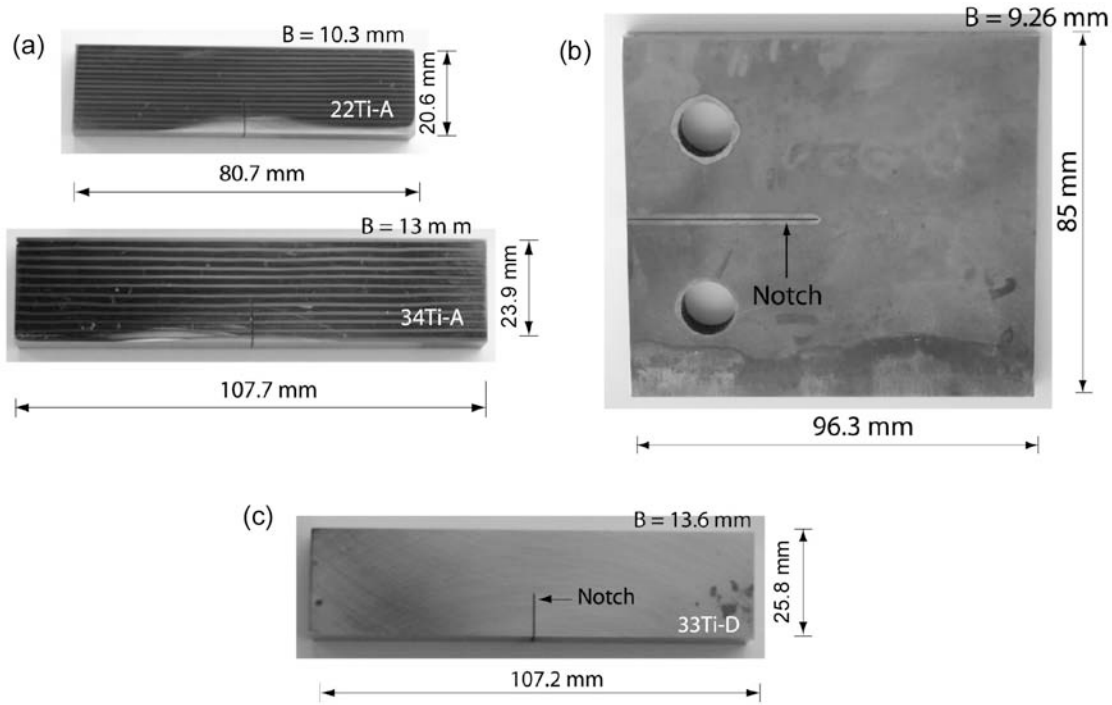
Figure 2-5.   Macrographs for MIL composites: (a) SE(B) specimens in crack-arrester orientation, (b) CT specimen in crack divider orientation (layers in plate of plate) and (c) SE(B) specimen in crack-divider orientation.

In both orientations, crack length was monitored by a crack opening displacement (COD) gage that calculates crack length using unloading compliance measurements. The COD readings were verified by direct optical measurements using a Navitar Zoom 6000 zoom lens system. Crack

length data that differed by more than 10% between the compliance and optical measurements were discarded. The reason behind such a difference will be discussed in the subsequent section.

III.   RESULTS AND DISCUSSION

A.   Monolithic Ti-6Al-4V and Al$_3$Ti materials

The fatigue-crack growth rates from both increasing and decreasing stress intensity tests for Ti-6Al-4V are shown in Figure 2-6. Threshold values of ~ 4.9 MPa√m and Paris-law slope of ~ 3.7 are observed. Monolithic Al$_3$Ti is a highly brittle material and fails at a stress intensity of ~ 2 MPa√m and is represented as a point on the fatigue-crack growth curve.
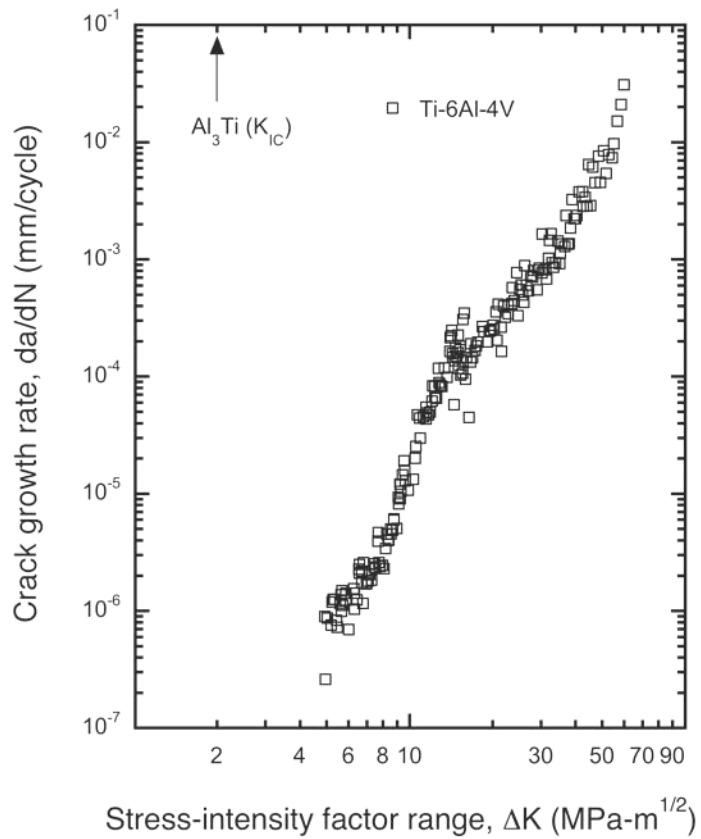
Figure 2-6.   Fatigue-crack growth behavior in monolithic Ti-6Al-4V. Fracture toughness of brittle Al$_3$Ti is also indicated.

B.   MIL COMPOSITES

Effects of ductile laminate material type: Ti-6Al-4V vs. Ti-3Al-2.5V

Figure 2-7(a) compares the fatigue crack growth data, in both the low and high crack growth regime, between laminates containing 20Ti-6-4 (20% Ti-6Al-4V) and 15Ti-3-2.5 (15% Ti-3Al-2.5V) with monolithic Ti-6Al-4V. Low crack growth behavior (10^{-7} mm/cycle $< \Delta K < 10^{-5}$ mm/cycle) in both samples was very similar, with stress-intensity factor threshold, ΔK_{TH}, equal to 4.2 MPa√m in Ti-6-4 and 4.1 MPa√m in Ti-3-2.5 reinforced composites, respectively. The threshold values for these MIL composites were very similar to that of monolithic Ti-6Al-4V (~4.9 MPa√m), whereas, at larger crack driving forces (high ΔK regime), they differed considerably, with 15Ti-3-2.5 exhibiting a fatigue failure at 31 MPa√m and 20Ti-6-4 at 44 MPa√m compared to 60 MPa√m for monolithic Ti-6A-4V. Since failure depends on the amount of material capable of plastically deforming, at large ΔK values (where K_{max} values approach K_{IC} or K_{SS}), 15Ti-3-2.5 exhibited faster crack growth rates than 20Ti-6-4 due to a combination of the lower ductile reinforcement volume fraction and inherent differences in the fracture toughness of Ti-6-4 *vs.* Ti-3-2.5.

Although fatigue crack growth was observed at stress intensities much lower compared to monotonic fracture values, an important result is that the laminates exhibited more than an order of magnitude increase in fatigue resistance over monolithic Al_3Ti that exhibits a brittle fracture at ~2 MPa√m. Such an impressive gain in fatigue resistance over Al_3Ti with a mere 20% ductile layer phase addition is worth noting. Moreover, fatigue experiments conducted at constant K_{max} control in the lower crack growth rate regime resulted in accelerated crack growth below threshold values indicated by constant R (= 0.1) tests; the mean stress ratio varied from 0.1 - 0.75 in this test. These tests thus provide conservative estimate of crack growth rates at lower stress intensities, where the mean stress ratio is higher and may better simulate actual loading conditions on structural components. The relevant mechanisms that lead to improved fatigue resistance of laminates over the brittle monolithic intermetallic will be discussed in detail in subsequent sections.

EFFECT OF ORIENTATION
Crack-divider orientation
Fatigue crack growth rate curves for the MIL composites in divider orientation, shown in Figure 2-8, exhibit a characteristic sigmoid shape, similar to monolithic structural metal alloys, with a

linear Paris crack growth regime and a clear threshold behavior under constant R ratio testing. The threshold values varied between 3.7 – 4.7 MPa√m with changes in Ti volume fraction from 18-40%. The failure of the ductile layers under cyclic loading leads to a degradation in the extent of crack tip shielding, and hence, reduces bridging lengths. Thus, the failure stress intensities, *i.e.* K_{max}, at the point of final fracture under fatigue crack growth conditions may more accurately reflect the true fracture toughness in these laminates compared to the steady-state toughness values (K_{SS}) obtained from monotonic fracture tests [14]. Under fatigue loading conditions, the bridging tractions, which contribute to the unusually high toughness displayed by these MIL composites under monotonic loading, are reduced somewhat by the fatigue process.

(a)   (b)
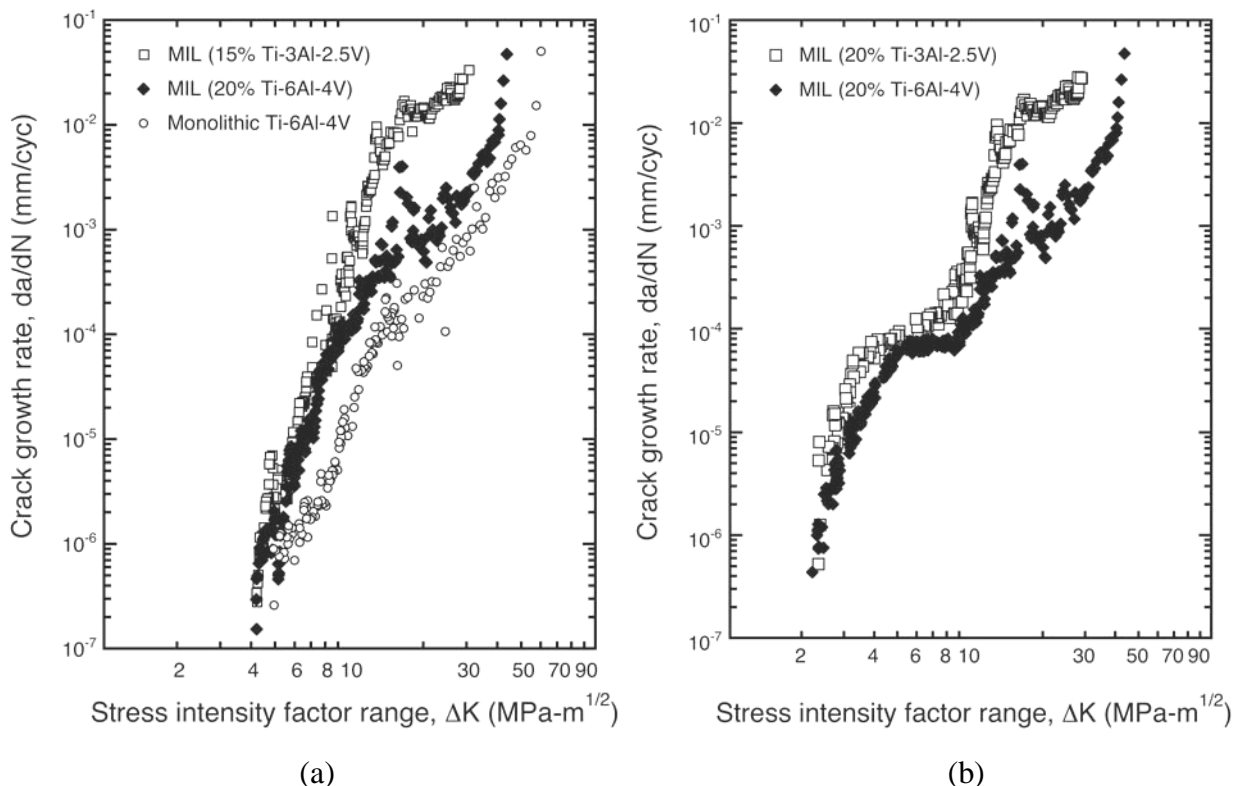
Figure 2-7. Fatigue-crack growth rates in crack-divider (CT specimen) Ti-Al₃Ti laminates as a function of (a) ΔK, stress-intensity factor range at $R = 0.1$ and (b) ΔK, at constant $K_{max} = 9$ MPa√m and $R = 0.1$ - 0.7.

This result suggests that for materials that exhibit bridging behaviors, more conservative values of fracture toughness may be obtained from a ΔK increasing fatigue crack growth test at failure. In spite of the reduced crack tip shielding, the fatigue data in Figure 2-8 indicates a dramatic improvement in fatigue crack growth resistance over the monolithic intermetallics. Furthermore,

the degradation in crack bridging in laminates under cyclic loading compared to monotonic loading is not as severe as that observed in particulate- or wire-reinforced composites [4, 12]. Similar observations were made by Bloyer *et. al.*, [19, 20] during fatigue testing of Nb/Nb$_3$Al reinforced composites.   Moreover, the volume fraction of the ductile phase in particulate composites was nearly twice compared to these MIL composites. Hence, a laminate architecture should be preferred over other geometries for enhancing fatigue resistance of brittle materials through ductile phase addition.
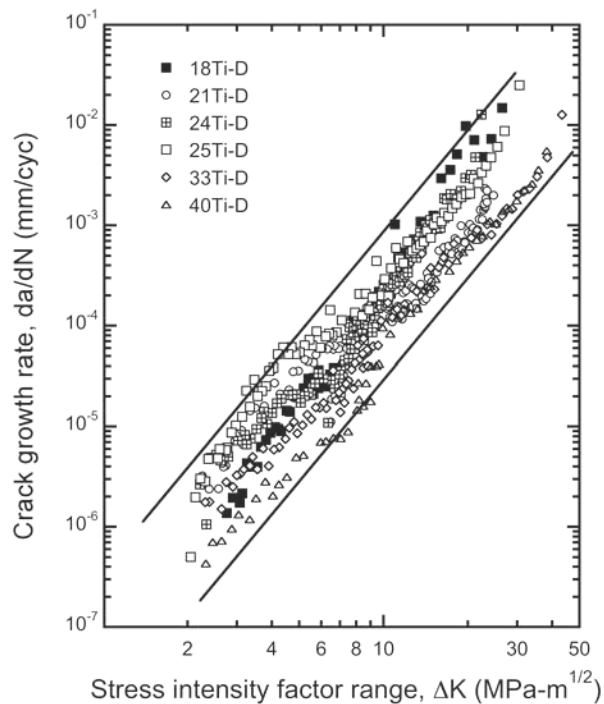
Figure 2-8. Fatigue crack growth rate curves for MIL composites in divider orientation. The crack growth rates lie between the two curves for MIL composites whose composition varies between ~18 – 40% Ti by volume.

EFFECT OF DUCTILE LAYER VOLUME FRACTION

With an increase in Ti volume fraction from 17.5 - 40.3%, the threshold varied minimally between 4.1 – 4.7 MPa√m (discussed in detail below). The thickness of the ductile layer also varied between 206μm – 502μm. Once again, in the higher crack growth regime, K_{max} values at failure increased with increase in volume fraction and stress intensities as high as 45 MPa√m were recorded, indicating fracture toughness values likely in excess of 50 MPa√m (see Figure 2-9). Since, conventional structural alloys usually have fracture toughness values between 25-125

MPa√m, the fatigue tests results indicate that MIL composites may be suitable for structural applications.

EFFECT OF LAYER THICKNESS

Dependence of fatigue crack growth rates on Ti layer thickness at a constant nominal volume fraction of ductile phase is shown in Figure 2-10. A slight improvement in fatigue resistance at higher stress intensities was observed with K_{max} increasing from 26 to 31 MPa√m as thickness increased. The threshold stress intensity however, showed very little variation with increasing Ti layer thickness. ΔK_{TH} values were 3.8 and 3.9 MPa√m for 579 μm and 267 μm Ti laminates, respectively. Bloyer *et*. *al*., [19, 20], however, observed that fatigue thresholds increased with an increase in layer thickness at a constant load ratio, *R*, of 0.1. Additionally, the same effect was retained on cyclic cracking at higher mean stress ratio, *R*, of 0.5, although, the threshold stress intensities were reduced by 30%.
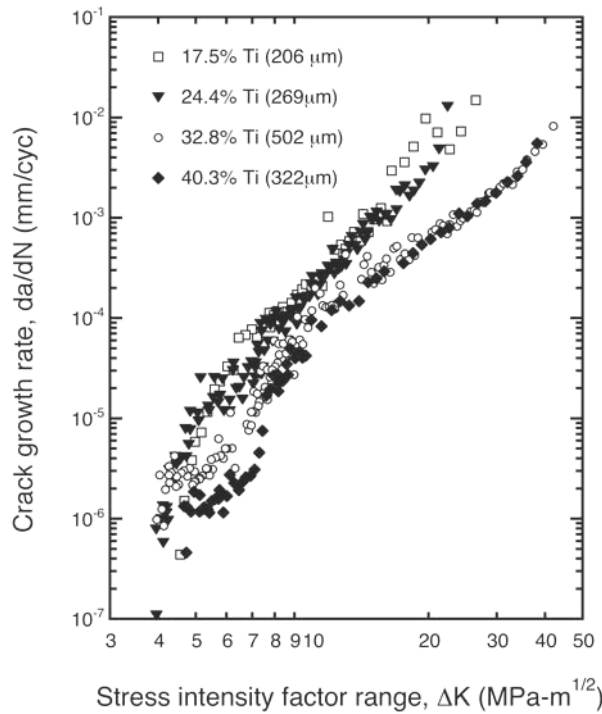
Figure 2-9. Effect of ductile layer volume fraction on fatigue crack growth rate of MIL composites.

This apparent contrast in fatigue threshold behavior may be explained as follows. All the fatigue tests conducted in the present work utilized a crack opening displacement (COD) gage to

estimate the crack length in bulk samples through unloading compliance measurements. Since the intermetallic fractures at a relatively low stress intensity of 2 MPa$\sqrt{}$m, and since the test conditions always maintain a higher ΔK, most of the intermetallic present, in or out of the plane of maximum stress, cracks readily if the stress intensity on that plane (at the crack tip) is greater than the K_{IC} of Al$_3$Ti. This is, of course, provided the ductile layer does not contribute to any crack tip shielding from far field loading.
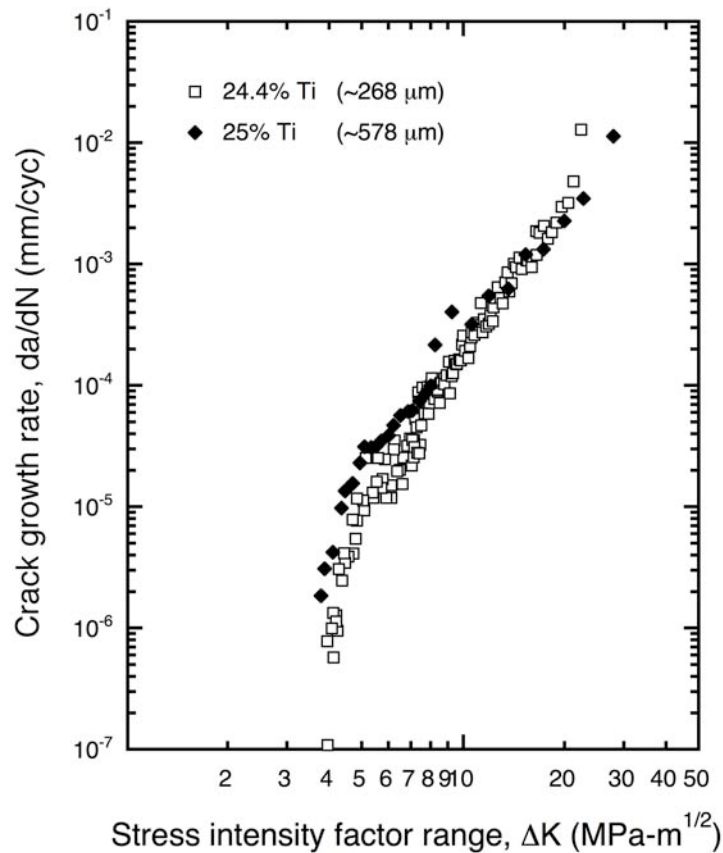
Figure 2-10. Effect of layer thickness (at constant ductile volume fraction) on fatigue crack growth rate of MIL composites.

Such early intermetallic failure leads to lower stiffness and hence the COD gage calculates an 'apparent' crack that is longer than the dominant macroscopic crack. It has to be emphasized that a true crack front, or a macroscopic crack cannot be clearly defined. Consequently, even at low stress intensities, the intermetallic fails relatively easily, and this leads to a threshold intensity value that is governed by the volume of intermetallic that fractures and the extent of ductile ligament bridging length. Since the crack does not grow below the threshold intensity,

and if one assumes that the mechanism of failure is not influenced greatly by the layer thickness, it can be argued that a constant bridging length forms near the threshold stress intensity range, irrespective of layer thickness, and thus one measures nearly the same threshold intensity ΔK_{TH}. Since the volume of intermetallic undergoing fracture varies with sample dimensions, the threshold values obtained show some scatter and may not be indicative of a true 'long crack' threshold value.

Indeed, when constant K_{max} control tests are conducted to obtain lower crack growth rate data, the composites show accelerated crack growth behavior with no apparent threshold, see Figure 2-11. This occurs because, even below 2 MPa√m (ΔK), owing to the high mean stress, R, of 0.7, K_{max} values are still higher than the Al_3Ti fracture toughness and COD measures a growing 'apparent' macro-crack. Such measurement leads to faster crack growth rates, and hence, represent conservative fatigue resistance properties. Indeed, if crack length on one of the outer faces of Ti layers is measured to calculate a 'macroscopic' long crack, the threshold may show an increased sensitivity to layer thickness, as demonstrated in K_R curve measurements. Nevertheless, the results obtained by Bloyer *et. al.*, were from tests conducted on small, micro-laminates, *i.e.*, not bulk samples. Moreover, they used DC(T) (Disc shaped compact tension) specimens for fatigue testing. It would be reasonable to argue that the fatigue behavior may have been influenced by specimen geometry, specifically, size and shape, as these affect small-scale bridging or large-scale bridging conditions.

Fatigue parameters (C, m), in the Paris equation,

$$\frac{da}{dN} = C\,(\Delta K)^m \tag{1}$$

are calculated by fitting a straight line to the linear Paris region of the fatigue curve. Table 2-3 indicates that the fatigue parameters in the Paris equation for fatigue crack growth rates are very similar to other monolithic metals or alloys. The power exponent, m, usually varies between 2-4 for many metals, and is usually very high for ceramics/intermetallics, ~20-40. The values of m for the MIL composites lie between 3 and 4.5. An additional effect due to such 'apparent' crack growth is the greater scatter in the fatigue data along the entire da/dN-ΔK curve, where, due to intermetallic cracking and subsequent fracture, the COD gage registers a sudden increase in

crack length and hence a sudden changes in the fatigue crack growth rate. After a few hundred cycles, however, the crack growth rate returns to previous steady values and continues along the sigmoidal curve. Such variations are apparent at many places in all the fatigue data presented until now.

Table 2-4.   Paris law exponents for MIL composites in divider orientation.

Material composition	C	M
8 Ti-D	3.39e-08	3.84
21 Ti-D	3.68e-08	3.41
24 Ti-D	8.40e-09	4.32
25 Ti-D	1.04e-07	3.36
33 Ti-D	3.93e-09	4.24
40 Ti-D	1.97e-08	3.46
Monolithic Ti-6Al-4V	2.1e-08	3.11
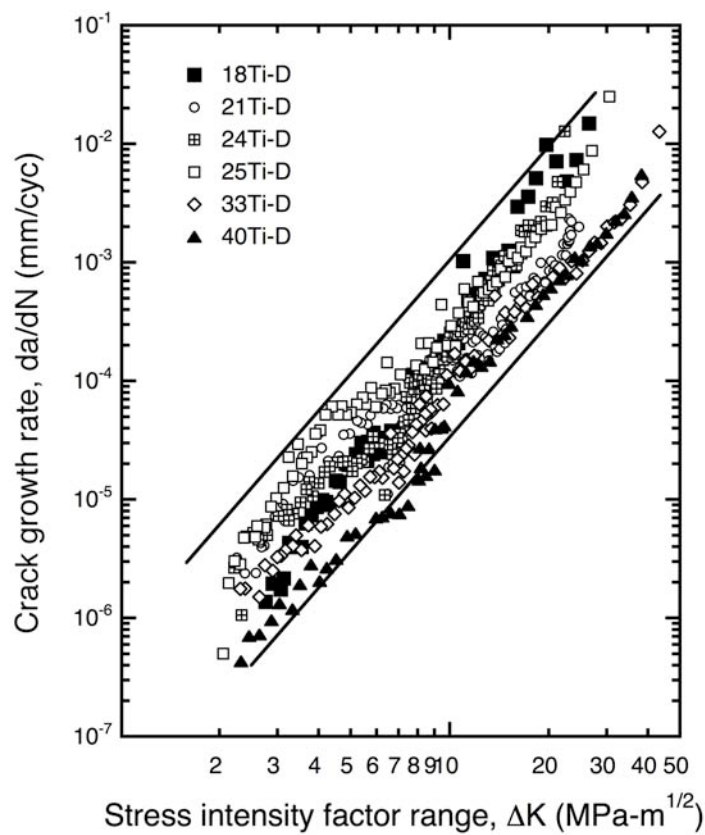
Figure 2-11. Effect of ductile reinforcement layer makeup on crack growth rate in MIL composite. Constant K_{max} test control was performed to obtain lower crack growth data.

Crack-arrester orientation

Figure 2-12 plots fatigue crack growth curves for MIL composites reinforced with varying Ti volume fraction and thickness. An interesting contrast in fatigue response at lower crack growth rates between the two orientations is apparent. The fatigue thresholds varied between 3 – 7 MPa√m, a significant change when compared to the divider orientation samples, where nearly all samples exhibited threshold values of ~3.7 – 4.7 MPa√m.

EFFECT OF DUCTILE LAYER VOLUME FRACTION

With an increase in Ti volume fraction, the arrester orientation laminates, in general, exhibited increasing resistance to fatigue crack growth. As Figure 2-13 indicates, there was an overlap of fatigue crack growth rate data between 18Ti-A, 22Ti-A and 33Ti-A, 48Ti-A laminates. This indicates that the fatigue resistance is not significantly sensitive to changes in volume fraction. The 18Ti-A and 22Ti-A laminates had fatigue threshold of 3.5 and 3.1 MPa√m respectively, slightly less than that of divider laminates with similar composition and monolithic Ti-6Al-4V. Nonetheless, the fatigue thresholds increased from 6.6 to 7 MPa√m for 33Ti-A and 48Ti-A laminates respectively, greater than ΔK_{TH} for Ti-6Al-4V. It should be noted that the Ti layer thickness also varied between 200 – 400 μm in these arrester laminates.
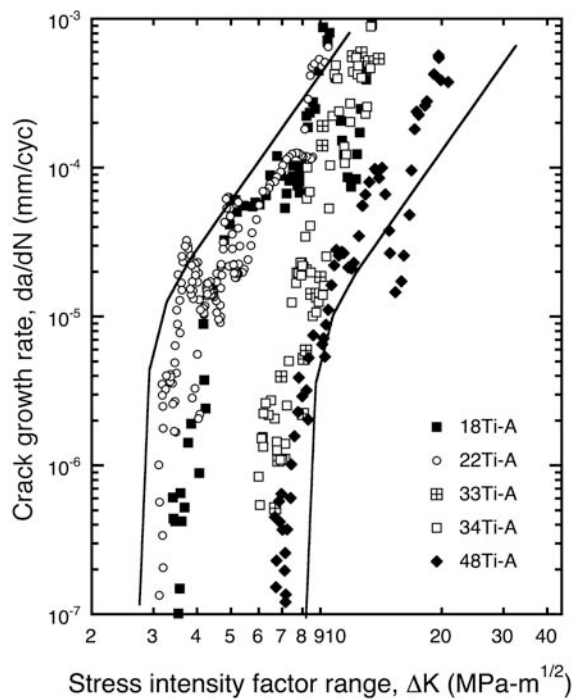
Figure 2-12. Fatigue crack growth rate curves for MIL composites in arrester orientation.

Apart from the difference in fatigue threshold values, the overlap in fatigue data in the arrester orientation laminates is similar to that observed in divider laminates at lower crack growth rates. However, scatter in fatigue data was greater in arrester laminates than in divider laminates, as evidenced from Figure 2-13. This is, once again, due to intermittent fracture of the brittle intermetallic phase during the entire loading cycles leading to a sudden increase in an 'apparent' crack length measured by the COD gage at various stress intensity levels. Such large crack growth variations yield greater crack growth rates, and hence, the fatigue data for arrester orientation laminates also represent conservative estimates. Nonetheless, the fatigue properties are significantly superior to monolithic intermetallics and ceramics.

EFFECT OF LAYER THICKNESS

Similar to divider orientation samples, the arrester orientation showed almost no sensitivity to layer thickness at the same ductile phase volume fraction, see Figure 2-14. Fatigue thresholds varied from 6 to 6.6 MPa$\sqrt{}$m for 34Ti-A and 33Ti-A laminates, respectively. Similar observations were made by Bloyer *et. al.*, [19, 20], who measured ΔK_{TH} between 6 – 7.5 MPa$\sqrt{}$m, in arrester orientation laminates of Nb/Nb$_3$Al with an increase in layer thickness at a nominal 20% ductile phase volume fraction.
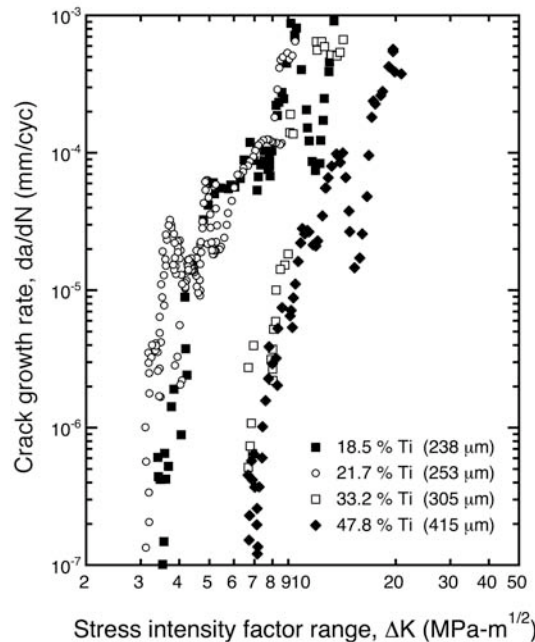
Figure 2-13.   Effect of ductile layer volume fraction on fatigue crack growth rate of MIL composites.

Figure 2-15 shows the effect of a higher mean stresses on low crack growth rate behavior during constant K_{max} tests. In contrast to divider orientation laminates that do not exhibit any well-defined threshold during constant K_{max} tests, crack growth rates in arrester orientation laminates indicate a threshold even at high mean stress levels. Although, the crack growth rate is accelerated during the early part of cyclic loading, crack growth slows down considerably at lower stress intensity ranges. This is attributed to the entire crack front being trapped in front of the ductile layer. However, the fatigue thresholds measured are lower than those obtained during constant R ratio experiments and vary between 2 to 6 MPa√m. The mechanisms leading to high threshold levels during decreasing ΔK tests are discussed below.

C.   Bridging mechanisms and fractography

The primary mechanism for toughening in MIL composites during cyclic loading was bridging zones formed by the ductile layer as the crack tunneled ahead in the intermetallic (see Figure 2-16).

DIVIDER ORIENTATION

The fatigue fracture surfaces for 20Ti-D laminate tested in a decreasing $(\downarrow)\Delta K$ condition are shown in Figure 2-17. Micrograph (a) in Figure 2- shows the failure surfaces of Ti-Al$_3$Ti layers. The crack tunnels through the Al$_3$Ti layer producing both inter- and intra-granular fracture surfaces. However, as can be seen in Figure 2-(b), a major portion of the fracture surface is intra-granular fracture. Ductile fatigue striations can be seen in Figure 2-(c), with the crack growing from bottom to top, indicating cyclic damage mechanisms that degrade crack bridging. Moreover, the ductile-brittle layers do not exhibit near interfacial cracking at low ΔK levels, see Figure 2-(d-e).
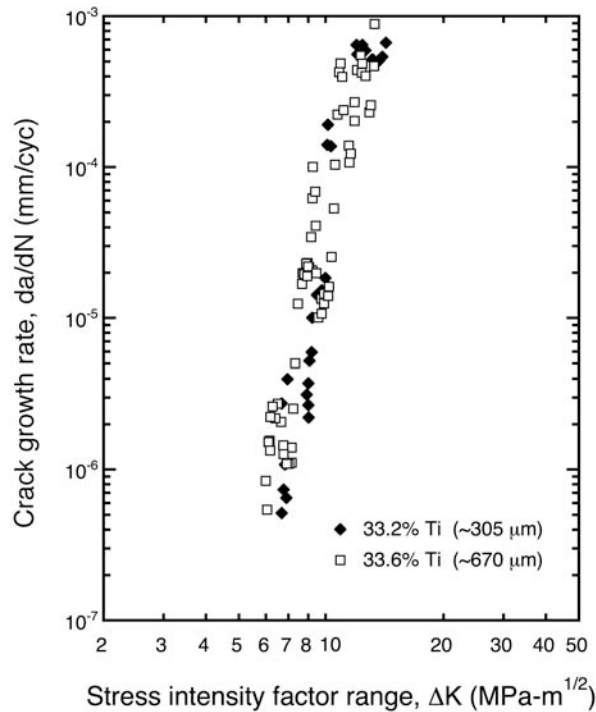
Figure 2-14.   Effect of layer thickness (at constant ductile volume fraction) on fatigue crack growth rate of MIL composites.
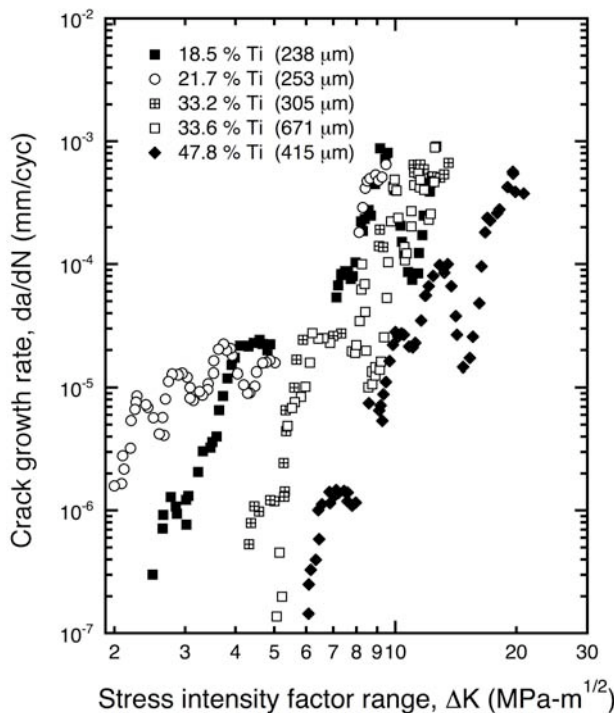
Figure 2-15.   Effect of ductile reinforcement layer makeup on crack growth rate in MIL composite.   Constant K_{max} test control was performed to obtain lower crack growth data.
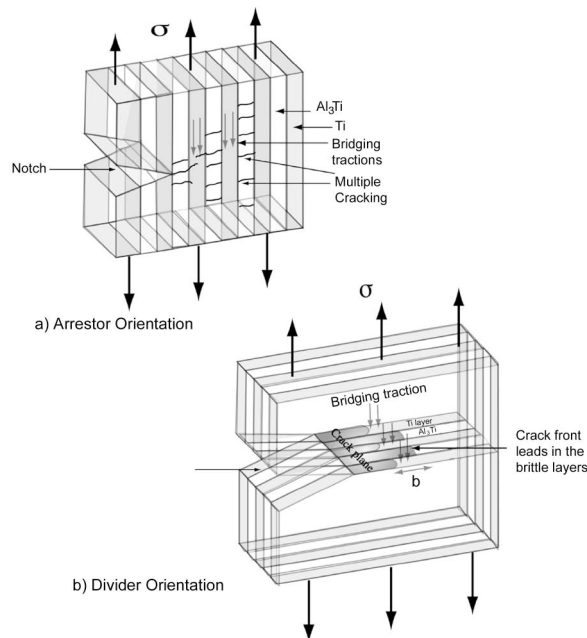
Figure 2-16.   Schematic diagram illustrating crack morphology variation due to orientation effects in laminate composites.
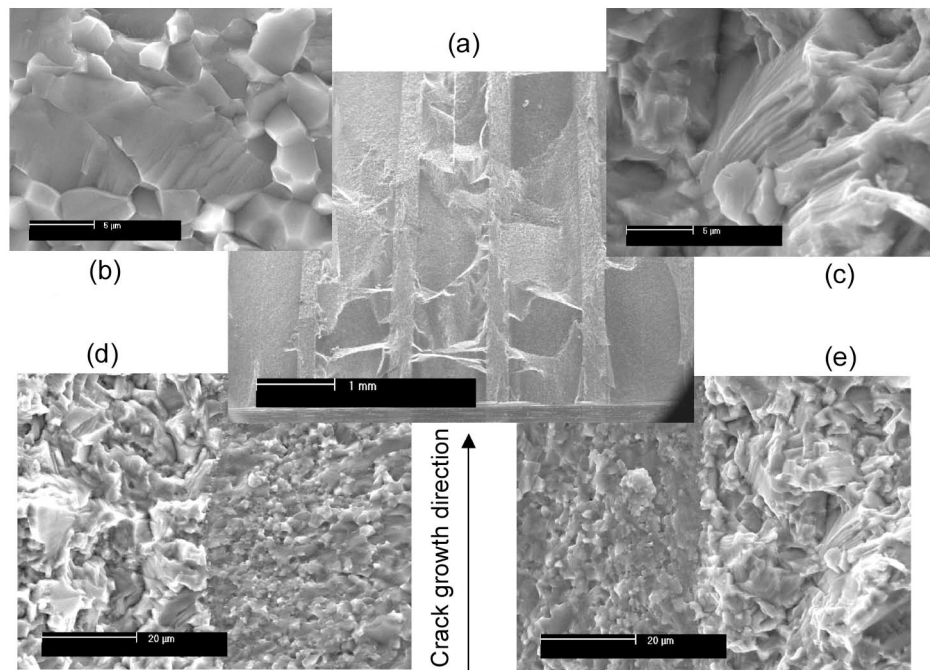
Figure 2-17.   SE images of fatigue-fracture surfaces in MIL composite 20Ti-D. (a) Micrograph showing failure of ductile/brittle layers. (b) Both inter- and intra-granular fracture of Al$_3$Ti, (c) Fatigue striations in Ti layer. (d-e) Ductile-brittle interfaces. Notice the absence of near interfacial cracking. Crack growth is from bottom to top during a ↓ΔK test ($\Delta K < 10$ MPa√m).
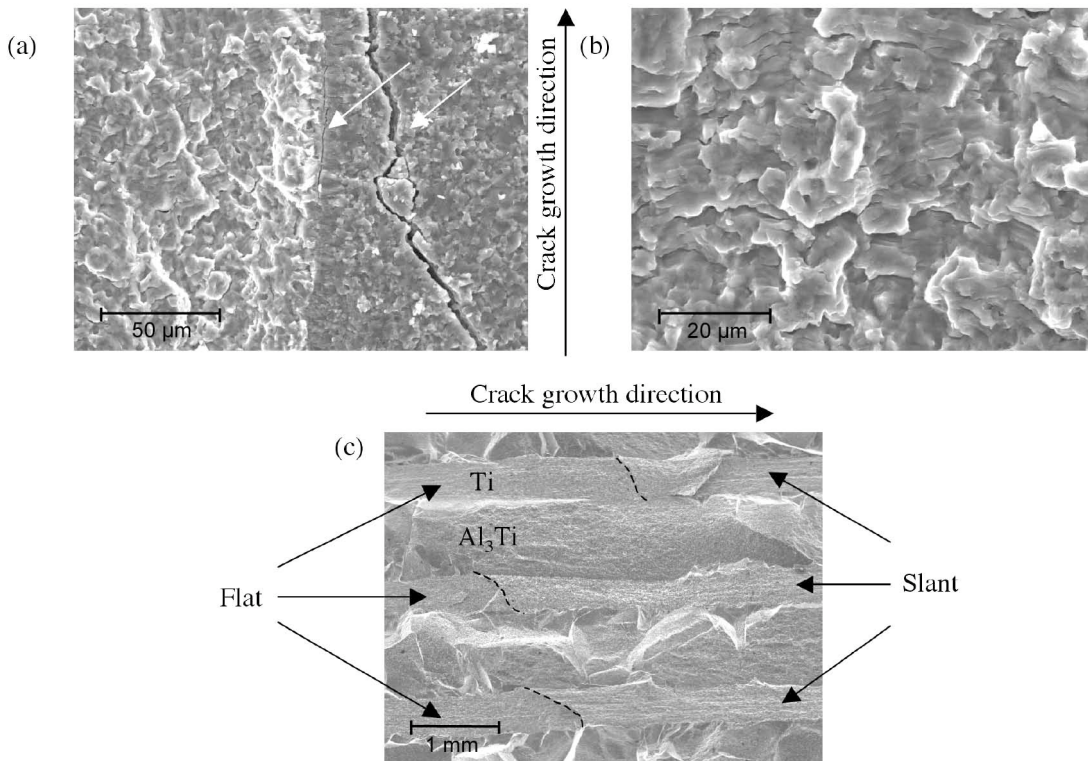
Figure 2-18. SE images of fatigue-fracture surfaces in MIL composite 33Ti-D. (a) micrograph showing evidence of interfacial crack near the ductile-brittle interface. (b) Fatigue striations in Ti layer. Notice substantial secondary cracking. Crack growth is from bottom to top in $\uparrow \Delta K$ test ($\Delta K > 20$ MPa$\sqrt{m}$). (c) Notice the change in fatigue surface from a flat fracture to a slant fracture in a constant K_{max} (= 10 MPa$\sqrt{m}$) test.

Figure 2-18 shows similar fatigue fracture surfaces in 33Ti-D laminate composite under increasing ($\uparrow$)ΔK test conditions. Interfacial cracking is now clearly observed at higher stress intensities in Figure 2-18(a). The intermetallic phase has failed largely by intra-granular fracture. Fatigue striations also formed at these high levels of stress intensities ($\Delta K > 20$ MPa$\sqrt{m}$), as shown in Figure 2-18(b), with larger striation spacing and significant secondary cracking compared to Figure 2-17(c). Even though the ductile ligaments failed under cyclic loading, they still provided enough bridging tractions to dissipate energy through plastic tearing and hence failed at stress intensity levels approaching the fracture toughness of many structural metals (> 40 MPa$\sqrt{m}$).

Bannister and Ashby [44] and Pickard and Ghosh [45] used a sandwich of metal bonded between two brittle plates to investigate the origin and degree of toughening by studying the behavior of the ductile phase near the tip of the cracks introduced in the brittle material. These sandwich tests have indicated that asymmetric or non-coplanar cracking results in higher fracture resistance under monotonic loading. Therefore, slant fracture (see Figure 2-18(c)) of the reinforcing Ti layer may have been due to non-coplanar cracking in the adjacent Al_3Ti layers and may have contributed to higher fatigue resistance.

ARRESTER ORIENTATION

While the crack path in divider orientation laminates (observed on the outer Ti surfaces of the fatigue samples) was nearly straight, the crack path in arrester orientation laminates was quite tortuous. A single definite crack front could not be defined at high stress intensities in arrester samples due to multiple non-collinear cracking, as shown in Figure 2-20. Therefore, the 'apparent' COD gage crack length measurement could not be correlated with a single macroscopic crack at high crack growth rates ($> 10^{-3}$ mm/cycle), and hence, any crack growth rate data beyond 10^{-3} mm/cycle was discarded from the fatigue plots. Figure 2-19 shows the crack profile in 18Ti-A composite, which indicates a different mechanism of ductile toughening in arrester orientation laminates. Since the intermetallic phase has low fracture strength, the crack front rapidly propagated through the intermetallic and was trapped entirely at the Ti-Al_3Ti interface. Further crack growth required renucleation of the crack near the Ti layer and hence led to an increase in threshold stress intensities with increasing layer thickness. In fact, when the notch was present exactly at the Ti/Al_3Ti interface, a crack often did not grow from the notch tip, as shown in Figure 2-20. A fatigue crack grew from the notch only when the notch tip was present in the middle of either the Ti or Al_3Ti layer. At high K_{max} values, irrespective of whether a constant $R = 0.1$ test or constant K_{max} test, cracks renucleated in the intermetallic layers ahead of the crack tip across intact ductile layers (Figure 2-20a), forming crack bridging zones that shielded the crack tip and thus increased the fatigue crack growth resistance. Furthermore, at low ΔK levels and constant $R = 0.1$ test conditions, such crack renucleation events ahead of the crack tip did not occur. During subsequent cyclic loading, the renucleated cracks in the intermetallic grew backward into the Ti layer, as shown in Figure 2-19. Due to multiple non-collinear cracking in the intermetallic, most of the renucleated cracks close to the plane of maximum stress

propagated either partially or completely through an entire Ti layer. Figure 2-19(b) shows multiple cracks indicated as 1, 2 and 3 in layer #4. Cracks far from the loading plane, such as 1, are completely arrested, whereas at 2 and 3, cracks partially grow into the Ti layer until the crack tip driving force decreased below the threshold value. Whereas, in layer #5, a renucleated crack grew parallel to the main crack, cracks growing in opposite directions in layer #2 merged after propagating through the entire Ti layer thickness. Such crack path meandering may also have contributed to higher energy dissipation and hence higher fatigue crack growth resistance.
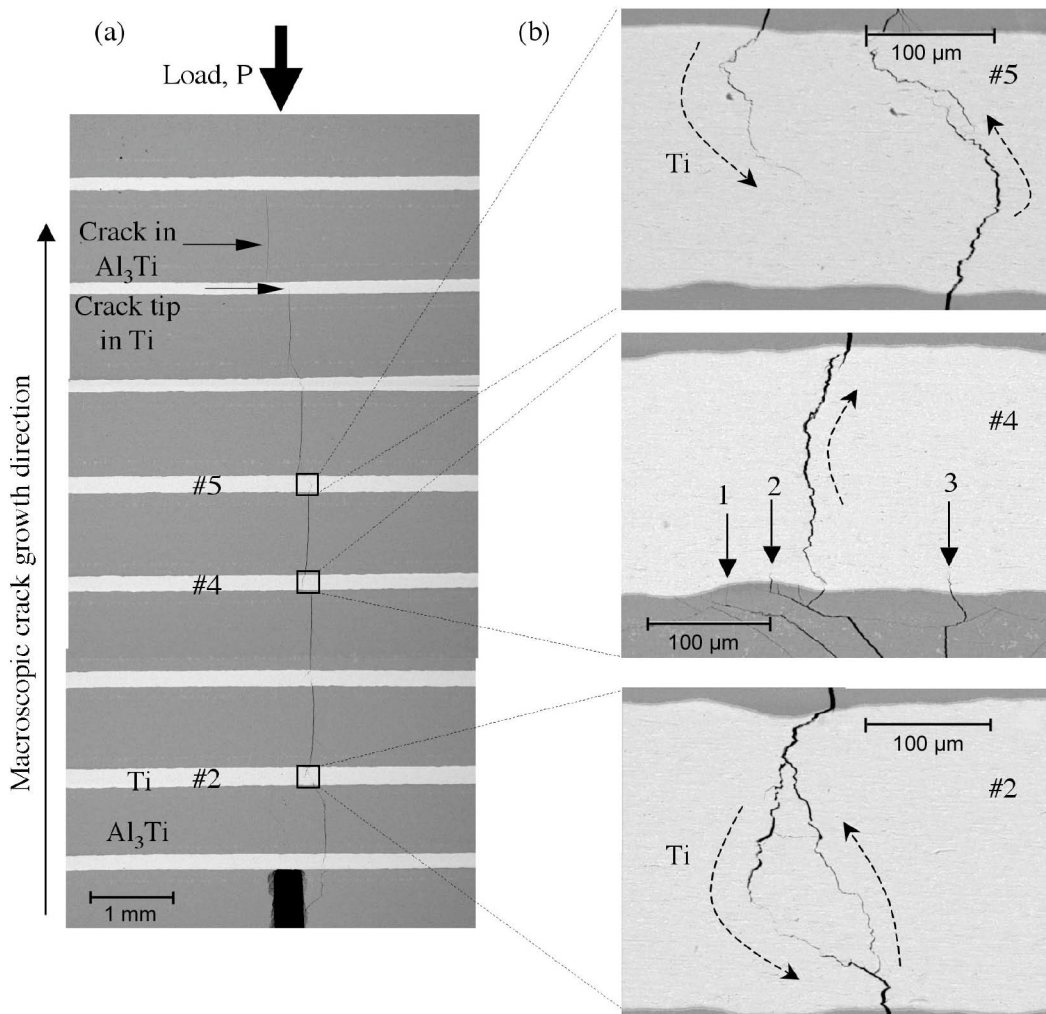
Figure 2-19.   Crack path morphology in 18Ti-A laminate in a decreasing ΔK test. (a) Crack profile in a decreasing ΔK fatigue test, (b) multiple cracking and crack path meandering. The scale bar is 100 μm for all micrographs in (b). Solid arrows in (a) indicate crack tip positions. Dotted arrows in (b) indicate the local, microscopic crack growth directions.

Figure 2-20 shows a crack profile in an increasing ΔK fatigue test on 18Ti-A composite. At low ΔK levels, a single straight crack grew uniformly through several layers. With increasing ΔK, however, a large amount of interfacial cracking and multiple non-collinear cracking occurred in the intermetallic layers ahead of the crack tip. Since a unique crack front was not identified, crack growth data at this stage was discarded. It has to be emphasized that the final ductile layer did not fail, and the crack deflected completely along the interface. With an increase in Ti volume fraction, fatigue resistance improved with increases in threshold levels and a decrease in crack growth rates at high ΔK levels.
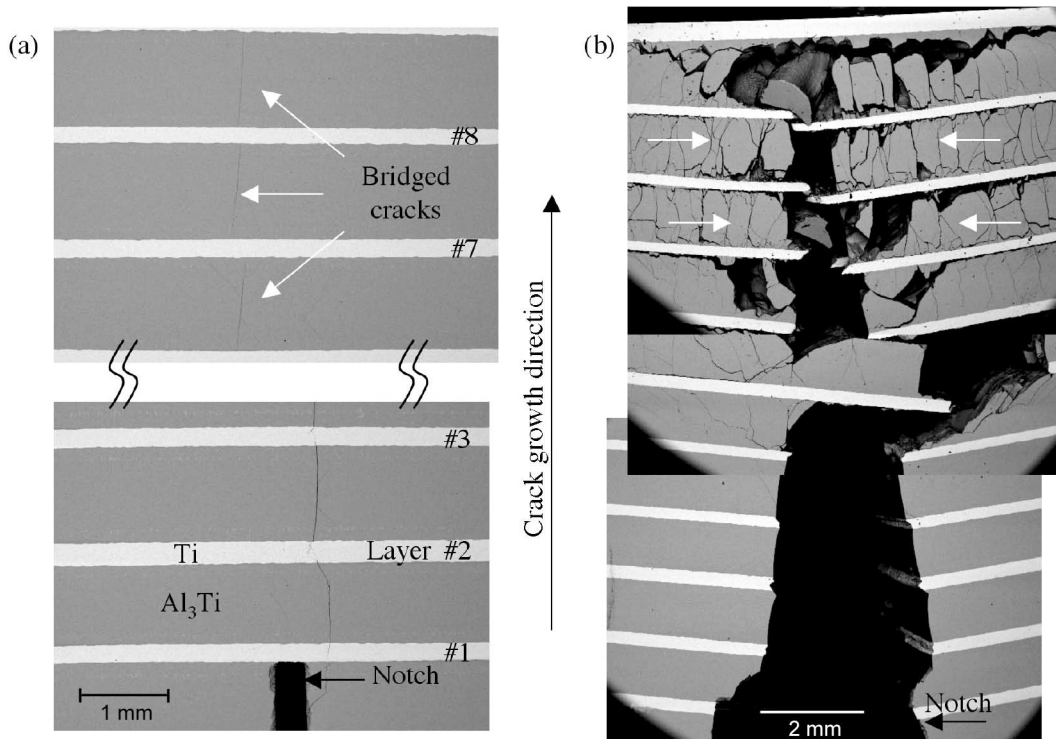
Figure 2-20.   Crack path morphology in 18Ti-A laminate in (a) Constant K_{max} test. At high K_{max} values, cracks renucleate in Al_3Ti layer ahead of intact ductile layers, thus leading to crack bridging and concomitant toughening. (b) Increasing ΔK test. Notice multiple non-collinear cracking of intermetallic layers at high ΔK levels.

Inspection of the constituent layers in Figure 2-21(a), indicates that the Ti layer failed by slant fatigue fracture. Non-coplanar cracks formed in the adjacent intermetallic layers leading to shear band deformation (see Figure 2-22) in the ductile Ti phase. The slant fatigue fracture in the Ti layers, due to being in a state of plane stress, will contribute to higher crack growth resistance. The intermetallic failed predominantly by intra-granular fracture, and interfacial cracks were

absent during cyclic loading at low ΔK levels. Therefore, while the main mechanism of toughening in divider laminates is through crack bridging by unbroken ductile ligaments, toughening in arrester laminates is provided by both crack bridging and trapping of the entire crack front in the ductile Ti layers.

Comparison between laminates and conventional metals and alloys

A comparison of fatigue crack growth rates between MIL composites and conventional metals and alloys is presented in Figure 2-23. The comparison clearly shows that MIL composites possess superior fatigue resistance over numerous monolithic ceramic and intermetallic materials and comparable crack growth rates with respect to many metal alloys. In fact, an interesting comparison emerges when stress intensities are normalized with respect to material density, as shown in Figure 2-24. The fatigue data for various high strength alloys now overlaps with that of the MIL composites indicating the suitability of these MIL composites for structural applications. The performance of a material for a particular application may depend on more than one parameter. Ti-Al MIL composites have twice the specific stiffness of steel and offer high crack growth resistance comparable to many structural metals.
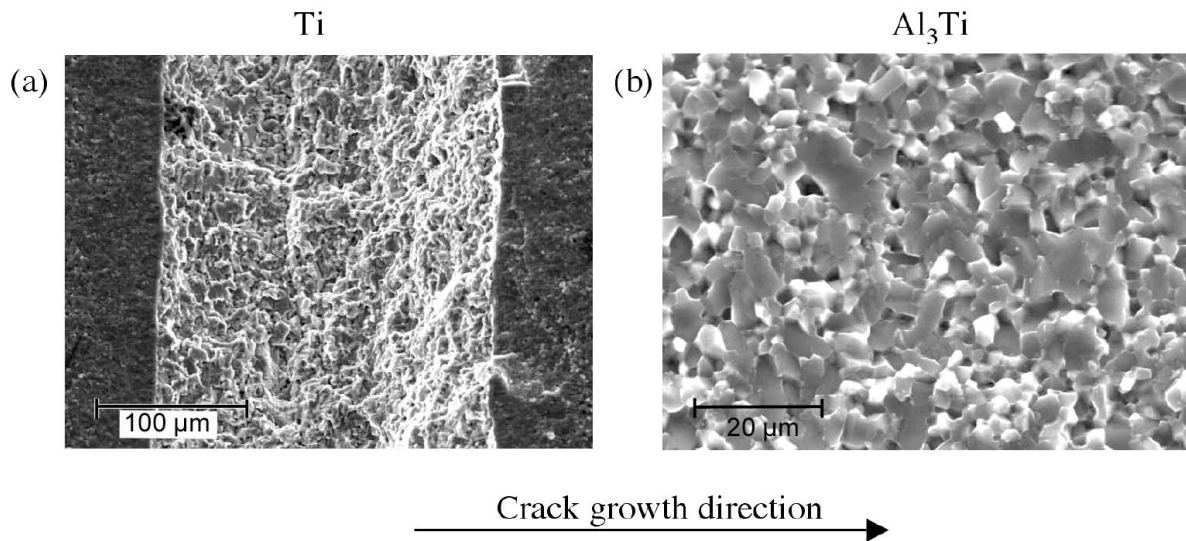
Figure 2-21.   Fatigue fracture surfaces in 22Ti-A composite. (a) Fatigue fracture surfaces at low ΔK levels. Notice slant fracture of Ti layer due to non-coplanar cracks in adjacent intermetallic layers, (b) predominantly intra-granular fracture of Al$_3$Ti.
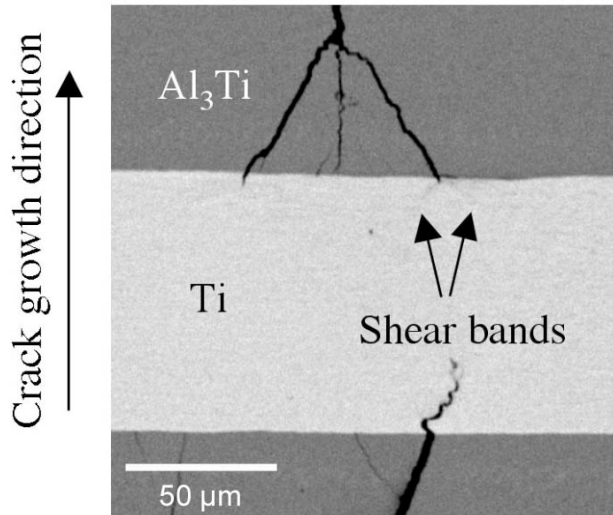
Figure 2-22.   Non-coplanar cracks formed in the adjacent intermetallic layers lead to shear band deformation and slat fracture of Ti layers.
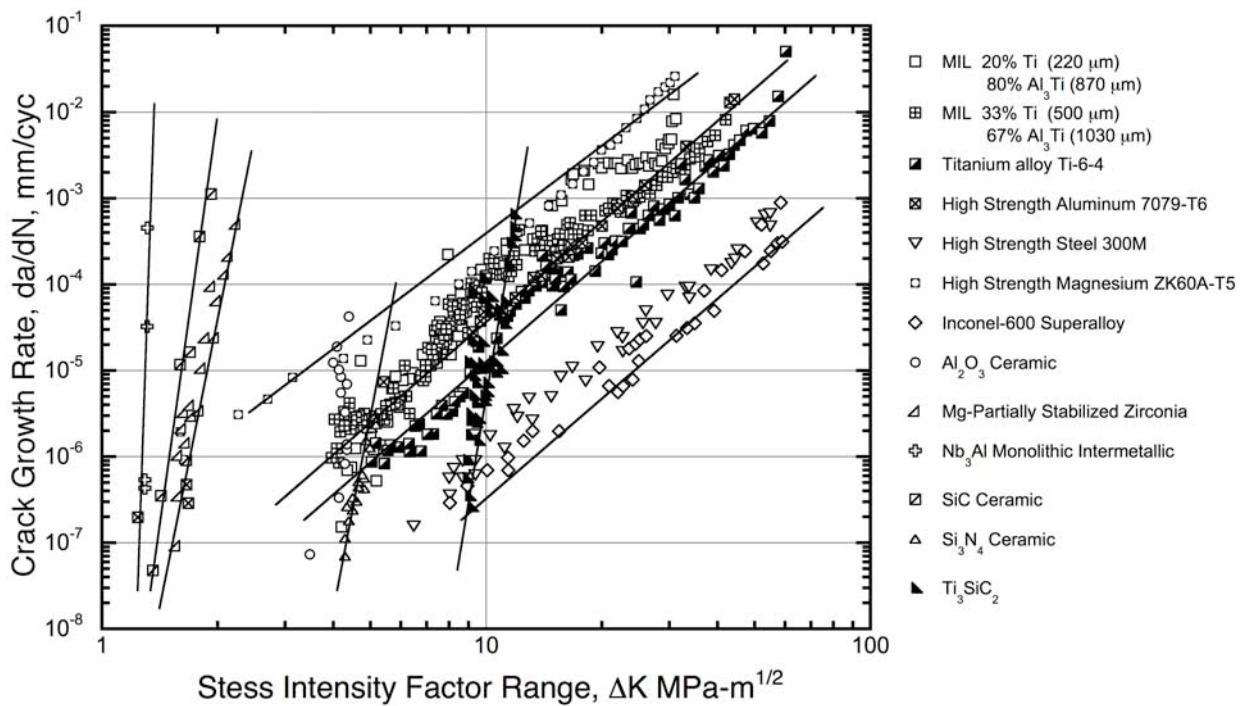
Figure 2-23.   Fatigue crack growth rates in MIL composites compared with crack growth data in various ceramics, high strength structural alloys [17, 73-75].
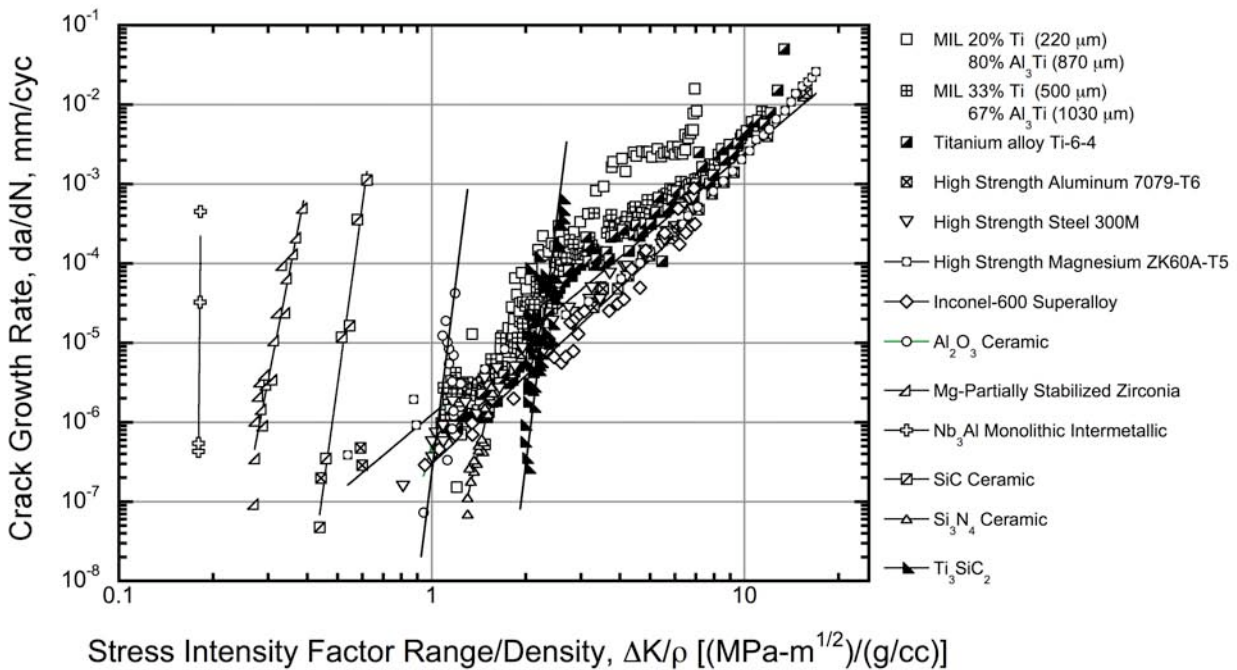
Figure 2-24.   Specific fatigue crack growth rates (da/dN - $\Delta K/\rho$) in MIL composites compared with crack growth data in various ceramics, high strength structural alloys.

CONCLUSIONS

Fatigue crack propagation in MIL composites has been studied with respect to ductile reinforcement type, volume fraction, thickness and orientation. Although both the composites exhibited similar threshold intensity values, MIL composites reinforced with Ti-6Al-4V ductile layers sustained higher stress intensities and lower growth rates at high ΔK levels compared to Ti-3Al-2.5V reinforcements. Resistance to fatigue crack propagation was seen to increase with an increase in ductile phase volume fraction. Maximum stress intensities of the order of 50 MPa√m were recorded during the high crack growth rate regime near failure. Fatigue crack growth rates showed little variation with increasing Ti layer thickness, at the same nominal volume fraction, in both arrester and divider orientations. All the laminates in divider orientation exhibited stable crack growth, with fatigue thresholds intensities between 4.1 – 4.7 MPa√m. However, in the arrester orientation, the threshold values showed significant variation. 18 vol.% Ti and 22 vol.% Ti laminates possessed fatigue thresholds of 3.5 and 3.1 MPa√m respectively, slightly less than that of the divider laminates with similar composition. The fatigue thresholds increased from 6.6 to 7 MPa√ for 33 vol.% Ti and 48 vol.% Ti composites, respectively. The

ductile Ti layers provided sufficient bridging tractions to improve fatigue resistance by almost an order of magnitude over the monolithic intermetallic, Al_3Ti. Crack tip shielding due to intact Ti layers that bridge the crack wake was seen as the mechanism for fatigue resistance in the divider orientation. In the arrester orientation however, both crack trapping at the ductile/brittle interface and subsequent crack bridging by intact Ti layers contributed to toughening. A comparison of fatigue crack growth data between MIL composites and conventional ductile metals/alloys showed the MIL composites as promising candidates for structural purposes with the added advantage of low weight and high specific stiffness.

REFERENCES TO SECTION 2

1. Harach, D.J. and K.S. Vecchio, *Microstructure evolution in metal-intermetallic laminate (MIL) composites synthesized by reactive foil sintering in air.* Metallurgical and Materials Transactions A: Physical Metallurgy and Materials Science, 2001. **32A**(6): p. 1493-1505.

2. Vladmir V. Krstic, Patrick S. Nicholson, *Toughening of glasses by metallic particles.* Journal of the American Ceramic Society, 1981. **64**(9): p. 499-504.

3. Rao, K.T.V., G.R. Odette, and R.O. Ritchie, *Fatigue and fracture resistance of ductile-phase toughened intermetallic-matrix composites: behavior in β-titanium-niobium/γ-titanium-aluminum (β-TiNb/γ-TiAl).* Fatigue Adv. Mater., Proc. Eng. Found. Int. Conf., 1991: p. 429-36.

4. Rao, K.T.V., G.R. Odette, and R.O. Ritchie, *On the contrasting role of ductile-phase reinforcements in the fracture toughness and fatigue-crack propagation behavior of titanium niobium (TiNb)/titanium aluminide (γ-TiAl).* Acta Metallurgica et Materialia, 1992. **40**(2): p. 353-61.

5. Rao, K.T.V., G.R. Odette, and R.O. Ritchie, *The role of interface and reinforcement properties on the fracture and fatigue resistance of ductile-phase toughened γ-TiAl composites.* Struct. Intermet., Proc. Int. Symp., 1st, 1993: p. 829-35.

6. Rao, K.T.V., G.R. Odette, and R.O. Ritchie, *Ductile-reinforcement toughening in γ-TiAl intermetallic-matrix composites: effects on fracture toughness and fatigue-crack propagation resistance.* Acta Metallurgica et Materialia, 1994. **42**(3): p. 893-911.

7. Rao, K.T.V. and R.O. Ritchie, *Microstructural effects on fatigue-crack growth behavior in γ-TiAl/β-TiNb intermetallic composites.* Materials Research Society Symposium Proceedings, 1992. **273**(Intermetallic Matrix Composites II): p. 127-33.

8. Rao, K.T.V. and R.O. Ritchie, *Fatigue crack propagation resistance of ductile titanium-niobium-reinforced γ-titanium-aluminum intermetallic matrix composites.* Materials Science & Engineering, A: Structural Materials: Properties, Microstructure and Processing, 1992. **A153**(1-2): p. 479-85.

9. Rao, K.T.V. and R.O. Ritchie, *Fracture and fatigue considerations in the development of ductile-phase reinforced intermetallic-matrix composites.* Fatigue Fract. Ordered Intermet. Mater. I, Proc. Symp., 1994: p. 3-12.

10. Rao, K.T.V. and R.O. Ritchie, *High-temperature fracture and fatigue resistance of a ductile β-TiNb reinforced γ-TiAl intermetallic composite.* Acta Materialia, 1998. **46**(12): p. 4167-4180.

11. Ritchie, K.T.V.R.a.R.O., *Microstructural effects on fatigue-crack growth behavior in γ-TiAl/β-TiNb Intermetallic composites.* Materials Research Society Symposium Proceedings, 1992. **273**: p. 127-133.

12. Rao, K.T.V., W.O. Soboyejo, and R.O. Ritchie, *Ductile-phase toughening and fatigue-crack growth in niobium-reinforced molybdenum disilicide intermetallic composites.* Metallurgical Transactions A: Physical Metallurgy and Materials Science, 1992. **23A**(8): p. 2249-57.

13. Soboyejo, W.O., et al., *Effects of reinforcement architecture on the fatigue and fracture behavior of MoSi$_2$/Nb composites.* Fatigue and Fracture of Ordered Intermetallic Materials II, Proceedings of a Symposium, Rosemont, Ill., Oct. 6-10, 1994, 1995: p. 359-90.

14. Soboyejo, W.O., F. Ye, and T.S. Srivatsan, *An investigation of the effect of ductile phase reinforcement on the fatigue and fracture behavior of a gamma-titanium aluminide intermetallic.* Fatigue and Fracture of Ordered Intermetallic Materials II, Proceedings of a Symposium, Rosemont, Ill., Oct. 6-10, 1994, 1995: p. 391-415.

15. Bloyer, D.R., K. T. Venkateswara Rao, Ritchie, R. O., *Resistance-curve toughening in ductile-phase reinforced intermetallic laminates.* Johannes Weertman Symposium, Proceedings of a Symposium held during the TMS Annual Meeting, Anaheim, Calif., Feb. 4-8, 1996, 1996: p. 261-266.

16. Bloyer, D.R., K.T. Venkateswara Rao, and R.O. Ritchie, *Fracture toughness and R-curve behavior of laminated brittle-matrix composites.* Metallurgical and Materials Transactions A: Physical Metallurgy and Materials Science, 1998. **29A**(10): p. 2483-2496.

17. Bloyer, D.R., K.T. Venkateswara Rao, and R.O. Ritchie, *Laminated Nb/Nb$_3$Al composites: effect of layer thickness on fatigue and fracture behavior.* Materials Science & Engineering, A: Structural Materials: Properties, Microstructure and Processing, 1997. **A239-240**: p. 393-398.

18. Bloyer, D.R., V. Rao, and R.O. Ritchie, *Resistance-curve toughening in ductile/brittle layered structures: behavior in Nb/Nb$_3$Al laminates.* Materials Science & Engineering, A: Structural Materials: Properties, Microstructure and Processing, 1996. **A216**(1-2): p. 80-90.

19. Bloyer, D.R., K.T.V. Rao, and R.O. Ritchie, *Fatigue-crack propagation behavior of ductile/brittle laminated composites.* Metallurgical and Materials Transactions A: Physical Metallurgy and Materials Science, 1999. **30A**(3): p. 633-642.

20. Bloyer, D.R., K.T.V. Rao, and R.O. Ritchie, *Toughness and subcritical crack growth in Nb/Nb$_3$Al layered materials.* Materials Research Society Symposium Proceedings, 1996. **434**(Layered Materials for Structural Applications): p. 243-248.

21. Badrinarayanan, K., A.L. McKelvey, K.T.V. Rao, and R.O. Ritchie, *Fracture and fatigue-crack growth behavior in ductile-phase toughened molybdenum disilicide: effects of niobium wire vs. particulate reinforcements.* Metallurgical and Materials Transactions A: Physical Metallurgy and Materials Science, 1996. **27A**(12): p. 3781-3792.

22. Bencher, C.D, A. Sakaida, K.T.V. Rao, R.O. Ritchie,*Toughening mechanisms in ductile niobium-reinforced niobium aluminide (Nb/Nb₃Al) in situ composites.* Metallurgical and Materials Transactions A: Physical Metallurgy and Materials Science, 1995. **26A**(8): p. 2027-33.

23. Odette, G.R, B.L. Chao, J.W. Sheckherd and G.E. Lucas, *Ductile phase toughening mechanisms in titanium aluminide (TiAl)-titanium-niobium laminate composite.* Acta Metallurgica et Materialia, 1992. **40**(9): p. 2381-9.

24. J. Heathcote, G.R.Odette, G. E. Lucas, R. G. Rowe and D. W. Skelly, *On the micromechanics oflow temperature strength and toughness of intermetalic/metallic microlaminate comosites.* Acta mater., 1996. **44**(11): p. 4289-4299.

25. Heathcote, J., .R. Odette, G.E. Lucas, R.G. Rowe, *Mechanical properties of metal-intermetallic microlaminate composites.* Materials Research Society Symposium Proceedings, 1996. **434**(Layered Materials for Structural Applications): p. 101-112.

26. Heathcote, J., G.R. Odette, and G.E. Lucas, *A finite element study on constrained deformation in an intermetallic/metallic microlaminate composite.* Materials Research Society Symposium Proceedings, 1996. **434**(Layered Materials for Structural Applications): p. 183-188.

27. Aashish Rohatgi, David J. Harach, Kenneth S. Vecchio, Kenneth P. Harvey, *Resistance-curve and fracture behavior of Ti-Al₃Ti metallic-intermetallic laminate (MIL) composites.* Acta Mat., 2003. **51**: p. 2933-2957.

28. Ashby, M.F., F.J. Blunt, and M. Bannister, *Flow characteristics of highly constrained metal wires.* Acta Metallurgica, 1989. **37**(7): p. 1847-57.

29. Cao, H.C., et al., *A test procedure for characterizing the toughening of brittle intermetallics by ductile reinforcements.* Acta Metallurgica, 1989. **37**(11): p. 2969-77.

30. Deve, H.E., A.G. Evans, G.R. Odette, R. Mehrabian, M.L. Emiliani and R.J. Hecht. *Ductile reinforcement toughening of titanium aluminide (γ-TiAl): effects of debonding and ductility.* Acta Metallurgica et Materialia, 1990. **38**(8): p. 1491-502.

31. Deve, H.E. and M.J. Maloney, *On the toughening of intermetallics with ductile fibers: role of interfaces.* Acta Metallurgica et Materialia, 1991. **39**(10): p. 2275-84.

32. J.D. Embury, F.Zok, D.J. Lahaie and W. Poole. *The properties of interfaces in composites*. in *Intrinsic and extrinsic fracture mechanisms in Inorganic composite systems*. 1995: MRS Proceedings, p. 1-5.

33. Rao, K.T.V. and R.O. Ritchie, *Fracture and fatigue-crack growth in γ-TiAl intermetallic composites at ambient and high temperatures.* Fatigue and Fracture of Ordered Intermetallic Materials II, Proceedings of a Symposium, Rosemont, Ill., Oct. 6-10, 1994, 1995: p. 327-38.

34. Lesuer, D.R., C.K Syn, O.D. Sherby, J. Wadsworth, J.J. Lewandowski, and W.H. Hunt, Jr., *Mechanical behavior of laminated metal composites.* International Materials Reviews, 1996. **41**(5): p. 169-197.

35. Rawers, J. and K. Perry, *Crack initiation in laminated metal-intermetallic composites.* Journal of Materials Science, 1996. **31**(13): p. 3501-3506.

36. Dong Seok Chung, Y.T., Manabu Enoki and Teruo Kishi, *Formation behavior of aluminide layers during the fabrication of Nb/Nb-aluminide laminate materials from Nb and Al foil.* J. Japan Inst. Metals, 1999. **63**(8): p. 1043-1052.

37. Chung, D.-S., M. Enoki, and T. Kishi, *Microstructural analysis and mechanical properties of in situ Nb/Nb-aluminide layered materials.* Science and Technology of Advanced Materials, 2002. **3**(2): p. 129-135.

38. Enoki, M., Atsuko Ohta, Dong Seok Chung, Makoto Watanabe and Teruo Kishi, *Crack propagation behavior of Ti/Ti-Al layered materials.* Nippon Kinzoku Gakkaishi, 2000. **64**(11): p. 1076-1081.

39. Rawers, J.C. and D.E. Alman, *Fracture characteristics of metal/intermetallic laminate composites produced by reaction sintering and hot pressing.* Composites Science and Technology, 1995. **54**(4): p. 379-84.

40. Manabu Enoki, K.S., Byung-Nam Kim and Teruo Kishi, *Crack Propagation of Ni/NiAl Laminate Materials.* J. Japan Inst. Metals, 1999. **63**(7): p. 838-843.

41. Rowe, R.G., D.W. Skelly, M.r. Jackson, M. Larsen and D. Lachapelle, *Advanced aircraft engine microlaminated intermetallic composite turbine technology.* Materials Research Society Symposium Proceedings, 1996. **434**(Layered Materials for Structural Applications): p. 3-13.

42. Kajuch, J., J. Short, and J.J. Lewandowski, *Deformation and fracture behavior of Nb in Nb_5Si_3/Nb laminates and its effect on laminate toughness.* Acta Metallurgica et Materialia, 1995. **43**(5): p. 1955-67.

43. Rigney, J.D., *Fracture of laminated and in situ niobium silicide-niobium composites.* Materials Research Society Symposium Proceedings, 1996. **434**(Layered Materials for Structural Applications): p. 227-241.

44. Bannister, M. and M.F. Ashby, *The deformation and fracture of constrained metal sheets.* Acta Metallurgica et Materialia, 1991. **39**(11): p. 2575-82.

45. Pickard, S.M. and A.K. Ghosh, *Bridge toughening enhancement in double-notched $MoSi_2/Nb$ model composites.* Metallurgical and Materials Transactions A: Physical Metallurgy and Materials Science, 1996. **27A**(4): p. 909-21.

46. Xiao, L. and R. Abbaschian, *On the flow behavior of constrained ductile phases.* Metallurgical Transactions A: Physical Metallurgy and Materials Science, 1993. **24A**(2): p. 403-15.

47. Soboyejo, W.O., F. Ye, L-C. Chen, N. Bahtishi, D.S. Schwartz and R.J. Lederich, *Effects of reinforcement morphology on the fatigue and fracture behavior of $MoSi_2/Nb$ composites.* Acta Materialia, 1996. **44**(5): p. 2027-41.

48. J. M. McNaney, R.M.Cannon, R.O.Ritchie, *Fracture and fatigue-crack growth along aluminum-alumina interfaces.* Acta mater., 1996. **44**(12): p. 4713-4728.

49. Huang, Y. and H.W. Zhang, *The role of metal plasticity and interfacial strength in the cracking of metal/ceramic laminates.* Acta Metallurgica et Materialia, 1995. **43**(4): p. 1523-30.

50. Dalgleish, B.J., K.P. Trumble, and A.G. Evans, *The strength and fracture of alumina bonded with aluminum alloys.* Acta Metallurgica, 1989. **37**(7): p. 1923-31.

51. M. Y. He, F.E.Heredia, D. J. Wissuchek, M. C. Shaw and A. G. Evans, *The Mechanics of crack growth in layered materials.* Acta metall. mater., 1993. **41**(4): p. 1223-1228.

52. M. C. Shaw, D.B.Marshall, M. S. Dadkhah and A. G. Evans, *Cracking and damage mechanisms in ceramic/metal multilayers.* Acta metall. mater., 1993. **41**(11): p. 3311-3322.

53. Evans, A.G., H.C. Cao, *On crack extension in ductile/brittle laminates.* Acta metall. mater., 1991. **39**(12): p. 2997-3005.

54. Hwu, K.L. and B. Derby, *Fracture of metal/ceramic laminates-II. Crack growth resistance and toughness.* Acta Materialia, 1999. **47**(2): p. 545-563.

55. Hwu, K.L. and B. Derby, *Fracture of metal/ceramic laminates-I. Transition from single to multiple cracking.* Acta Materialia, 1999. **47**(2): p. 529-543.

56. Dalgleish, B.J., M.C. Lu, and A.G. Evans, *The strength of ceramics bonded with metals.* Acta Metallurgica, 1988. **36**(8): p. 2029-35.

57. Lesuer, D.R., J. Wadsworth, R.A. Riddle, C.K. Syn, J.J. Lewandowski and W.H. Hunt Jr., *Toughening mechanisms in Al/Al-SiC laminated metal composites.* Materials Research Society Symposium Proceedings, 1996. **434**(Layered Materials for Structural Applications): p. 205-211.

58. M.R. Fox, A.K.Ghosh, *Structure, strength and fracture resistance of interfaces in NiAl/Mo model laminates.* Mater. Sci. & Eng., 1999. **A259**: p. 261-268.

59. Q. Ma, M.C.Shaw, M.Y. He, B.J. Dalgleish, D.R. Clarke and A.G. Evans, *Stress redistribution in ceramic/metal multilayers containing cracks.* Acta metall. mater., 1995. **43**(6): p. 2137-2142.

60. Alman, D.E., et al., *Processing, structure and properties of metal-intermetallic layered composites.* Materials Science & Engineering, A: Structural Materials: Properties, Microstructure and Processing, 1995. **A192/193**: p. 624-32.

61. Alman, D.E., J.C. Rawers, and J.A. Hawk, *Microstructural and failure characteristics of metal-intermetallic layered sheet composites.* Metallurgical and Materials Transactions A: Physical Metallurgy and Materials Science, 1995. **26A**(3): p. 589-99.

62. Xia, Z., et al., *Fabrication of laminated metal-intermetallic composites by interlayer in-situ reaction.* Journal of Materials Science, 1999. **34**(15): p. 3731-3735.

63. Westbrook, J.H. *Structural intermetallics: their origins, status and future.* in *Struct. Intermet., Proc. Int. Symp., 1st.* 1993: TMS.

64. Anton, D.L. and D.M. Shah, *High temperature ordered compounds for advanced aero-propulsion applications.* Materials Research Society Symposium Proceedings, 1989. **133**(High-Temp. Ordered Intermet. Alloys 3): p. 361-71.

65. Anton, D.L. and D.M. Shah, *Ductile phase toughening of brittle intermetallics.* Materials Research Society Symposium Proceedings, 1990. **194**(Intermet. Matrix Compos.): p. 45-58.

66. Larsen, J.M., W.C. Revelos, and M.L. Gambone, *An overview of potential titanium aluminide composites in aerospace applications.* Materials Research Society Symposium Proceedings, 1992. **273**(Intermetallic Matrix Composites II): p. 3-16.

67. K.K. Chawla and P.K. Liaw, J. Mater. Sci., 1979. **14**: p. 2143-2150.

68. P.B. Huffman, R.D. Carpenter, J.C. Gibeling. in *Materials Research Society Symposia Proceedings*, J.J. Lewandowski, C.H. Ward, M.R. Jackson, and W.H. Hunt Jr., eds., Material Research Society, Pittsburgh, PA, 1996, vol. 434, pp.281-86.

69. Hala A. Hassan, J.J.Lewandowski, and M.H. Abd El-Latif, *Effects of lamination and changes in layer thickness on fatigue-crack propagation of lightweight laminated metal composites.* Metallurgical and Materials Transactions A, 2004. **35A**: p. 45-52.

70. Murugesh, L., et al., *Fracture and fatigue behavior in niobium aluminide (Nb3Al) + niobium intermetallic composites.* Materials Research Society Symposium Proceedings, 1992. **273**(Intermetallic Matrix Composites II): p. 433-8.

71. Murugesh, L., K.T.V. Rao, and R.O. Ritchie, *Crack growth in a ductile-phase-toughened niobium/niobium aluminide(Nb$_3$Al) in situ intermetallic composite under monotonic and cyclic loading.* Scripta Metallurgica et Materialia, 1993. **29**(8): p. 1107-12.

72. Soboyejo, W.O., F. Ye and T.S. Srivatsan, *An investigation of the effect of ductile phase reinforcement on the fatigue and fracture behavior of a gamma-titanium aluminide intermetallic.* Fatigue and Fracture of Ordered Intermetallic Materials II, Proceedings of a Symposium, Rosemont, Ill., Oct. 6-10, 1994, 1995: p. 391-415.

73. Hertzberg, R.W., *Deformation and fracture mechanics of engineering materials.* 1996: John Wiley & Sons, Inc.

74. Speidel, M.O. *Fatigue crack growth at high temperature.* in *High temperature materials in gas turbines.* 1974. Baden, Switzerland: Elsevier Scientific Publishing Company.

75. Barsoum, M.W., *Fundamentals of Ceramics.* 1997: Institute of Physics Publishing, IOP.

SECTION 3: FRACTURE OF Ti-Al₃Ti METAL-INTERMETALLIC LAMINATE (MIL) COMPOSITES: EFFECTS OF LAMINATION ON R-CURVE BEHAVIOR

I.   INTRODUCTION

Intermetallics are known to possess high compressive strength and stiffness, high oxidation resistance and melting temperatures, some with low density, and generally good creep resistance [1].   However, owing to their ordered structure, intermetallics exhibit limited dislocation mobility leading to brittle fracture at low temperatures ($\sim 2\text{MPa}\sqrt{m}$ for Al₃Ti), thus limiting their use as structural components. Considerable research has gone into the development of structural intermetallics [2], and one of the strategies for increasing the utility of intermetallics involves the toughening of the intermetallic with ductile reinforcements. Over the last two decades, composites with different ductile reinforcement morphologies, which included particles, wires and laminates, were developed, and the effect of these ductile reinforcements on the mechanical properties has been extensively investigated [3-9]. In spite of the classical tradeoff between higher stiffness/strength or higher toughness, an optimal application-specific microstructural design can be achieved by incorporating the excellent properties exhibited by the individual components in the right microstructure architecture. The development of MIL composites is a step towards that direction.

Previous studies on mollusk shells [27, 28] have shown that hierarchical structures over various length scales, based on weak constituents (CaCO₃ and organic binders), endow the final structure with highly optimized mechanical properties.   Such bio-mimetic motivation has led to the development of MIL composites with damage critical properties, such as specific fracture and fatigue properties (*i.e.*, properties normalized with density), equal or superior to the component materials. MIL composites do not possess a strict hierarchical structure exhibited by the mollusk shells, instead, they are layered materials with discrete interfaces over the micro-scale. Nevertheless, such bio-mimetic architecture at a single length scale has been shown to dramatically improve many properties such as fracture and impact behavior [26].

In order to use the beneficial properties of the intermetallic Al₃Ti, such as high compressive strength and stiffness, low density and good creep resistance, while mitigating its detrimental

brittle nature, it is necessary to reinforce the brittle phase with tougher ductile metals [29]. Various methods that have been developed to produce laminate composite structures include diffusion bonding, deposition, and spray forming, [30-40]. Lesuer *et al.* [41] reviewed the history of laminated metal composites (LMC's) along with various processing techniques in detail. The particular process used to fabricate MIL composites, the focus of this work, is "reactive foil sintering" or "reaction bonding". The details of the processing technique are discussed elsewhere [30]. The objective of the present work is, therefore, to quantify the fracture properties of such novel MIL composites with respect to ductile thickness and volume fraction. Such a study will enable us to delineate the toughening mechanisms in MIL composites, and to extend our understanding of the fracture and failure mechanisms eventually paving the way towards development of structural intermetallic composites optimized for user/application-specific properties.

Concepts of toughening

An important property that any structural material should possess is resistance to crack propagation under both static and cyclic loading conditions. Therefore, in order to embrace the concept of structural intermetallics, methods have been developed to incorporate crack growth resistance in these otherwise brittle materials. The toughening methods that have been developed fall under two classes: intrinsic or extrinsic toughening mechanisms [42-44].

Intrinsic toughening results when the microstructure exhibits an inherent resistance to crack propagation, attributable to grain morphology, ductility, bond strength, alloying elements and precipitates, that tend to alter or influence the dislocation mobility or plastic zone dimensions. In metals, intrinsic toughening is brought about by plastic deformation, where large plastic zone size and crack tip blunting ultimately lead to high toughness. From the nature of the intrinsic toughening process, it is readily apparent that intrinsic mechanisms are an inherent material property, *i.e.* independent of crack size or specimen geometry, and occur ahead of the crack front.

However, intermetallics and ceramics, in general, have very little or no dislocation motion, and hence exhibit very little inherent or intrinsic crack propagation resistance. In such highly brittle materials, unstable fracture and subsequent failure occurs when the applied stress intensity factor (or crack driving force) reaches the material's fracture resistance, K_{Ic} (or G_{Ic}), and is nearly constant during further crack extension. In brittle materials, extrinsic toughening can be used very effectively to increase toughness by creating a process zone behind the crack front that acts to shield the far-field driving forces. Since extrinsic toughening occurs in the crack wake, extrinsic mechanisms are dependent on specimen geometry and crack dimensions. When extrinsic mechanisms are active, the crack driving force (or stress intensity) necessary to extend the crack increases from an initial value K_N, (initiation toughness) to a certain value K_R, usually denoted as R. Thus, a plot of K_R (or R) *vs*. crack extension, Δa, is called the resistance curve (or R-curve), and such increasing crack resistance behavior is termed R-curve behavior. Other intrinsic toughening methods, like transformation toughening, impart resistance-curve behavior for certain classes of ceramics [45].

Toughening in brittle ceramic/intermetallic systems is typically achieved through ductile reinforcements, where the plastic work of the deforming ductile phase is utilized to increase energy dissipation. The ductile ligaments that span the crack wake apply crack bridging tractions over the bridging length, thus shielding the crack tip from external loads. A number of ductile particulate reinforced brittle matrix composites have been studied in detail. The known studies include γ-TiAl/Nb [46], γ-TiAl/TiNb [7], $MoSi_2$/Nb [11, 47], Nb_3Al/Nb [21] and others [48-51]. The ductile inclusions are usually in the form of particles [6, 7, 11, 13, 21, 46, 47, 49, 52-54] or fibers [20, 48, 51, 55-58].

A common feature in all these brittle systems after reinforcement is that they exhibit pronounced resistance curve (R-Curve) behavior, *i.e.* resistance to crack propagation, wherein the stress intensity factor (K_R) increases with increasing crack length. For example, ductile phase toughening induced by incorporating Nb particles enhanced the toughness of Nb_3Al from ~1 to 6 MPa√m [21]. In the $MoSi_2$/Nb system [11], the crack resistance improved from a critical value (K_{IC}) of 5 MPa√m for unreinforced $MoSi_2$ to ~13 MPa√m steady state fracture toughness, whereas, the toughness of γ-TiAl/Nb [4] increased from 8 MPa√m to ~25-30 MPa√m.

Investigations on γ-TiAl/TiNb [6] showed an increase in crack initiation toughness from 8 MPa√m to 16 MPa√m, nearly twice that of monolithic γ-TiAl, finally reaching a steady state (K_{SS}) value of 44 MPa√m.

The concept of laminating various metals and alloys resulting in composites that exploit unique properties of the constituent materials has been known for a very long time [41]. Nevertheless, in the light of developing structural intermetallic composites, the idea has been once again embraced as a potentially useful engineering approach. Over the past decade, a number of diverse brittle intermetallics and ceramics have been toughened with various ductile metal laminates [14-19, 22-26, 31-33, 39, 40, 51, 59-80]. A number of these laminate systems were originally conceived and developed with an aim of increasing crack propagation resistance in brittle components used for high temperature aerospace applications [29, 81-83].

Numerous studies have illustrated the benefits of a laminate architecture to fracture resistance. Fracture toughness tests have been conducted on a variety of laminate composite systems [4, 6, 7, 14-17, 19, 22-24, 26, 40, 51, 60, 62-65, 69, 72-75]. In one study, fracture resistance of Nb_5Si_3 intermetallic was increased by a factor of five, from 1.7 MPa√m to 8.6 MPa√m, by reinforcing with ductile Nb layers (in the arrester orientation, AO) [64], while in another investigation an improvement from 2 MPa√m to nearly 28 MPa√m was attained after a crack extension of 400μm [65]. $Nb/MoSi_2$ laminates (AO) showed better fracture properties than composites reinforced with ductile particles or fibers [51].

Nb/Nb_3Al laminate composites have been similarly studied in depth with regards to the influence of layer thickness and orientation [21]. In both orientations, divider and arrester, the laminates toughened in an R-curve fashion, with progressive improvement in toughness properties as the reinforcement layer thickness was increased. While a crack initiation toughness of 1 MPa√m was noted in divider orientation for all specimens (same as the toughness of brittle Nb_3Al), crack initiation toughness values as high as ~7 MPa√m were observed in the arrester orientation. The toughness increased to over 10 MPa√m, with the increase in metal layer thickness from 50μm-250μm. The effect of laminate orientation on overall toughness was relatively small, with

arrester orientation samples exhibiting slightly better properties over the divider orientation samples.

Enoki *et al*., [60, 62], and Harach *et al*., [26], have showed that peak toughness and resistance curves improved commensurately with increasing volume fraction in laminate composites. In fact, these are the only known studies on the effects of volume fraction on toughness for laminate composites. In Ni/NiAl laminates, the maximum fracture resistance measured was 17.5 MPa√m in the divider orientation and 23.5 MPa√m in the arrester orientation [62]. Interestingly, in the Ti/Al$_3$Ti laminates, crack initiation toughness was higher in divider laminates compared to arrester laminates with the same volume fraction of Ti [26].

Studies on TiNb/γTiAl, Nb/MoSi$_2$ and Nb/Nb$_3$Al [4, 6, 12, 15, 22] have all illustrated benefits of ductile phase toughening with particles, wires and laminates. Additionally, these studies confirmed the superiority of laminates over wire and particulate reinforcements in terms of toughness gains. However, further investigations on cyclic loading effects have severely undermined the use of particles and wires as potential reinforcements due to near elimination of toughening effects as a result of premature ductile ligament failure. As a result, designing laminates against both static and cyclic loading effects is paramount to the development of these composite towards structural uses. Hence in the current work, effects of ductile layer thickness and volume fraction on fracture toughness and resistance-curve behavior of Ti-Al$_3$Ti MIL composites are investigated.

However, a large body of research has been directed towards the characterization of ductile-reinforced, brittle composite systems with reinforcement morphology other than laminates. Investigations on laminate composites have been confined to metal-intermetallic "microlaminates", with layer thickness in the range of 1 μm to 250 μm [14-19, 23-25]. Relatively little is known about the mechanical properties of metallic-intermetallic composites including the Ti-Al$_3$Ti combination. The impediment towards such characterization is the difficulty in developing bulk composites of sufficient size for testing. However, the novel one-step process [30] used in the development of MIL composites produces fully dense laminate composites with layer thickness from 200 μm to > 4mm, and overall sample sizes that do not

appear to be limited in overall lateral dimensions or thickness. These composites can be designed for structural applications by optimizing the constituent properties over laminate architecture (layer thickness, percentage composition of titanium, starting material type) and processing history.

II. EXPERIMENTAL PROCEDURES

Metal-intermetallic laminate (MIL) composites are a unique form of composites, in which alternating metallic and intermetallic layers are created through a reaction between a low melting temperature metal, such as Al, and a high melting temperature metal, such as Ti (see Figure 3-1). Sheet metal of Ti-6Al-4V and 1100 aluminum were used to fabricate Metal-Intermetallic (Ti-Al_3Ti) Laminate (MIL) composites by a novel one-step process that utilizes a controlled reaction at elevated temperature and pressure [30]. For this study the initial thickness of starting foils was chosen in such a way that all of the aluminum was consumed in the reaction with the adjacent titanium to form the aluminide (Al_3Ti), while leaving some unreacted Ti. The final structure, therefore, consists of alternating layers of ductile metal (Ti) and the brittle intermetallic (Al_3Ti).

The MIL composite so produced is lighter (~3.7 g/cc) than steel alloys (~8 g/cc), and yet has an elastic modulus ~195 GPa, close to that of steel (~200GPa). However, the most impressive gain is the higher resistance to crack propagation, *i.e.*, high toughness achieved in an otherwise brittle structure. The composition, layer makeup and the mechanical properties of the final MIL composite can be varied systematically by varying individual starting foil thickness, composition and layering sequence. Therefore, a thorough understanding of such structure-property relationships is essential in extending the capability of this new class of composite as structural components.
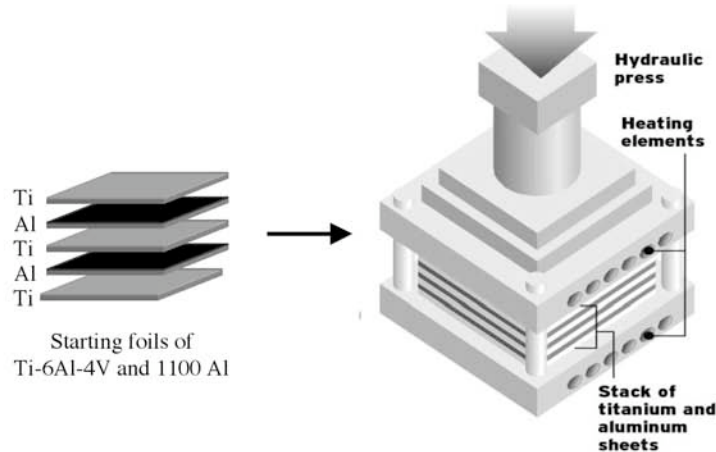
Figure 3-1.   Schematic diagram of metal-intermetallic laminate (MIL) composite fabrication apparatus.

R-curve behavior of the laminates in the divider orientation was tested in two different ways, wherein crack opening displacement (COD) gages and crack propagation gages (CPG) were used to monitor the crack length. In both cases, single-edged notched bend beams, SE(B) (see Figure 3-2), were tested under three-point bend loading in accordance with the ASTM E-399 standard. The three-point bend tests were performed under position control with an actuator speed of 0.1 mm/min at room temperature.
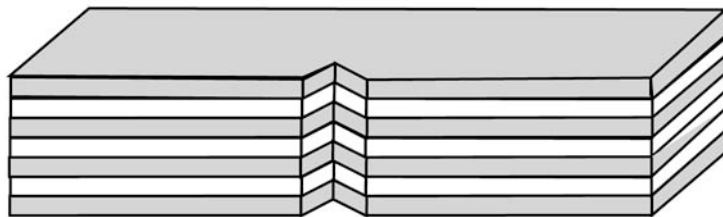
Figure 3-2.   Schematic diagram of Crack-Divider Orientation in the MIL composite in the SE(B) geometry.

The typical span was either 77 mm or 102.4 mm, and the ratio of width to thickness varied between 2-4, within the limits recommended by ASTM E-399. All the samples were notched using a low speed saw utilizing a diamond blade of thickness 0.25 mm.   The samples were subsequently fatigue pre-cracked to an a/w ratio (crack length/sample width) of nearly 0.5. Fatigue pre-cracking was performed in constant $\Delta K = 5$ MPa$\sqrt{}$m mode and at 10 Hz cyclic (sine wave) frequency at a load ratio (R) equal to 0.2. During fatigue pre-cracking the crack length was monitored indirectly by a COD gage that calculates the crack extension through the increase

in the specimen compliance. The entire resistance curve was evaluated up to $a/w = 0.7 - 0.8$, and the tests were performed in open air at 22°C. Fatigue pre-cracking of the bend specimen is required to mimic a naturally occurring crack in a structural member. Additionally, a set of notched specimens were tested without any fatigue pre-cracking in order to compare the influence of fatigue pre-cracking on the bridging behavior and hence fracture properties.

In the first method, crack opening displacement (COD) gages were used to measure the crack length indirectly by measuring the change in compliance of the specimen during loading. This compliance change was then used to evaluate the crack length and fracture toughness (COD R-curve) using linear elastic solutions (see Appendix A for calculations).

In the second method, crack propagation (CP) gages were used to monitor the crack in the titanium layer on one face of the sample. Crack propagation gages (Model 1-RDS-22) were obtained from Hottinger Baldwin Messtechnik (HBM) and is schematically shown in Figure 3-3 with respect to the specimen and crack geometry. The crack propagation gages consist of 50 strands of resistive wires, each of 44Ω resistance, connected in parallel. As the crack propagates, it breaks the resistive wires, thus changing the resistance of the entire strain gauge. Such a change can be detected and amplified by using a 1/4 bridge circuit as shown in Figure 3-4. Since the resistive strands are separated uniformly by a distance of 0.1 mm, the crack length on the titanium face can be accurately monitored. This is similar to optically measuring the crack length, where the crack growth is monitored directly by calibrating an imaging system with uniformly spaced markings on the specimen surface. This crack length is then used in Equations A1 – A4 (given in Appendix A) to evaluate the R-curve behavior (CPG R-curve).

While the crack propagation gage measures directly the crack length in the ductile phase, there is no direct method of determining the crack front embedded in the brittle Al_3Ti layers that are sandwiched between the external Ti layers. Hence, a COD gage determines the crack length in the specimen indirectly by converting the increase in compliance during loading due to damage (in the form of brittle intermetallic cracking and crack extension in the Ti layer) into an equivalent crack length. It will be explained in the next section that, in many cases, a clear crack front is very difficult to define and hence conservative estimates obtained from the COD gage is

used in conjunction with CPG readings to estimate the extent of bridging. This is the reason for using two different approaches to measure the crack length. Additionally, a compact tension (CT) Ti-6Al-4V bulk specimen was also tested under monotonic loading at 0.1 mm/min to evaluate and compare fracture toughness with respect to the MIL composites.
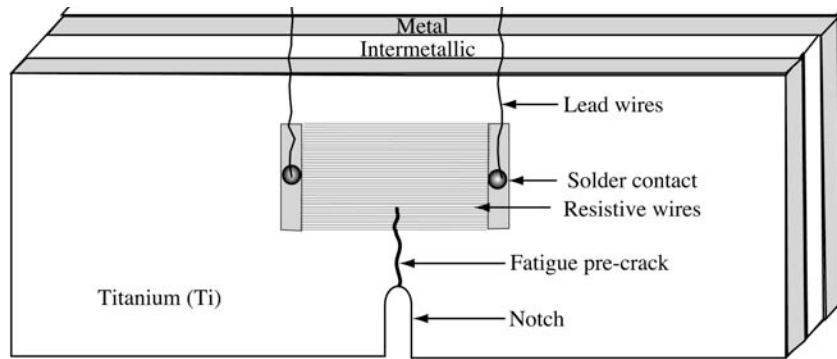
Figure 3-3.   Crack propagation gage set up for measuring crack length in a SE(B) specimen during R-curve testing.

In addition to the fracture tests, fatigue-crack propagation tests [84] were also performed on the laminate composites with single-edged-notch bend, SE(B), geometry according to ASTM standard E647 specifications. The general specimen dimensions for SE(B) specimen were in the range of width (W) = 18 to 26mm, thickness (B) = 9 to 14 mm, and span (S) = 77 or 107.2 mm. All samples were fatigue tested at room temperature (22°C) at a cyclic frequency of 10 Hz (sine wave). Increasing ΔK ($\Delta K\uparrow$) and decreasing ΔK ($\Delta K\downarrow$) tests were performed at a stress ratio (K_{min}/K_{max}) $R = 0.1$, in order to generate both high crack growth rate ($1 \times 10^{-1} > da/dN > 1 \times 10^{-5}$ mm/cycle) and low crack growth rate ($1 \times 10^{-5} > da/dN > 1 \times 10^{-7}$ mm/cycle) data, respectively. ΔK in all the tests was controlled according to standard load shedding techniques and is given by the equation:

$$\Delta K = \Delta K_0 \exp(-C(a_{i+1} - a_i))$$

where ΔK is the stress intensity factor range, ΔK_0 is the initial stress intensity factor range, C is the stress intensity factor gradient, and a_{i+1}, a_i are the instantaneous and initial crack lengths respectively. For ΔK decreasing tests, C values between -0.08 mm^{-1} to -0.15 mm^{-1} were used and C values between 0.08 mm^{-1} to 0.25 mm^{-1} were used in ΔK increasing tests.

Table 3-1 lists the representative MIL composites composition used to fabricate SE(B) specimen in the crack-divider orientation. Henceforth, the samples will be designated by the volume fraction of Ti. For example, 20Ti refers to a SE(B) specimen with a Ti volume fraction of 20% in a crack-divider orientation. The resulting layered structure of the MIL composites is shown in Figure 3-5. The average grain size of Al_3Ti in the MIL composites shown in Figure 3-6 was estimated using ASTM E112 line-intercept procedure. The optical micrographs of the corresponding ductile phase microstructure are also shown.
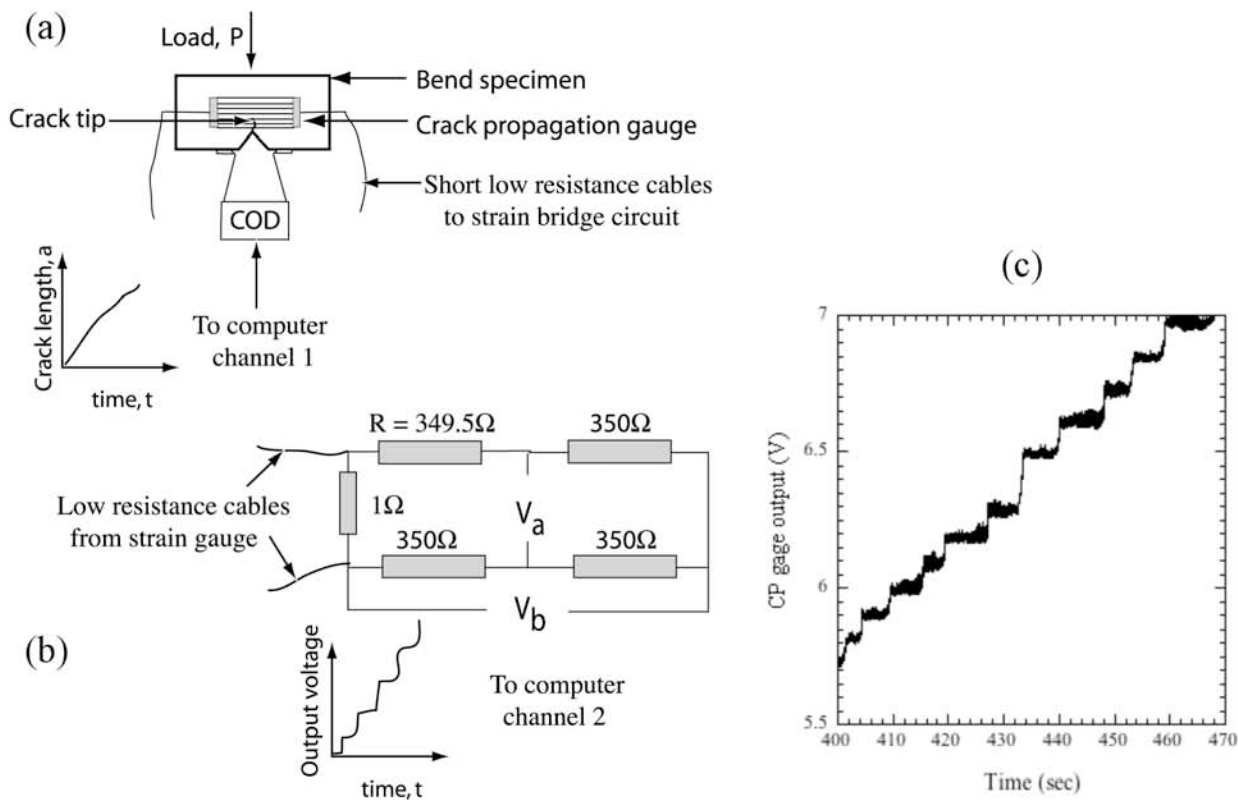
Figure 3-4.   (a) Schematic illustration of the strain gages used in fracture tests. (b) Schematic drawing of Strain gage amplifier, 1/4 bridge circuit for measuring the crack length on one face of the bend specimen. (c) Data recorded from the crack propagation gage during crack growth in a MIL composite. Note the step output from the CP gage where each step represents change in voltage due to a single broken resistive wire (only a portion of the actual output is shown here).

Table 3-1.   Effective thickness and volume fraction of constituent layers in MIL composites fabricated in divider orientation of SE(B) and CT geometry.

Sample	Starting foil thickness (μm)		Final layer thickness (μm)		Volume fraction (%)		No. of layers		Measured density
SE(B)	Ti	Al	Ti	Al$_3$Ti	Ti	Al$_3$Ti	Ti	Al$_3$Ti	g/cc
18Ti	508	813	206	968	17.5	82.5	10	9	3.55
24Ti	508	508	269	833	24.4	75.6	10	9	3.60
25Ti	1016	1270	579	1644	25.0	75.0	6	5	3.64
33Ti	862	813	502	1030	32.8	67.2	9	8	3.70
40Ti	508	381	322	477	40.3	59.7	22	21	3.83
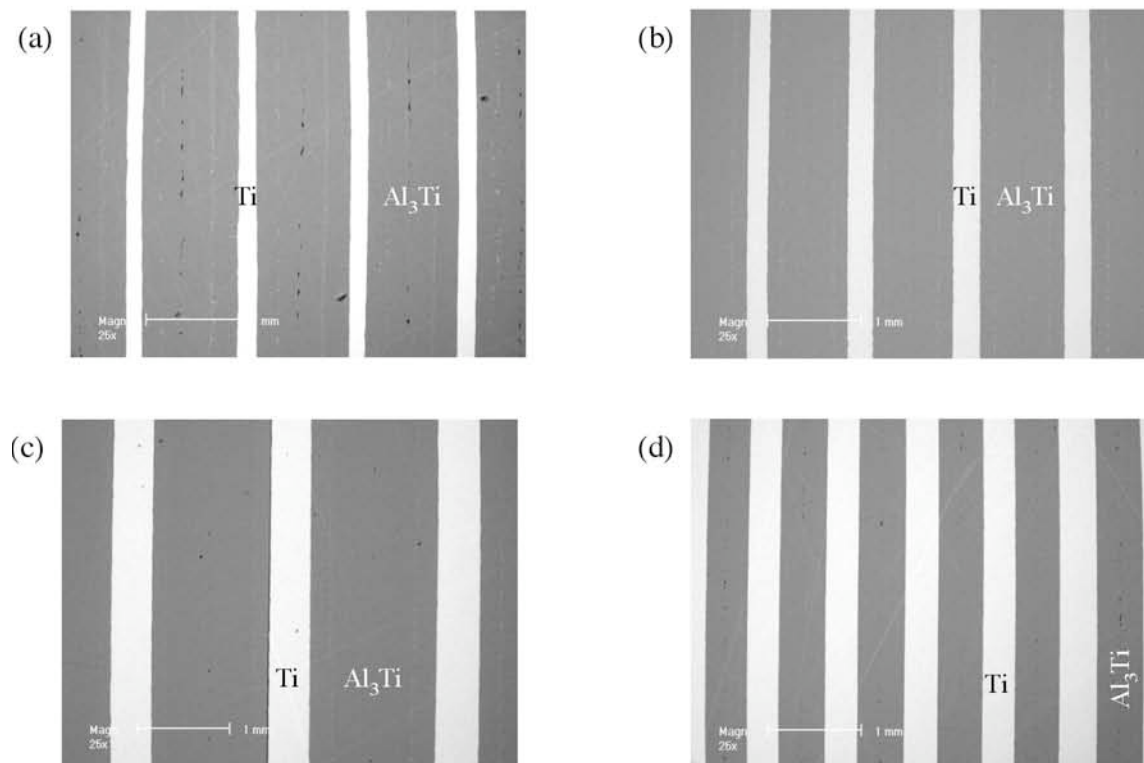
Figure 3-5.   Scanning electron micrographs of MIL composites (through-thickness section). (a) 18Ti (b) 24Ti (c) 33Ti (d) 40Ti. The scale bar is 1mm in all the micrographs.
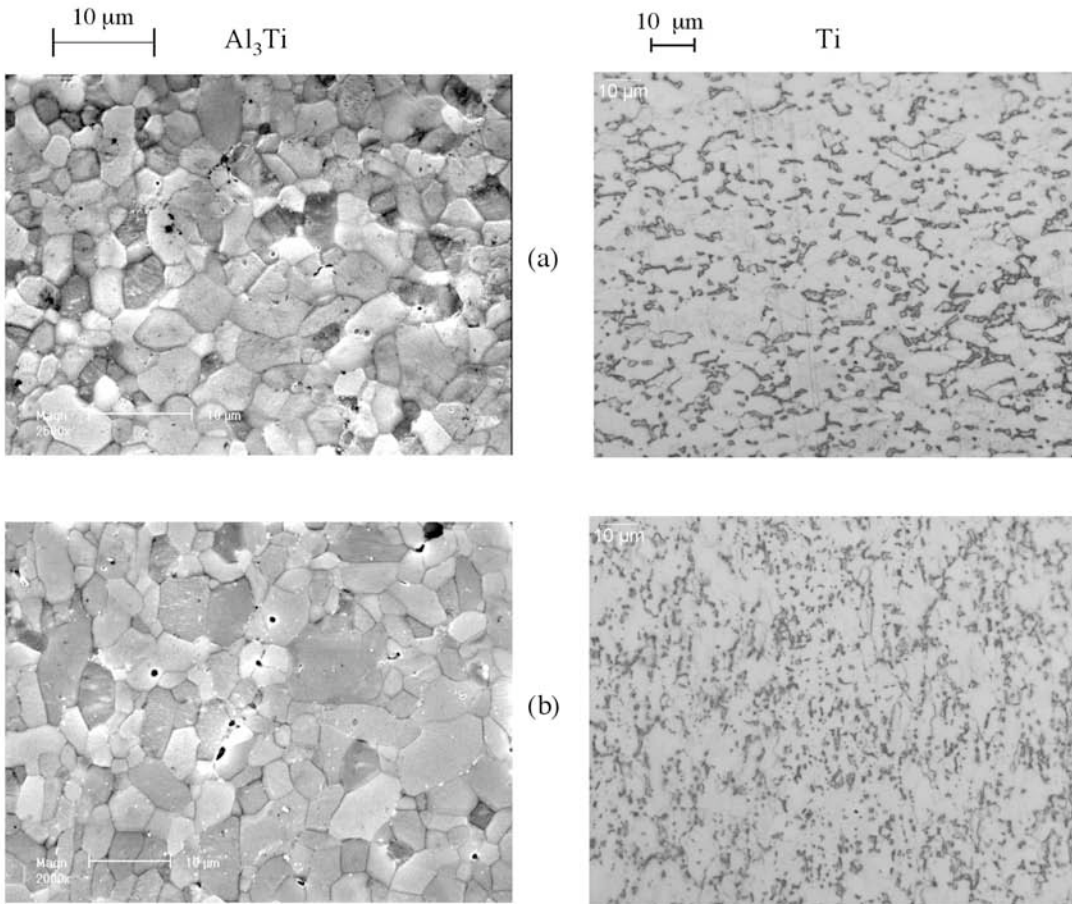
Figure 3-6.   Microstructure of Al$_3$Ti (secondary electron SEM image) and Ti (optical micrographs) in MIL composite: (a) 21Ti (2.6 μm Al$_3$Ti) (b) 33Ti (3.5 μm Al$_3$Ti).

III. RESULTS AND DISCUSSION

A. Monolithic Ti-6Al-4V and Al$_3$Ti materials

The R-curve for Ti-6Al-4V is shown in Figure 3-7 along with the fracture toughness of Al$_3$Ti, which indicated as a horizontal line. The initiation toughness (K_N) for Ti-6Al-4V is observed at ~ 71 MPa√m, consistent with the K_{IC} reported for bulk Ti-6-4 alloys (~ 75 MPa√m).
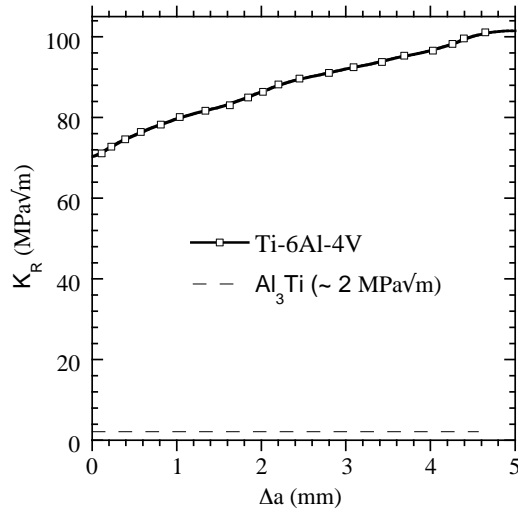
Figure 3-7.   R-curve behavior in monolithic Ti-6Al-4V. The fracture toughness of Al₃Ti is shown as a dotted horizontal line at ~ 2 MPa√m.

B. *Metal-Intermetallic Laminate (MIL) composites*

The R-curves or fracture resistance curves for divider laminates shown in Figure 3-8 indicate that ductile reinforcements in the brittle intermetallic improved resistance to crack propagation by more than an order of magnitude (Al₃Ti K_{IC} ~ 2 MPa√m). The crack length measurements used to calculate the fracture toughness curves in Figure 3-8(a) were determined by a crack opening displacement (COD) gage. With an increase in the ductile phase volume fraction from 18 to 40%, peak toughness values increased in general from 75 to 96 MPa√m (note that the Ti layer thickness also varied between 206μm – 579μm), on par with monolithic Ti-6Al-4V fracture toughness of 75 MPa√m (see Table 3-3). The results for the 25Ti sample did not follow the above trend as clearly as the other volume fraction samples did. The crack growth resistance exhibited by the MIL composites exceeded the fracture resistance of many ductile particle or wire reinforced brittle composites [6, 7, 11, 13, 20, 21, 46-49, 51-58]. All six laminates tested in crack divider orientation exhibited an initiation toughness of ~ 9 MPa√m. Until 2 mm crack extension *(*i.e. as measured by COD gage, Δa_{COD}), the fracture resistance data nearly overlapped, *i.e.*, the R-curve possessed a common slope in all the tests. However, when the stress intensity increased to ~ 20 MPa√m, individual R-curves monotonically increased, with their slope increasing in general with increasing Ti volume fraction.
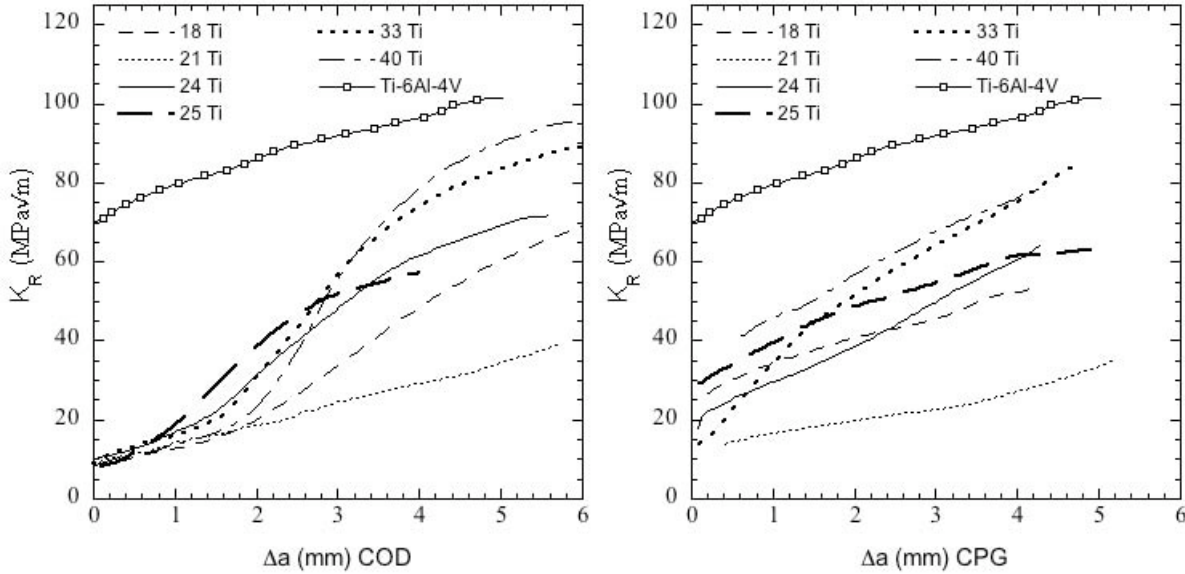
Figure 3-8.   R-curves for divider laminates. (a) K_R-Δa_{COD}, crack length was monitored using COD gages. (b) K_R-a/w, crack length was monitored using CP gages.

Since it was difficult to place the crack propagation gages in such a manner that the first resistive wire in the gage is immediately ahead of the crack-tip, the first data point on the plots shown in Figure 3-8(b) correspond to a stress intensity at a finite crack growth length (< 0.1mm, as measured by CP gage), and this occurred when a_{COD} was ~2mm. Therefore, R-curves calculated using a_{CP}, indicated a 'near' initiation value (K_N) greater than or equal to 20 MPa√m. Since the COD gage determines crack length through elastic compliance of the specimen, and since the R-curves in Figure 3-8a showed two distinct slopes at ~20 MPa√m, indicating a sudden change in compliance, it is inferred that the ductile reinforcement provided nearly 2mm bridging length before crack initiation in the Ti.

It is assumed here, however, that the crack front in all Ti layers is straight, *i.e.*, the crack front at the center of specimen thickness does not extend further than the crack front on the surface Ti layers. Such an assumption, although not strictly justified, is expected to give reasonable estimates of average crack length as measured by the crack propagation gage (a_{CP}.).

Thus, such crack tunneling behavior in Al_3Ti, where the crack front in the intermetallic layers extends further than the crack front in the Ti layers, and subsequent bridging by intact ductile layers, was the primary cause for enhancement in crack growth resistance in laminate

composites. Figure 3-9 shows the evidence for crack tunneling behavior in the MIL composite. Figure 3-9(a) shows extensive damage in the brittle Al_3Ti, where cracks tunneled nearly 2mm ahead of the crack in the Ti layer (as measured by CP gage), forming non-coplanar or non-collinear cracks. Clearly, a dominant single crack front or a crack tip is extremely difficult to define or identify. The cross-section in Figure 3-9(b), taken 3 mm ahead of the Ti layer defined crack tip, shows that although non-coplanar cracks formed, the extent of brittle cracking is greatly reduced. Bridging lengths of ~2–3 mm were found in all the laminates, that compares well with the estimates suggested by the COD gage measurements earlier.

The fracture surfaces for 33Ti laminate composite are shown in Figure 3-10. The micrograph in Figure 3-10(a) shows the fracture surfaces of the individual layers, with Ti layers indicating slant fracture. Earlier work [66, 67] has shown that non-coplanar cracking (or slant fracture) leads to a larger work of rupture and hence higher toughness. The fracture surface of a single Ti layer, shown in Figure 3-10(b), reveals the angled fracture surfaces and extensive cracking in the Al_3Ti layer near the interfaces. The near interfacial cracking is evident at the region where the fatigue pre-crack ended (in Ti layer) and the crack started to grow under monotonic loading during R-curve testing. Magnification of this fatigue-R-curve crack interface in Figure 3-10(c) reveals a transition from flat, transgranular fracture under cyclic loading to a more ductile dimpled failure due to microvoid coalescence under monotonic loading. The fracture surfaces of the brittle intermetallic in Figure 3-10(d) indicate a mixture of intra-granular cleavage fracture and intergranular fracture.

In the divider orientation, the crack front is exposed to both the brittle and ductile layers at all times. Due to the rapid tunneling of the crack into the brittle intermetallic, the crack front in this microstructural layer extends further than the crack front in the ductile Ti phase, thus leading to the formation of the ductile bridging zones. However, after a certain amount of crack growth, the bridging metal ligaments farthest from the crack tip fail due to plastic stretching beyond a critical displacement (u^*), and a steady state is reached between crack growth and ligament failure. This leads to a steady state toughness value and the R-curve assumes a plateau form, *i.e.*, it saturates. Since, the crack front is embedded in the ductile phase all the time, the steady state values achieved in laminates are often higher compared to particulate or fiber reinforcements,

where crack growth occurs primarily in the brittle matrix. Such contrast in R-curve behavior has been verified by Bloyer *et al*. [15].

In the present study, the bridging lengths (~2-3 mm) observed in the laminates are large with respect to the crack length (*a*) or specimen ligament (*w-a*) (*w* = 19-26 mm, see Table 3-3). Hence, in this case, large-scale bridging conditions prevail and any assumptions of small-scale bridging may lead to incorrect estimates of true toughness values.
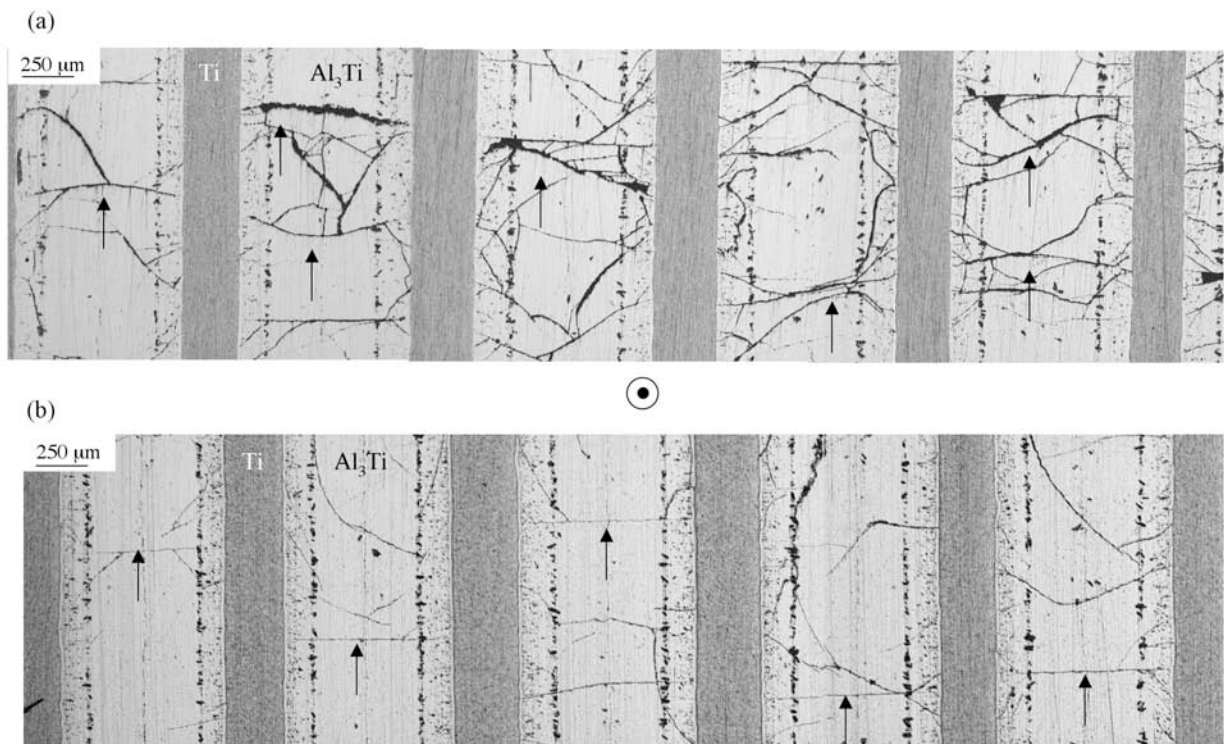
Figure 3-9.   Optical micrographs of crack fronts in a laminate composite during R-curve testing (crack plane growth is horizontal and into the plane of the page). (a) The crack front shown here is nearly 2 mm ahead of the crack tip in the Ti layer (measured by the CP gage), suggesting tunneling of the cracks into the brittle Al$_3$Ti layer. The cross-section also shows extensive non-coplanar cracking and hence a dominant or single crack front is difficult to define. (b) The crack front at nearly 3 mm ahead of the apparent crack tip. The arrows indicate cracks that have tunneled through the brittle layer; only a few are identified. The images refer to the cross-section BB$^|$ in Figure 3-11. Similar sectioning of the sample further ahead of the crack tip revealed almost no cracking of the intermetallic phase.

Figure 3-10. SEM images of fracture surface in the 33Ti laminate. (a) Fracture surfaces of Ti and Al$_3$Ti layers. (b) Ti-Al$_3$Ti interface. Observe the near interfacial cracking in the brittle phase. (c) The dotted curve separates the fatigue pre-cracked region from the monotonic fracture surface. A change from flat, transgranular crack growth to a more ductile dimpled failure can be observed in Ti layer. (d) predominantly mixed-mode intra-granular and intergranular fracture of Al$_3$Ti.

C.   Models for toughening in laminates

From the above results, it is evident that the toughening in MIL composites is due to extensive crack bridging by intact Ti layers that shield the crack tip. The contribution of ductile tractions in reducing crack driving force (or increasing crack growth resistance) over appropriate bridging lengths can be evaluated using the weight function method. Figure 3-11 schematically illustrates the concept of bridging in both crack arrester and crack divider laminates. For the purpose of the present study, only the crack divider orientation is analyzed. The general problem depends on the form of the traction over the bridging length, specimen geometry and crack length. In such cases, the bridging contribution toward crack tip stress intensity reduction is given as [85-87]:

$$K_b = \int_b \sigma(\chi)\, m(\alpha,\chi)\, d\chi \tag{1}$$

where $\sigma(\chi)$ is the traction distribution function given as a function of distance $\chi = x/w$ behind the crack tip, $m(\alpha,\chi)$ ($\alpha = a/w$) is the weight function for a given specimen geometry, and b is the bridging zone length. The specimen width and the crack length are denoted by w and a, respectively.
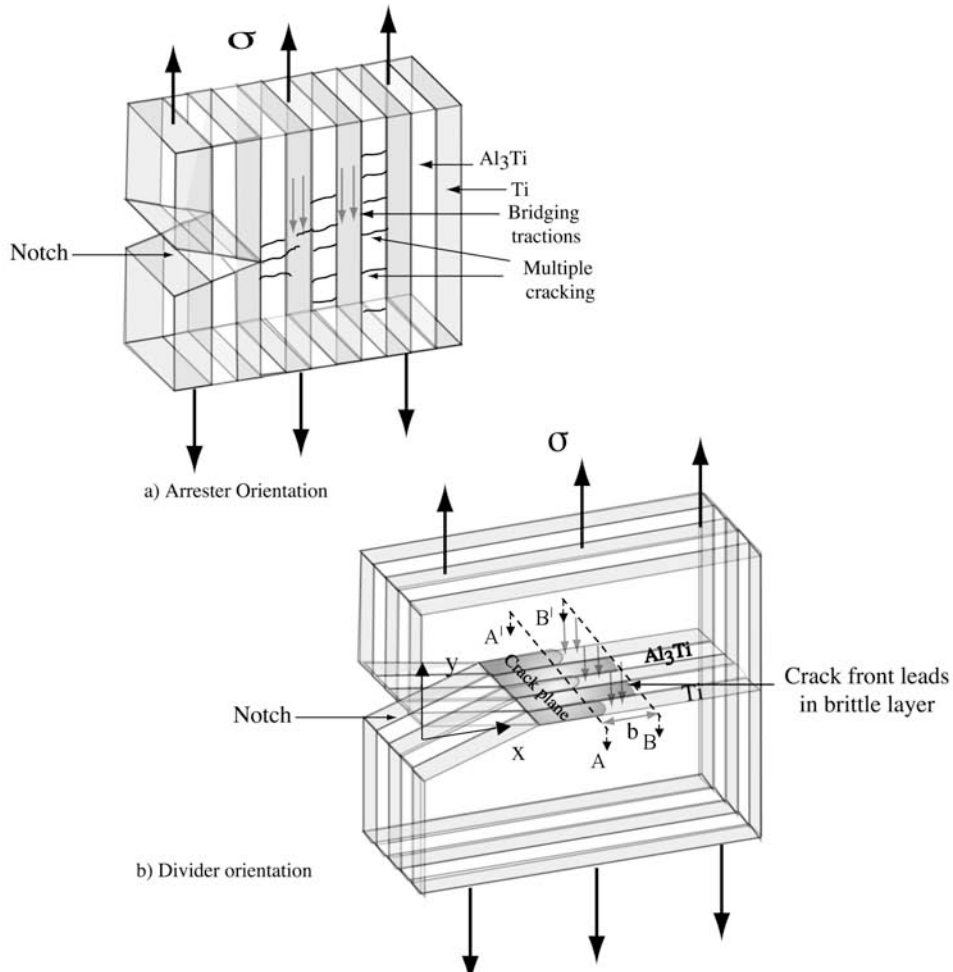
Figure 3-11. Schematic diagram illustrating crack morphology variation due to orientation effects in laminate composites: (a) crack arrester orientation (b) crack divider orientation. Planes $AA^|$ and $BB^|$ indicate cross sections of the laminate composite near the crack tip (see Figure 3-9 and Figure 3-20). The arrows between the planes indicate bridging tractions over the length b.

The effective stress intensity, K_{eff}, at the crack tip can then be given by superposing the bridging stress intensity, K_b, with intrinsic toughness (toughness of the brittle intermetallic) of the laminate composite, K_c:

$$K_{eff} = K_c + K_b \qquad (2)$$

In order to evaluate the bridging contribution from Equation 1, both the traction distribution function, and the weight function should be known in advance. However, the difficult part is calculating the traction distribution function, and for many cases it cannot be determined theoretically. The traction function, $\sigma(\chi)$, depends on the stress-displacement, $\sigma(u)$, behavior of the constrained ductile phase undergoing deformation and the crack-opening profile, $u(\chi)$. Therefore, direct experimental measurements are required (such as sandwich experiments [58, 66, 67, 88, 89]) to calculate these functions. Some models try to incorporate general empirical non-linear functions such as [75]:

$$\frac{\sigma}{\sigma_0} = \left[1 - \frac{u}{u*}\right]^n \qquad (3)$$

where σ represents the tractions due to the bridging ligaments, σ_0 is the constrained maximum traction for a given ductile metal layer, u is the displacement of the crack faces, $u*$ is the critical crack opening displacement at which the tractions no longer exist on the crack faces, and n is a power index.

Evidently, $\sigma(u)$ is dependent on many factors such as specimen geometry, reinforcement geometry, and loading conditions, and hence are very difficult to model. The simplest approximation is obtained through a rectilinear bridging traction law [53] given by:

$$\frac{\sigma(u)}{\sigma_0} = \varsigma = \begin{cases} 1, & 0 \le \dfrac{u}{u*} \le 1 \\ 0, & \dfrac{u}{u*} \ge 1 \end{cases} \qquad (4)$$

and

$$\sigma_0 u* = \int_0^{u*} \sigma_e(u) du \qquad (5)$$

where $\sigma_e(u)$ is the stress-displacement curve measured experimentally. Constrained stress-

displacement curves have been determined for a number of systems [22, 25, 64, 66, 67], however, a simplified approach is to assume a constant $\sigma(\chi)$ [15, 17, 90], equal to the constrained flow stress of the ductile reinforcement over the entire bridging length. In Ti-Al$_3$Ti MIL composites, constrained tensile tests have indicated constrained flow stress ratios less than 1.1 [91]. Therefore, $\sigma(\chi)$ in this study is assumed to be the uniaxial yield strength of Ti-6Al-4V ($\sim$ 970 MPa). The layered architecture of the Ti layers is accounted for by the volume fraction, f, in the equation:

$$K_{eff} = K_c + f\,\sigma_0 \int_b m(\alpha,\chi)\,d\chi \qquad (6)$$

The assumption of a constant $\sigma(\chi)$ in the above model has had some success before [15, 90]. Zok and Hom [90] have pointed out that once the ductile bridging ligaments furthest from the crack tip fail, a steady state value is attained by both the bridging length and the R-curve behavior. Furthermore, they suggested that such R-curve saturation is observed during small scale bridging (SSB), where the bridging lengths are small compared to the crack length (a) and the uncracked ligament (w-a) dimensions:

$$\frac{b}{a} \to 0 \quad and \quad \frac{b}{(w-a)} \to 0 \qquad (7)$$

The weight function for a single edge-cracked finite width specimen, $m(\alpha,\chi)$, in Equation 1 is given by [92]:

$$m(\alpha,\chi) = \frac{1}{\sqrt{2\pi\alpha}} \sum_{n=1}^{5} \xi_n(\alpha)\left(1-\frac{\chi}{\alpha}\right)^{n-\frac{3}{2}} \qquad (8)$$

where $\alpha = \dfrac{a}{w}$; $\chi = \dfrac{x}{w}$ and the function values, $\xi_n(\alpha)$, for some values of α are listed in Table 3-2. It should be noted that x is measured from the load line to the crack tip. Therefore, the stress intensity for any arbitrary crack face loading, $\dfrac{\sigma(\chi)}{\sigma}$ can be evaluated as follows:

$$K = Y\,\sigma\,\sqrt{\pi\alpha w} \qquad (9)$$

where σ is a far-field stress chosen as the reference stress to determine the appropriate weight function for the above geometry. The non-dimensional factor Y is determined as follows:

$$Y(\alpha,\chi) = \int_0^\alpha \frac{\sigma(\chi)}{\sigma} \frac{m(\alpha,\chi)}{\sqrt{\pi\alpha}} d\chi = \frac{1}{\sqrt{2\pi\alpha}} \int_0^\alpha \frac{\sigma(\chi)}{\sigma} \sum_{n=1}^5 \xi_n(\alpha)\left(1-\frac{\chi}{\alpha}\right)^{n-\frac{3}{2}} d\chi \tag{10}$$

When the crack is subjected to a uniform stress, $\sigma(\chi) = \sigma$, acting in the wake of the crack tip, the non-dimensional factor Y simplifies as:

$$Y(\alpha,\chi) = \frac{1}{\sqrt{2\pi\alpha}} \int_\chi \frac{\sigma(\chi)}{\sigma} \sum_{n=1}^5 \xi_n(\alpha)\left(1-\frac{\chi}{\alpha}\right)^{n-\frac{3}{2}} d\chi; \qquad \alpha-\beta \le \chi \le \alpha; \quad \beta = \frac{b}{w}$$

$$Y(\alpha,\frac{\beta}{\alpha}) = \frac{1}{\sqrt{2\pi\alpha}} \sum_{n=1}^5 \xi_n(\alpha) \int_{\alpha-\beta}^\alpha \left(1-\frac{\chi}{\alpha}\right)^{n-\frac{3}{2}} d\chi = \frac{1}{\sqrt{2\pi\alpha}} \sum_{n=1}^5 \xi_n(\alpha)\left(\frac{-2\alpha}{2n-1}\right)\left[\left(1-\frac{\chi}{\alpha}\right)^{n-\frac{1}{2}}\right]_{\alpha-\beta}^\alpha \tag{11}$$

$$Y(\alpha,\frac{\beta}{\alpha}) = \frac{\sqrt{2}}{\pi} \sum_{n=1}^5 \frac{1}{2n-1} \xi_n(\alpha)\left(\frac{\beta}{\alpha}\right)^{n-\frac{1}{2}}$$

which agrees with Wu and Carlsson [92]. The function $Y(a/w, b/a)$ is plotted for reference in Figure 3-21 (see Appendix B). Therefore, under large scale bridging (LSB) conditions, the bridging contribution to the stress intensity is given (after substituting for the variables α and β, and $\sigma = \sigma_0$) by:

$$K_b = \sigma_0 \sqrt{\pi a} \frac{\sqrt{2}}{\pi} \sum_{n=1}^5 \frac{1}{2n-1} \xi_n(\frac{a}{w})\left(\frac{b}{a}\right)^{n-\frac{1}{2}} \tag{12}$$

Figure 3-12 illustrates the manner in which Equation 12 is used to model the LSB conditions. For a given bridging length (b) and specimen width (w), the a/w ratio is varied by incrementing the crack length ($a/w = 0.5$-0.8 in this case, similar to the values used in the experiments). As the crack grows, both the a/w and b/a values change, and hence a rising R-curve, as shown in Figure 3-12c, is obtained from Equation 12. The assumption here, however, is that until the crack grows to a length equal to the bridging length, b_c, the bridging length value used in Equation 12 is equal to the crack increment (Δa). Once the entire bridging length forms in the immediate wake of the crack tip, it is assumed that a steady state bridging length is attained, and hence this steady state value is used thereafter to calculate the remaining portion of the R-curve (see Figure 3-12b).

Equation 12 is fitted to the experimental data in Figure 3-12 to estimate the bridging lengths for laminates with varying Ti volume fraction. The bridging lengths calculated varied between ~2-3

mm (see Table 3-2) agreeing well with the experimental observations. Nevertheless, there are a few differences to be noted between the experimental and the LSB model R-curves in Figure 3-13. The R-curve determined from the CP gage crack length measurements does not, in general, have a initial rise portion, since it only measures the crack increment in the Ti layer. Since the fatigue pre-cracking introduced bridging ligaments prior to the R-curve testing, the rise portion of the COD R-curve does not match closely to the model R-curves in some cases. As the experimental data limited the R-curves to be calculated up to 5-6 mm crack extension only, the model curves are presented accordingly. However, if one extends the model R-curves, they are similar to the curve schematically drawn in Figure 3-12c, clearly suggesting LSB conditions.
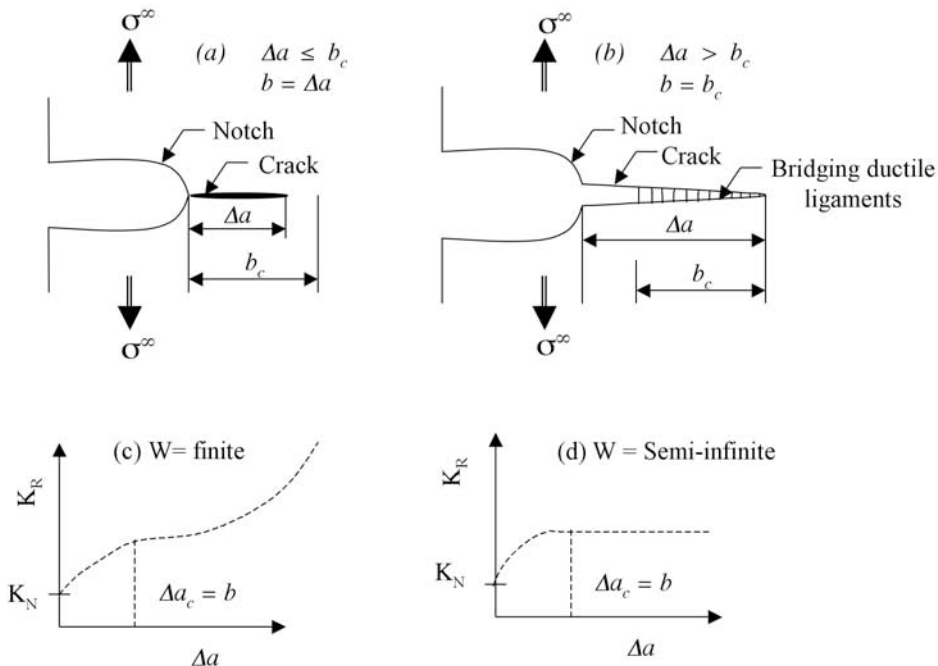
Figure 3-12. R-curve behavior under SSB and LSB conditions. (a) crack growth prior to reaching steady state bridging length. (b) crack growth and bridging ligaments after the attainment of steady state bridging length. (c) R-curve calculated under LSB conditions. (d) R-curve calculated under SSB conditions. Notice the saturation of R-curve under SSB to a steady state value, K_{SS}, compared to monotonically increasing function under LSB. K_N is the crack initiation toughness.

Since the volume of intermetallic that can fracture prior to ductile bridging ligament failure is higher in composites with low Ti reinforcement volume fractions, it is anticipated that bridging lengths would be higher in such laminates. However, no particular trend in bridging lengths with Ti volume fraction is observed. One of the reasons may be that the sample dimensions, and

hence net volume of intermetallic, varied among the laminates tested (compare width, *w*, in Table 3-2). This suggests that bridging length is strongly dependent on specimen geometry, particularly sample size. Therefore, bridging length for a given thickness and volume fraction of ductile layer may not be a constant, since it depends on sample geometry.
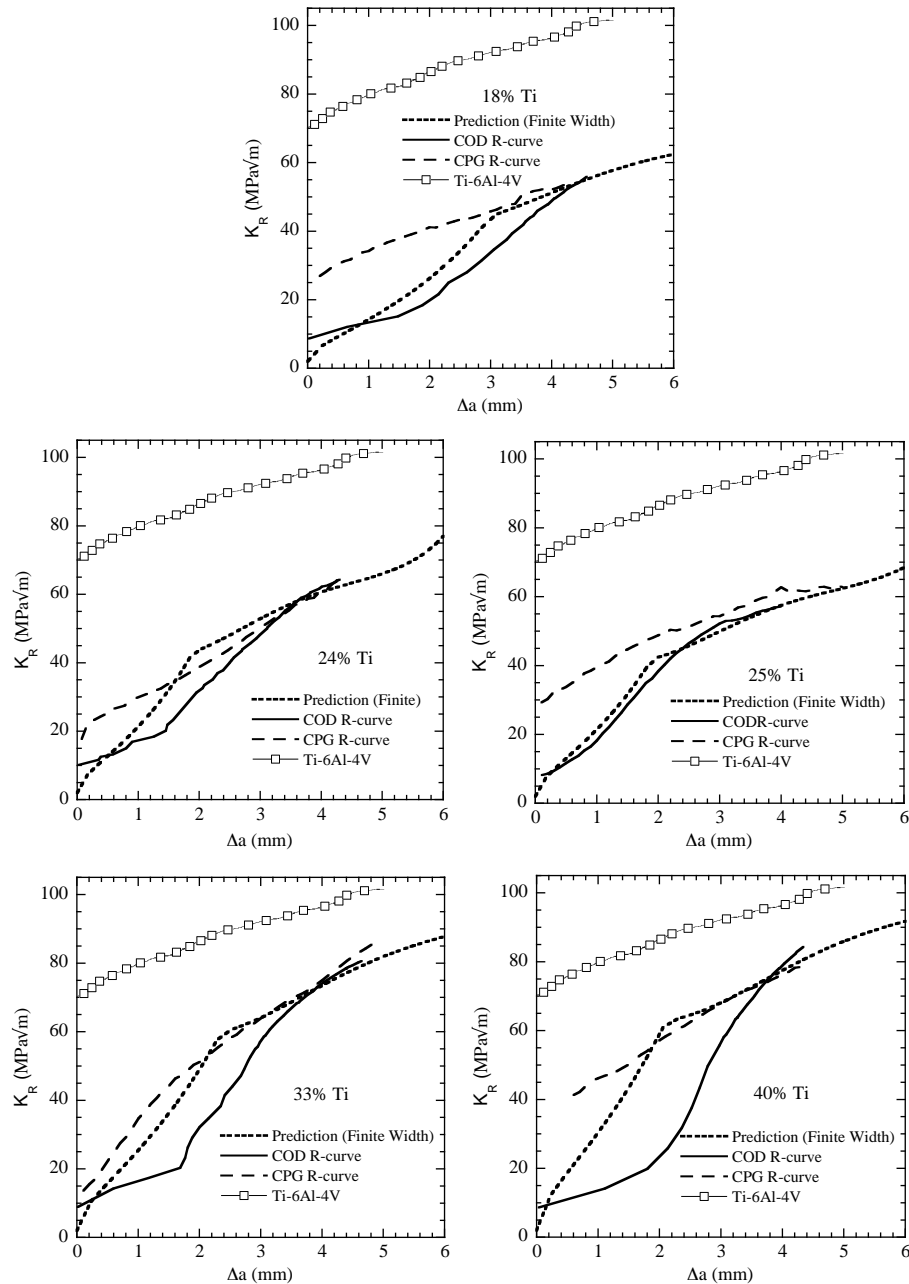
Figure 3-13.   Plots showing the LSB R-curve predictions (for a finite crack). The Ti volume fraction varied between 18% - 40%, indicated on the plots. The bridging length values used for the fit are given in Table 3-2. R-curve data for monolithic Ti-6-4 is also included in each plot for comparison.

Table 3-2.   Summary of fracture toughness values in divider laminates

MIL	%Ti	E' GPa Modulus	Ti layer thickness μm	$^1K_{SSB}$ MPa√m	K CP MPa√m	K_{SS} COD MPa√m	$^2K_{SS}{}^{SSB}$ MPa√m	$\Delta K^{Fatigue}$ ($K_C{}^{Fatigue}$) MPa√m	^3b *bridging length* mm	w finite width	w_∞ semi-infinite width
18 Ti	17.5	198	206	59	53	75	17.5	30 (34)	3	26.5	75
24 Ti	24.4	191	269	78	64	72	18.3	23 (26)	1.9	18.7	55
25 Ti	25	190	579	116	63	57	19.5	30 (34)	2	20.2	55
33 Ti	32.8	183	502	121	84	90	27	45 (50)	2.4	25.5	65
40 Ti	40.3	175	322	105	78	96	30.6	41 (46)	2.1	25.5	55

[1] Calculated from Equation 18; and [2]Equation 17; [3]Calculated from the model curve fit to experimental data

D. Small Scale Bridging (SSB) conditions

It was mentioned earlier that the bridging lengths (~2-3 mm) observed (or calculated) in the laminates were large with respect to the crack length (*a*) or specimen ligament (*w-a*), *i.e.*, Equation 7 is not satisfied, suggesting LSB conditions. Zok and Hom [90] have calculated (in fiber reinforced brittle-matrix composites) that for a steady state bridging length, b_c, of 1 mm and assuming an error of 10% due to large scale bridging, specimens with $w \geq 25$ mm and $a \approx 12$ mm would be required to measure the true resistance behavior. They showed that the R-curves obtained by testing smaller specimens overestimate the true fracture behavior, and thus called into question the validity of toughness data published for various ductile reinforced brittle composites. For the bridging lengths calculated in the case of these MIL composites, specimen with $w > 50$ mm and $a > 25$ mm would be required to capture the SSB conditions.

Steady state toughness values can, however, be calculated under SSB conditions, if the appropriate weight functions and bridging-zone size are known. The weight function for a single edge-cracked semi-infinite width specimen, $m(\chi)$, in Equation 1 is given by [92]:

$$m(\alpha,\chi) = \frac{1}{\sqrt{2\pi}} \sum_{n=1}^{5} \zeta_n \left(1 - \chi\right)^{n-\frac{3}{2}}$$

(13)

where the crack length, *a,* is chosen as the characteristic dimension (since it is a specimen with a semi-infinite width instead of finite width, *w*, as in Equation 8). Hence, $\alpha = \dfrac{a}{a} = 1$; $\chi = \dfrac{x}{a}$ and the function values, ζ_n, are listed in Table 3-5 (in Appendix C). Therefore, the stress intensity for

any arbitrary crack face loading, $\dfrac{\sigma(\chi)}{\sigma}$, can be evaluated in a similar way as Equations 8-12, as follows:

$$K = Y \sigma \sqrt{\pi a} \qquad (14)$$

where σ is a uniform crack face pressure loading chosen as the reference stress to determine the appropriate weight function for the above geometry. The non-dimensional factor Y is determined as:

$$Y(\alpha,\chi) = \int_0^\alpha \frac{\sigma(\chi)}{\sigma} \frac{m(\chi)}{\sqrt{\pi}} d\chi = \frac{1}{\sqrt{2\pi}} \int_0^\alpha \frac{\sigma(\chi)}{\sigma} \sum_{n=1}^5 \zeta_n (1-\chi)^{n-\frac{3}{2}} d\chi \qquad (15)$$

When the crack is subjected to an uniform stress, $\sigma(\chi) = \sigma$, acting in the wake of the crack tip, the non-dimensional factor Y simplifies as:

$$Y(\chi) = \frac{1}{\sqrt{2\pi}} \int_\chi \frac{\sigma(\chi)}{\sigma} \sum_{n=1}^5 \zeta_n (1-\chi)^{n-\frac{3}{2}} d\chi; \qquad 1-\beta \le \chi \le 1; \quad \beta = \frac{b}{a} = b$$

$$Y(\frac{\beta}{\alpha}) = \frac{1}{\sqrt{2\pi}} \sum_{n=1}^5 \zeta_n \int_{1-\beta}^1 (1-\chi)^{n-\frac{3}{2}} d\chi = \frac{1}{\sqrt{2\pi}} \sum_{n=1}^5 \zeta_n \left(\frac{-2}{2n-1}\right)\left[(1-\chi)^{n-\frac{1}{2}}\right]_{1-\beta}^1 \qquad (16)$$

$$Y(\frac{\beta}{\alpha}) = \frac{\sqrt{2}}{\pi} \sum_{n=1}^5 \frac{1}{2n-1} \zeta_n (\beta)^{n-\frac{1}{2}}$$

which agrees with Wu and Carlsson [92]. The function *Y(b/a)* is plotted in Figure 3-22 (in Appendix C). Therefore, under small scale bridging (SSB) conditions, the bridging contribution to the stress intensity is given by (after substituting for the variable α and β and $\sigma = \sigma_0$):

$$K = \sigma_0 \sqrt{\pi a} \frac{\sqrt{2}}{\pi} \sum_{n=1}^5 \frac{1}{2n-1} \zeta_n \cdot \left(\frac{b}{a}\right)^{n-\frac{1}{2}} \qquad (17)$$

Equation 17 is used in a similar manner as Equation 12 was used, and explained schematically in Figure 3-14(a-b). Using the bridging lengths and semi-infinite specimen width listed in Table 3-2, the SSB R-curves are calculated as shown in Figure 3-16. The SSB R-curves closely follow the same trend shown in Figure 3-14(d), *i.e.,* they all reach saturation and hence exhibit steady state toughness values (K_{SS}). The K_{SS} values varied between 18 and 30 MPa√m, still more than an order of magnitude greater than the intermetallic toughness (~2 MPa√m). However, the K_{SS}

under SSB conditions were nearly one-third the values seen in experimentally determined R-curves (see Table 3-2). As Zok and Hom [90] have pointed out, the LSB conditions may overestimate the true fracture behavior. However, the SSB values may be underestimating the true toughness values by nearly 10-20 MPa√m, for reasons discussed in the next section.

In the literature, an alternative energy approach, as formulated by Ashby and Bannister [66, 88, 89], is also used to estimate the SSB K_{SS}. The steady state toughness is calculated by combining the ductile reinforcement toughening and the matrix intrinsic toughness in the following form:

$$K_{ss} = \sqrt{K_c^2 + E' f \sigma_0 \chi t} \qquad (18)$$

where K_c is the matrix toughness, E' is the plane strain modulus of the laminate, f is the volume fraction of ductile reinforcement, t is the reinforcement size parameter, equal to half thickness for laminates, and $\sigma_0 \chi$ is the constrained flow stress of the ductile layer, equal to the Ti-6Al-4V yield strength (970 MPa in this case). The relevant parameters and the calculated K_{SS} values are given in Table 3-3. Although the steady state toughness calculated from Equation 18 agree closely with the peak R-curve values obtained from the experiments, they are nearly 3-4 times the values calculated under SSB conditions (see Table 3-2). Equation 18, therefore, seems to reflect the LSB rather than SSB conditions, contrary to previous suggestions by Bloyer *et al.* [15]. Nevertheless, it was pointed out that the energy formulation may over-predict the maximum toughness, and hence should be treated as an upper bound to the toughness achievable for ductile-phase reinforced brittle composites. It was further argued by Bloyer *et al.* that since the maximum toughness values calculated from the energy model are reasonably consistent with the measured values, in spite of their over-prediction, use of the energy-based model may be generally valid for ductile/brittle laminate composites. This apparent discrepancy between the various data probably results from the fact that the energy method does not take into account the extent of bridging ligaments, and hence fails to distinguish between laminate composites with varying bridging lengths. Additionally, an important parameter that affects Equation 18 is the thickness of the ductile reinforcements, t. The laminate composites tested by Bloyer *et al.* [15] were reinforced with ductile layers that ranged in thickness between 50-250 μm, whereas the laminates tested in the current work consisted of ductile layers with thickness ranging between 200-580 μm. It is suggested that the scaling of K_{SS} in Equation 18 with the ductile layer thickness

may not reflect the true toughness variation with thickness. The more rigorous weight function methods do not take into account the thickness of the Ti layers directly (in crack divider orientation), instead they incorporate it into the volume fraction parameter, f. Hence, Equation 18 must be carefully interpreted when used to estimate laminate composite toughness.
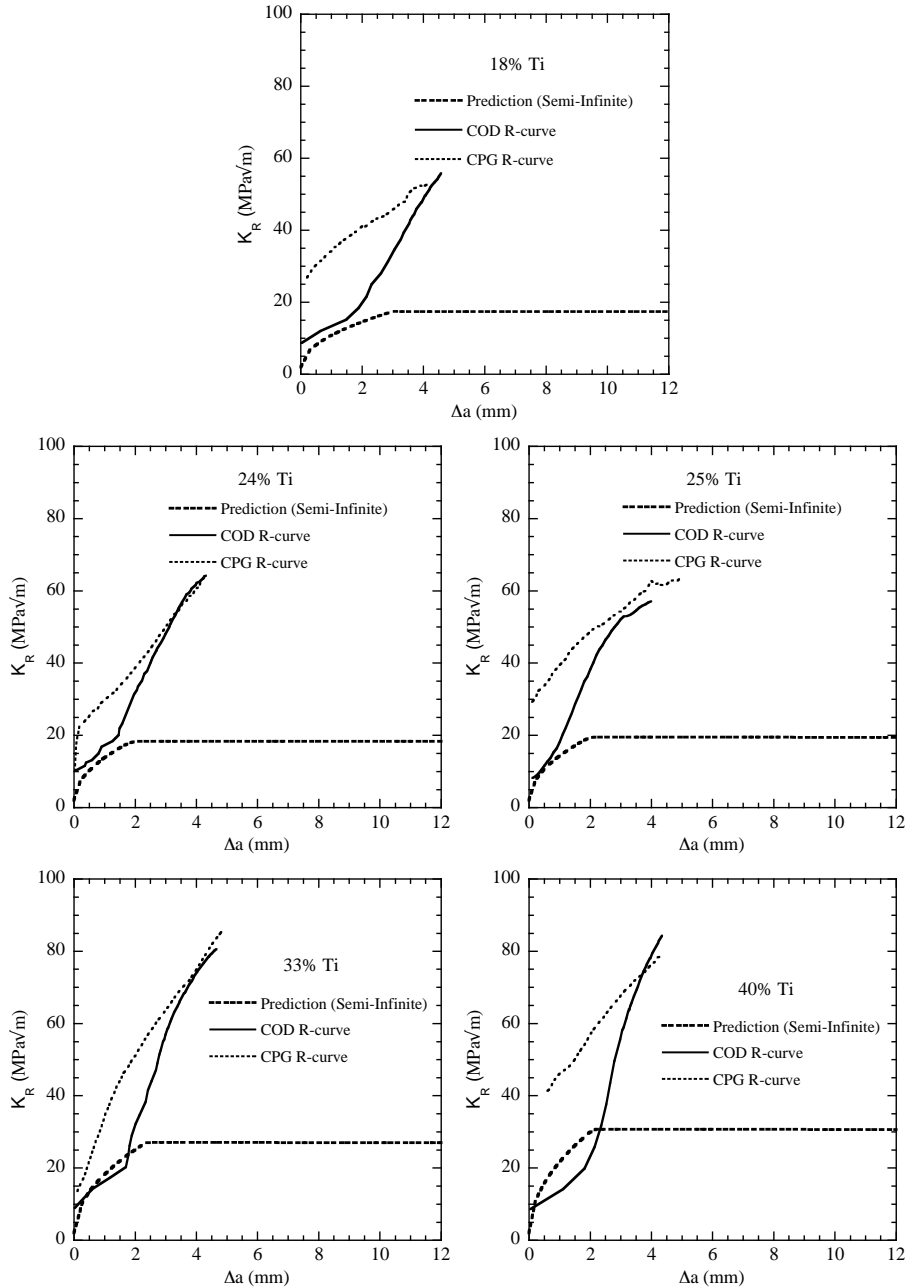
Figure 3-14.   Plots showing the R-curve predictions under SSB conditions. The Ti volume fraction varied between 18% - 40%, indicated on the plots. The bridging length and specimen width values used for the fit are given in Table 3-2.

E. Effect of layer thickness and volume fraction

One may expect that the toughness of laminate composites scales proportionally with increasing volume fraction and layer thickness of the ductile phase, since larger bridging zones may develop. Several models already developed for particles or fiber reinforcements confirm such a trend [85, 86, 93]. A review of the literature on ductile particulate or fiber reinforced composites support that initiation toughness (K_N) is similar to fracture toughness (K_{IC}) of the brittle matrix [48, 50, 89]. This may be due to the fact that in such composites, cracks are predominantly embedded inside the brittle matrix and only occasionally 'see' the ductile inclusions. However, fewer studies on the effect of layer thickness in laminate composites on fracture properties have been conducted. The only known complete studies were performed on Al(Cu, Ni)/Al$_2$O$_3$ [75] and Nb/Nb$_3$Al [14-17, 19].

Both the large scale bridging model and the energy model suggest that the toughness increases with increase in Ti volume fraction. Indeed, the resistance to crack propagation improved, in general, with an increase in volume fraction. The peak toughness calculated from the R-curves obtained from COD and CP gage measurements along with the toughness values estimated by the energy model from Equation 18 and SSB model from Equation 17 are plotted as a function of Ti layer volume fraction in Figure 3-18. All the calculations show that the peak toughness is achieved between 33-40% Ti reinforcement, among the tested samples. It should be noted that the layer thickness also changed between 200-580 μm. The laminates 24Ti and 25Ti that had nearly the same volume fraction, but different Ti layer thickness, exhibited slightly differing toughness values obtained from COD R-curve. However, the CP gage R-curve indicated very similar behavior.

It might be expected that the crack initiation toughness (K_N) in divider laminates will also be equal to the toughness of the brittle matrix, since the crack front is exposed to both the brittle and ductile layers. TiNb/γ-TiAl is one of the most studied and characterized ductile reinforced brittle system [4, 6, 7, 22]. At just 20% TiNb (f_m), calculated steady state toughness (K_{SS}) (in both orientations) indicated an increase of nearly 10 times (~46.7 MPa√m) that of the matrix after 4.2

cm of crack growth. Nevertheless, the initiation toughness was found to be comparable to the matrix toughness of 8 MPa√m. Work done on Al(Cu)/Al₂O₃ laminates (in DO), with $f_m < 30\%$ (volume fraction of metal), showed that the toughness of brittle Al_2O_3 can be enhanced from 3.5 MPa√m to nearly 20-45 MPa√m [74], while the crack initiation toughness (K_N) was always equal to the brittle phase fracture toughness of ~3.5 MPa√m [73]. Bloyer *et al.* [15] also observed that the initiation toughness of the composite was similar to the brittle phase toughness with layer thickness having little effect.
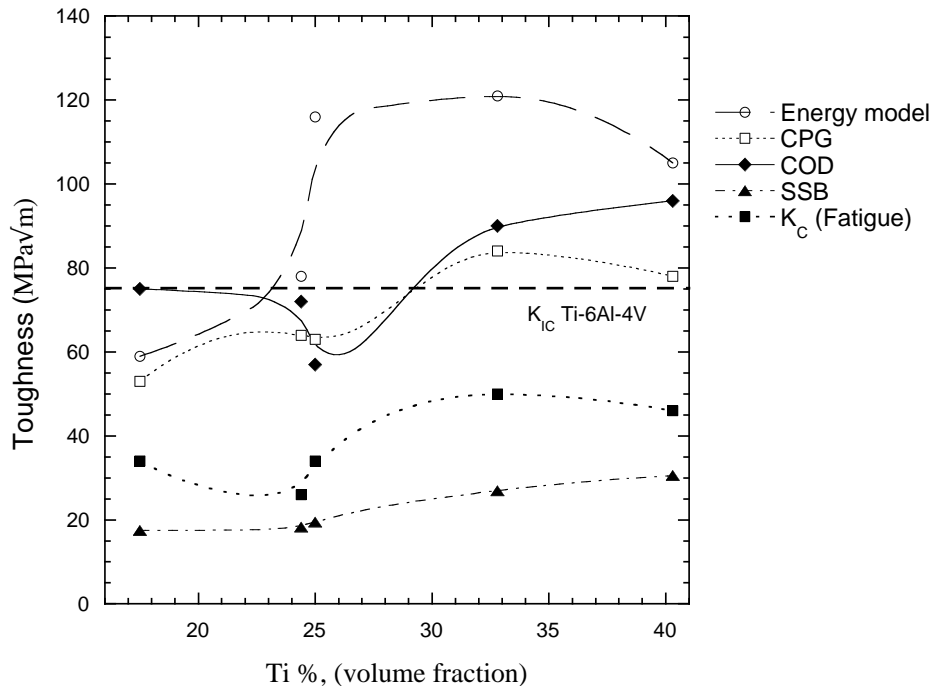
Figure 3-15. The toughness values calculated from Equation 17 and 18 compared with those obtained from experiments (K_{COD} and K_{CP}) as a function of ductile phase volume fraction.

Similarly, since the crack front is embedded in both the ductile and brittle layers, it was anticipated that the initiation toughness of the laminates would be close to the intermetallic toughness (~2 MPa√m). However, in the present work, the initiation toughness of 9 MPa√m (from COD R-curves) observed in the composites was nearly 5 times the intermetallic toughness. This may be due to any residual bridging ligaments formed during fatigue pre-cracking that existed prior to monotonic fracture tests. The fatigue crack growth experimental data, as shown in Figure 3-21 for the crack divider laminates, indicated similar fatigue thresholds, between 3.7 - 4.2 MPa√m among various samples tested [84]. Since, all the bend specimen used in fracture

toughness testing were fatigue pre-cracked just above threshold intensity level (~5 MPa√m, see Figure 3-18), it may be reasonable to expect the residual bridging conditions existing before the fracture tests to be very similar and hence may have led to comparable fracture initiation toughness.

F.   General Discussion

The main aim of the current work is to appraise the feasibility of MIL composites for structural applications, and hence determining and modeling their fracture behavior is a paramount task. The R-curves that have been experimentally measured were correlated with weight function methods by taking into account fairly simple crack bridging conditions. These methods have indicated that the laminate composites exhibited superior toughness properties, on par with monolithic conventional materials like aluminum and titanium alloys. It was seen, however, that the resulting R-curves were measured under LSB conditions, where the bridging lengths were comparable to the specimen dimensions (see Equation 7). Hence, by considering a semi-infinite specimen that reflected SSB conditions, the resistance curves that were calculated suggest that the true toughness values may be much lower than observed under LSB conditions. The key concept that was presented by Zok and Hom [90] and illustrated in the present work is that although the toughness values obtained under LSB conditions may reflect the fracture behavior of structures with similar dimensions as the specimens used in the current experiments, the true fracture properties of large structural components may be overestimated, and hence the small specimen properties cannot be used as an inherent material property.

This is demonstrated in Figure 3-18, where the R-curves under LSB conditions for several finite width specimens are compared with the R-curves under SSB conditions for large specimen. For a given bridging length, such comparisons may be calculated using Equations 12 and 17. These plots may be appropriately used to evaluate the range of possible toughness achievable in these laminates, with the true fracture behavior lying somewhere between these limits. When small specimens are used, such plots make it convenient to assess the true resistance curves.

Typically, the values b/a and b/(w-a) determine the extent of bridging conditions (see Equation 7). The general approach has been to evaluate these ratios for a bridging length observed during R-curve testing of small specimens and analyzing the observations after establishing the appropriate bridging conditions. However, the bridging length is not unique for a given specimen, since it depends on a number of geometrical parameters associated with the specimen size. Evidently, for a given volume (or size) of a laminate composite, the amount of cracking in the brittle intermetallic can be controlled by simply changing either the thickness or the volume fraction of the ductile phase and vice versa, and, therefore, the bridging zone size may be altered. For example, the R-curves in Figure 3-15 were obtained from specimens that were only notched but not fatigue pre-cracked. The peak toughness values observed in these R-curves exceeded the toughness values reported in Table 3-2 for the fatigue pre-cracked specimens. Moreover, at the end of the test, the samples were heat tinted at 600°C for a few minutes in order to oxidize the exposed crack plane in Ti and Al_3Ti layers. The subsequently fractured surfaces indicated that the bridging zone lengths were nearly 4-6 mm (compare these values with the bridging lengths of ~2-3 mm observed in fatigue pre-cracked samples). Clearly, LSB conditions were prevalent and to estimate SSB toughness values, specimens with widths ~100-150 mm would be required. Therefore, at the outset, it would appear necessary to report the toughness measurements alongside with the geometric properties for every test, and hence a general platform for evaluating and comparing laminate composite properties may appear to evade us.

However, the problem may have a solution if it is approached in a reverse fashion. Specifically, Is it possible to introduce sufficiently small bridging zone lengths in a small specimen such that SSB conditions may apply (i.e., satisfy Equation 7), and hence appraise the true toughness properties of the laminate composites? Figure 3-18 shows the optical micrographs of crack fronts in a laminate composite during cyclic fatigue testing. The extent of cracking in the brittle Al_3Ti is less severe than under R-curve testing, as shown in Figure 3-19. Moreover, the crack tunneling into the brittle phase ahead of the crack in Ti layer is limited, such that only ~0.6 mm bridging zones are formed. Such reduced bridging zone lengths under cyclic loading has also been observed for both ductile particulate reinforced brittle matrix composites and other brittle/ductile laminate composites [15, 17]. Therefore, such small bridging zones mimic SSB conditions for specimens tested in the present work (w ~20-25 mm). Yet, the cyclic fatigue crack

growth data in Figure 3-19 [84] indicate that the composite laminate sustained stress intensity factor range (ΔK) at failure (the upper region of the sigmoidal fatigue curve) between 25-45 MPa√m. In fact, considering the load ratio, R, as 0.1, the stress intensity at failure was ~26-50 MPa√m. These values are nearly 10-20 MPa√m greater than the values predicted under SSB conditions for R-curve testing. Therefore, it may appear that the SSB calculations may be underestimating the true toughness behavior.
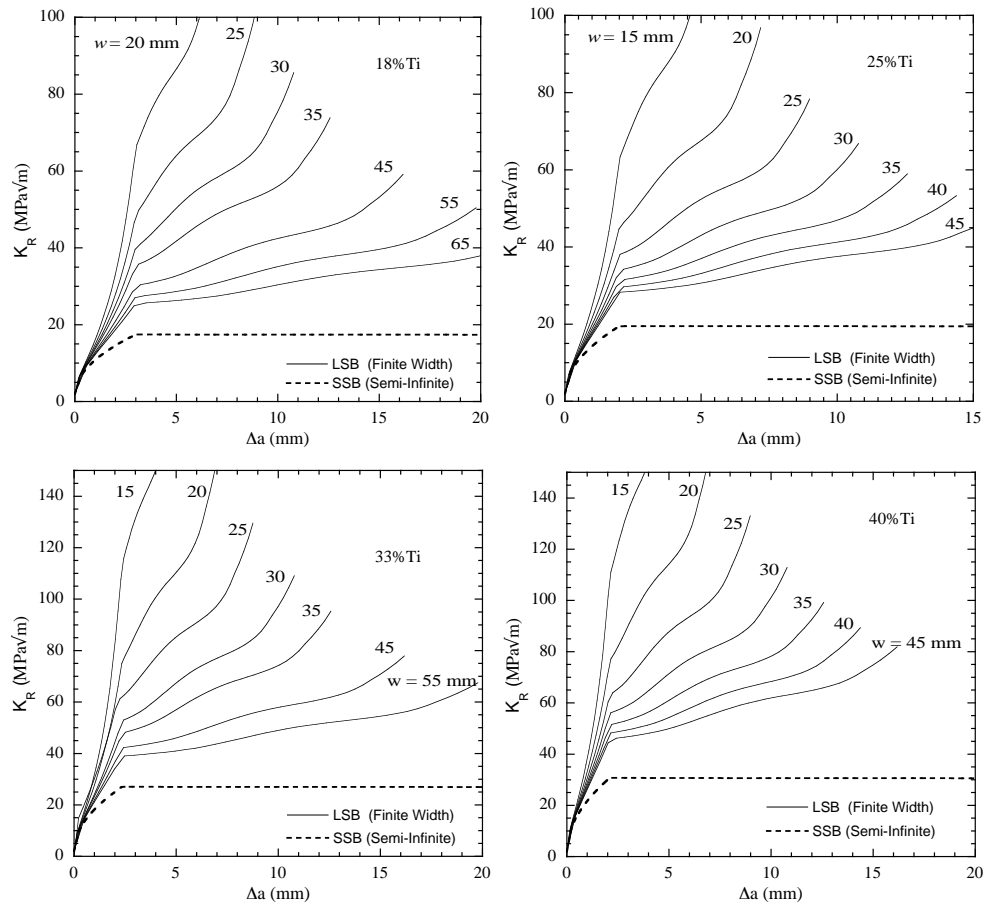
Figure 3-16.   Plots showing the effects of LSB on the R-curve behavior. The SSB R-curve is also drawn for comparison.
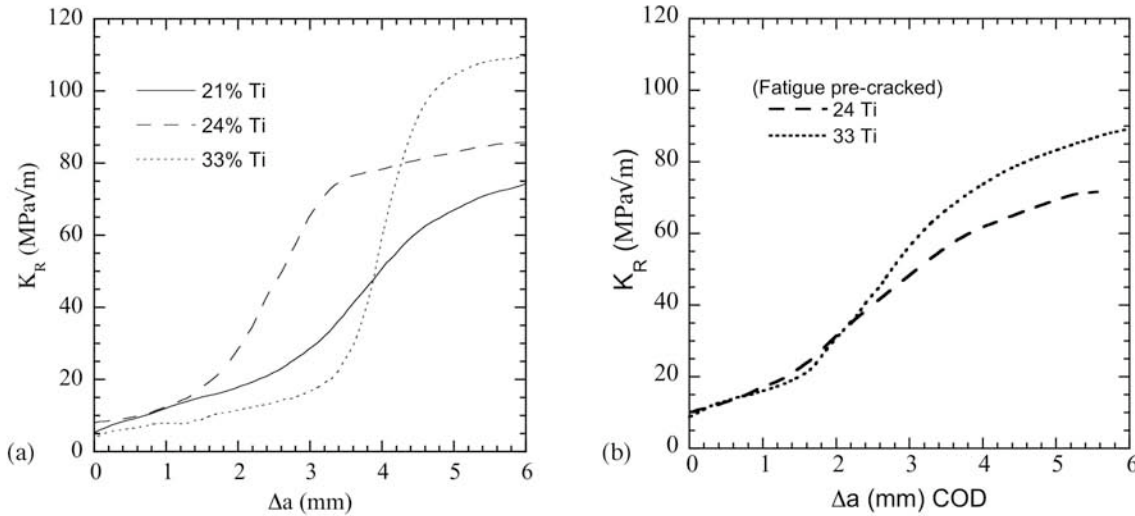
Figure 3-17. (a) R-curves measured for specimen that were not fatigue pre-cracked. Compare these with the R-curves measured from specimens that were fatigue pre-cracked prior to fracture testing (b).
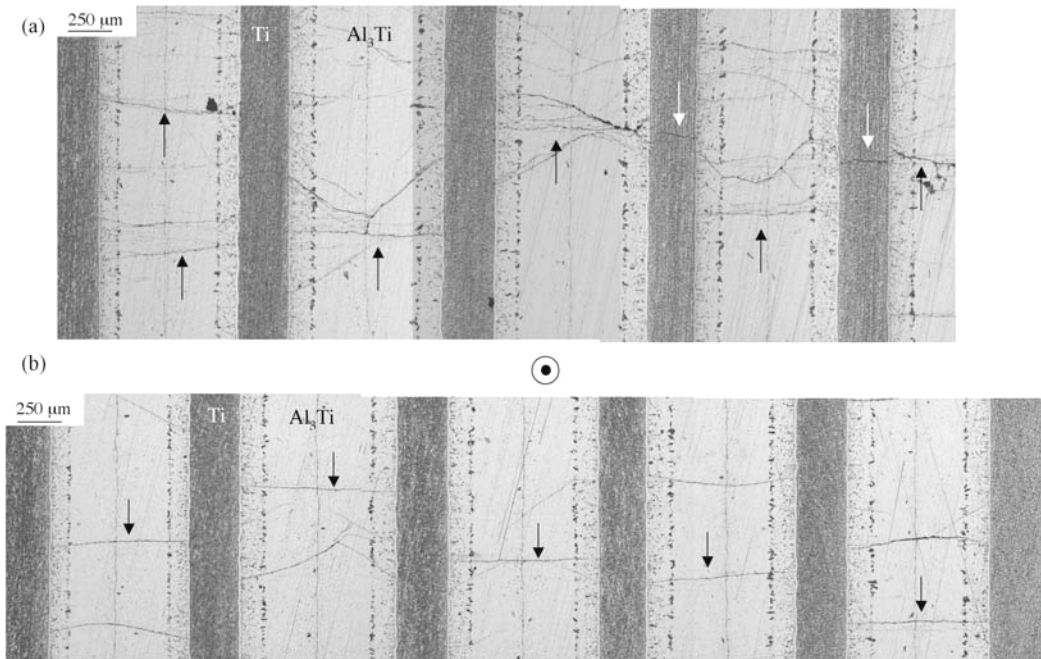
Figure 3-18. Optical micrographs of crack fronts in a laminate composite during cyclic fatigue testing (crack plane growth is horizontal and into the plane of the page). (a) The crack front at an approximate crack tip in Ti layer. (b) The crack front shown here is nearly 0.4 mm ahead of the crack tip in the Ti layer (measured by the CP gage), suggesting tunneling of the cracks into the brittle Al_3Ti layer (corresponding to the cross-section $AA^|$ in Figure 3-11) . The cross-section also indicates the existence of a few non-coplanar cracks. The cracks in Al_3Ti tunneled only ~0.6 mm ahead of the crack front in Ti layer during cyclic loading. The arrows indicate cracks that have tunneled through the brittle layer, only a few are identified.

101

This does not however reflect on the validity of the SSB model, but rather is due to the fact that the bridging zone size may not be unique for a given composite. Hence, the toughness behavior can be either overestimated or underestimated. The observations from the cyclic fatigue crack growth experiments, however, appear to lie between these upper and lower bounds. They may not be the true inherent toughness of the composite, yet they may represent closer, yet conservative, estimates of the true toughness values. Therefore, the experimental results support that the fatigue crack growth experiments are capable of measuring near-fracture toughness values of ductile-brittle laminate composites without underestimating or overestimating their true potential as tough materials. This may eventually lead to adoption of fatigue crack growth experiments as a means of evaluating the fracture behavior in ductile-brittle laminate composites.
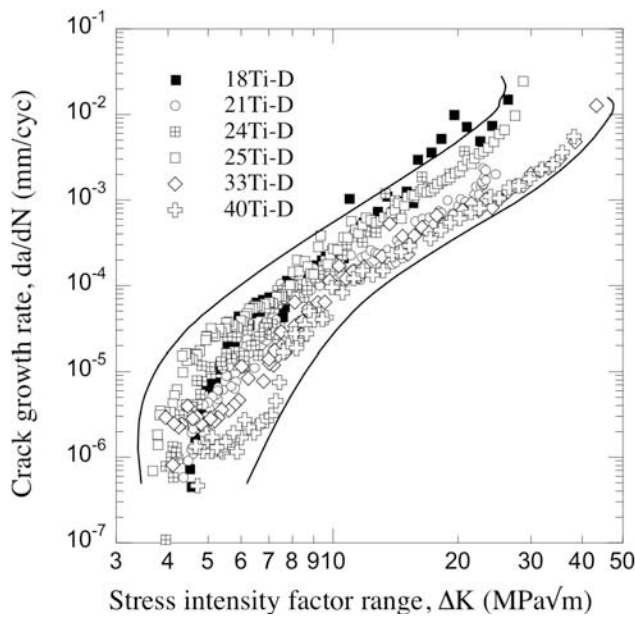
Figure 3-19. Fatigue crack growth rates in crack divider orientation MIL composites. Notice that the fatigue thresholds for the above composites lie between 3.8 – 4.7 MPa√m [84].

The added advantage is that the fatigue crack growth data is automatically obtained and hence the parameters needed for designing the material against cyclic loading conditions are readily available. Therefore, both the damage critical properties of fracture toughness and cyclic crack growth data are evaluated together. The toughness values from the fatigue crack growth data along with the data from other models and experiments listed in Table 3-2 are plotted in Figure

3-17 for comparison. It should be noted that this approach may be suitable only for laminate composites. It has been observed in ductile particulate reinforced brittle matrix composites that cyclic loading nearly eliminated the bridging ligaments that spanned the crack wake [4, 13, 46, 52], and hence the approach may not be feasible or applicable in such cases.

Finally, the specific fracture toughness ($\Delta K/\rho$) versus specific elastic modulus (E/ρ) of the MIL composites is compared with various other ceramics, composites and conventional structural alloys (like steel, aluminum etc.) in Figure 3-22 [26]. An ideal material in terms of high fracture toughness and elastic modulus with low density should occupy the top right corner in the plot. It can be seen that the MIL composites have higher specific toughness than other laminate systems and are on par with many structural alloys like magnesium, aluminum, steel and titanium. Thus, owing to the ease of fabrication, low fabrication costs, and their attractive mechanical properties, MIL (Ti/Al$_3$Ti) composites are promising candidates for structural applications that require optimization in weight.
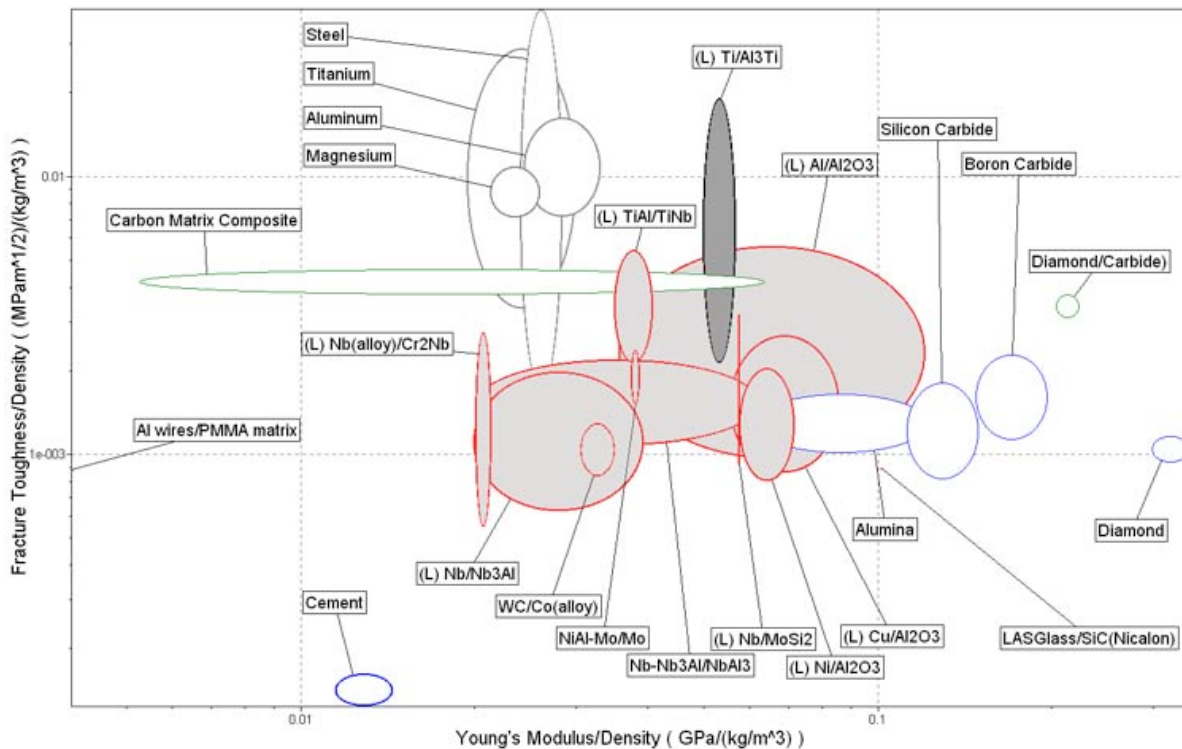
Figure 3-20. Specific Fracture Toughness versus Specific Modulus Property map for an array of structural materials. Plot includes MIL (Ti-Al$_3$Ti) composites (dark gray colored) and other laminate systems (identified by (L) and colored in light gray), metals, alloys and composites [26].

IV.   CONCLUSIONS

The above studies on the fracture toughness and R-curve behavior of novel metal-intermetallic laminate composites lead to the following conclusions:

1.   Ti-Al$_3$Ti MIL composites exhibited almost an order of magnitude improvement in toughness values over monolithic Al$_3$Ti (fracture toughness ~ 2 MPa$\sqrt{}$m) with the addition of just 20-40% by volume of ductile Ti phase in the form of continuous layers. Furthermore, the fracture resistance increased with increasing Ti volume fraction.

2.   Significant improvement in toughness was attributed primarily to uncracked ductile Ti layers that bridge the crack wake and shield the crack tip from far field loading.

3.   The crack-initiation toughness, K_N, was nearly 5 times (~9 MPa$\sqrt{}$m) the intermetallic fracture toughness. However, due to the formation of the bridging ligaments during fatigue pre-cracking, prior to the R-curve testing, a systematic analysis on the variation or dependence of K_N on Ti layer thickness or volume fraction was not available.

4.   A weight function model was used to evaluate the contribution of bridging towards such improvement in toughness values. A fit between the model and the experimental R-curve data showed that bridging lengths varied between 2-3 mm, closely matching the observed bridging zone lengths. Clearly, such large bridging zones indicate large scale bridging (LSB) conditions.

5.   Steady state toughness values were evaluated using models that reflected SSB conditions. The calculations yielded toughness values nearly one-third of those obtained under LSB conditions. It is suggested that since bridging lengths may not be unique for a composite of given ductile layer thickness and volume fraction, and may depend on specimen geometry, the SSB models may undervalue the toughness improvements achievable in the MIL composites.

6.   Under fatigue crack growth testing, the bridging lengths were reduced to ~0.5 mm. Yet, the toughness values at failure were nearly 10-20 MPa$\sqrt{}$m greater than the values

predicted under SSB conditions for R-curve testing. Therefore, it is suggested that the stress intensity at failure during an increasing ΔK fatigue crack growth experiment may better predict the true toughness behavior achievable in these laminate composites.

7 A comparison of the specific toughness versus specific elastic modulus data for MIL composites with a host of materials that include conventional structural metals/alloys, brittle/ductile composites and high strength ceramics suggest that the MIL composites may be promising candidates for structural applications that require optimization in weight.

Appendix A

The compliance change may be used to calculate the crack length using the following equation:

$$\frac{a}{w} = C_0 + C_1 U + C_2 U^2 + C_3 U^3 + C_4 U^4 + C_5 U^5 \tag{A-1}$$

where U is given by:

$$U = \frac{1}{\sqrt{\dfrac{EvB(4w)}{PS}} + 1} \tag{A-2}$$

and C_i are compliance coefficients for bend specimen and equal to:

Table 3-3.   Compliance coefficients for Equation (A-1)

C_i	$i = 0$	1	2	3	4	5
	0.999748	-3.9504	2.9821	-3.21408	51.51564	-113.031

E is the elastic modulus, v is the displacement between measurement points, B is the effective specimen thickness, P is the load between measurement points, a is the crack length, w is the specimen width, and S is the span between the loading points. Fracture toughness or R-curve behavior is then calculated by using:

$$K = \frac{PS}{BW^{\frac{3}{2}}} f\left(\frac{a}{w}\right) \tag{A-3}$$

where $f(a/w)$ is given by the function:

$$f\left(\frac{a}{w}\right) = \frac{3\left(\frac{a}{w}\right)^{\frac{1}{2}}\left[1.99 - \left(\frac{a}{w}\right)\left[1 - \left(\frac{a}{w}\right)\right]\left[2.15 - 3.93\left(\frac{a}{w}\right) + 2.7\left(\frac{a}{w}\right)^2\right]\right]}{2\left[1 + 2\left(\frac{a}{w}\right)\right]\left[1 - \left(\frac{a}{w}\right)\right]^{\frac{3}{2}}} \qquad (A-4)$$

Appendix B

Table 3-4. $\xi_n(\alpha)$ for a single edge-cracked in a finite width specimen [92]

α	$\xi_1(\alpha)$	$\xi_2(\alpha)$	$\xi_3(\alpha)$	$\xi_4(\alpha)$	$\xi_5(\alpha)$
0.01	2	0.9765	1.142	-0.3504	-0.0912
0.05	2	1.0927	1.1506	-0.3662	-0.0819
0.1	2	1.4187	1.1378	-0.355	-0.0763
0.2	2	2.5366	1.2378	-0.3474	-0.0562
0.3	2	4.2381	1.6796	-0.4095	-0.0188
0.4	2	6.6359	2.8048	-0.6105	0.0394
0.5	2	10.022	5.4999	-1.3401	0.2178
0.6	2	15.036	11.878	-3.6067	0.7858
0.7	2	29.519	45.507	-18.928	4.8834
0.8	2	38.813	78.752	-36.596	9.8172
0.85	2	53.846	151.21	-79.015	22.27
0.9	2	82.687	351	-207.09	60.859
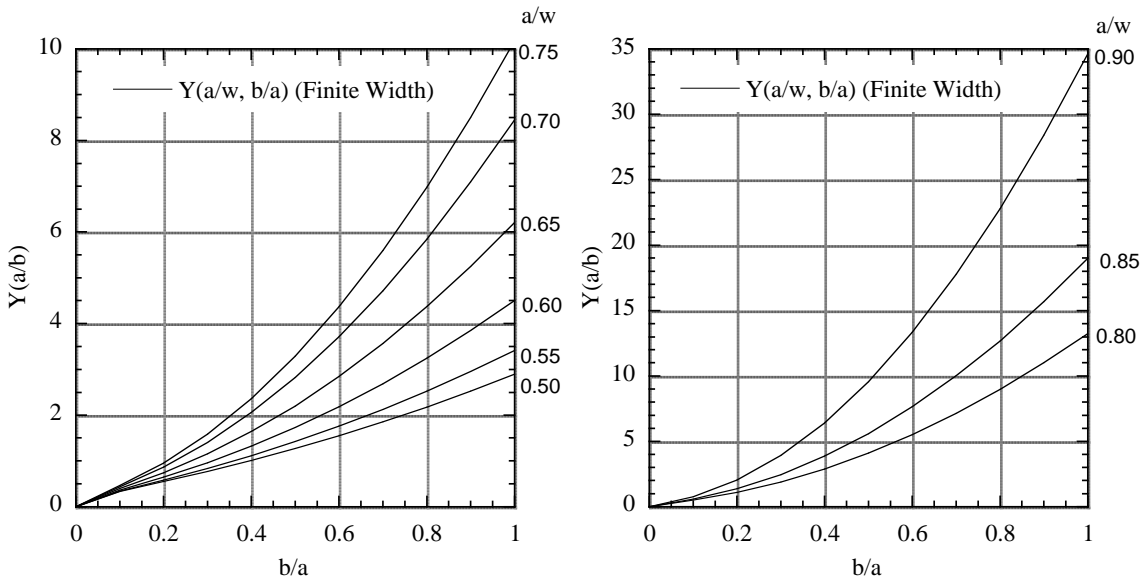
Figure 3-21.   The non-dimensional factor Y$(a/w, b/a)$ (see Equation 11) for single edge crack in a finite width specimen, with uniform tractions in the wake of crack tip. For better clarity, Equation 11 is plotted above in two figures for different a/w ratios.

Appendix C

Table 3-5. $\zeta_n(\alpha)$ for a single edge-cracked in a semi-infinite specimen [92].

	n = 1	2	3	4	5
ζ_n	2.0	0.9788	1.1101	-0.3194	-0.1017
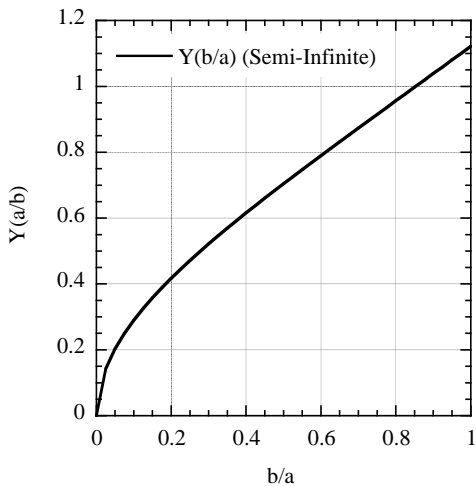
Figure 3-22.   The non-dimensional factor Y*(b/a)* (see Equation 16) for single edge crack in a semi-infinite specimen, with uniform tractions in the wake of the crack tip.

REFERENCES TO SECTION 3

1.   Sauthoff, G., *Intermetallics*. Materials Science and Technology: A comprehensive treatment, ed. P.H. Robert W. Cahn, and Edward J. Kramer. Vol. Volume 8. 1995: VCH.

2.   Darolia, R., J.J. Lewandowski, C.T. Liu, P.L. Martin, D.B. Miracle and M.V. Nathal, *Structural intermetallics*. Struct. Intermet., Proc. Int. Symp., 1st. 1993: TMS. 1-15.

3.   Rao, K.T.V., G.R. Odette and R.O. Ritchie, *Fatigue and fracture resistance of ductile-phase toughened intermetallic-matrix composites: behavior in β-titanium-niobium γ-titanium-aluminum (β–TiNb/γ-TiAl)*. Fatigue Adv. Mater., Proc. Eng. Found. Int. Conf., 1991: p. 429-36.

4.   Rao, K.T.V., G.R. Odette and R.O. Ritchie, *On the contrasting role of ductile-phase reinforcements in the fracture toughness and fatigue-crack propagation behavior of titanium niobium (TiNb)/titanium aluminide (γ-TiAl)*. Acta Metallurgica et Materialia, 1992. **40**(2): p. 353-61.

5. Rao, K.T.V., G.R. Odette and R.O. Ritchie, *The role of interface and reinforcement properties on the fracture and fatigue resistance of ductile-phase toughened γ-TiAl composites.* Struct. Intermet., Proc. Int. Symp., 1st, 1993: p. 829-35.

6. Rao, K.T.V., G.R. Odette and R.O. Ritchie, *Ductile-reinforcement toughening in γ-TiAl intermetallic-matrix composites: effects on fracture toughness and fatigue-crack propagation resistance.* Acta Metallurgica et Materialia, 1994. **42**(3): p. 893-911.

7. Rao, K.T.V. and R.O. Ritchie, *Microstructural effects on fatigue-crack growth behavior in γ-TiAl/β-TiNb intermetallic composites.* Materials Research Society Symposium Proceedings, 1992. **273**(Intermetallic Matrix Composites II): p. 127-33.

8. Rao, K.T.V. and R.O. Ritchie, *Fatigue crack propagation resistance of ductile titanium-niobium-reinforced γ-titanium-aluminum intermetallic matrix composites.* Materials Science & Engineering, A: Structural Materials: Properties, Microstructure and Processing, 1992. **A153**(1-2): p. 479-85.

9. Rao, K.T.V. and R.O. Ritchie, *Fracture and fatigue considerations in the development of ductile-phase reinforced intermetallic-matrix composites.* Fatigue Fract. Ordered Intermet. Mater. I, Proc. Symp., 1994: p. 3-12.

10. Rao, K.T.V. and R.O. Ritchie, *Microstructural effects on fatigue-crack growth behavior in γ-TiAl/β-TiNb Intermetallic composites.* Materials Research Society Symposium Proceedings, 1992. **273**: p. 127-133.

11. Rao, K.T.V., W.O. Soboyejo and R.O. Ritchie, *Ductile-phase toughening and fatigue-crack growth in niobium-reinforced molybdenum disilicide intermetallic composites.* Metallurgical Transactions A: Physical Metallurgy and Materials Science, 1992. **23A**(8): p. 2249-57.

12. Soboyejo, W.O., F. Ye, L.C. Chen, N. Bahtishi, D.S. Schwartz and R.J. Lederich, *Effects of reinforcement architecture on the fatigue and fracture behavior of MoSi2/Nb composites.* Fatigue and Fracture of Ordered Intermetallic Materials II, Proceedings of a Symposium, Rosemont, Ill., Oct. 6-10, 1994, 1995: p. 359-90.

13. Soboyejo, W.O., F. Ye and T.S. Srivatsan, *An investigation of the effect of ductile phase reinforcement on the fatigue and fracture behavior of a gamma-titanium aluminide intermetallic.* Fatigue and Fracture of Ordered Intermetallic Materials II, Proceedings of a Symposium, Rosemont, Ill., Oct. 6-10, 1994, 1995: p. 391-415.

14. Bloyer, D.R., K.T.V. Rao and R.O. Ritchie, *Resistance-curve toughening in ductile-phase reinforced intermetallic laminates.* Johannes Weertman Symposium, Proceedings of a Symposium held during the TMS Annual Meeting, Anaheim, Calif., Feb. 4-8, 1996, 1996: p. 261-266.

15. Bloyer, D.R., K.T. Venkateswara Rao and R.O. Ritchie, *Fracture toughness and R-curve behavior of laminated brittle-matrix composites.* Metallurgical and Materials Transactions A: Physical Metallurgy and Materials Science, 1998. **29A**(10): p. 2483-2496.

16. Bloyer, D.R., K.T. Venkateswara Rao and R.O. Ritchie, *Laminated Nb/Nb₃Al composites: effect of layer thickness on fatigue and fracture behavior.* Materials Science & Engineering, A: Structural Materials: Properties, Microstructure and Processing, 1997. **A239-240**: p. 393-398.

17. Bloyer, D.R., V. Rao and R.O. Ritchie, *Resistance-curve toughening in ductile/brittle layered structures: behavior in Nb/Nb₃Al laminates.* Materials Science & Engineering, A: Structural Materials: Properties, Microstructure and Processing, 1996. **A216**(1-2): p. 80-90.

18. Bloyer, D.R., K.T.V. Rao and R.O. Ritchie, *Fatigue-crack propagation behavior of ductile/brittle laminated composites.* Metallurgical and Materials Transactions A: Physical Metallurgy and Materials Science, 1999. **30A**(3): p. 633-642.

19. Bloyer, D.R., K.T.V. Rao and R.O. Ritchie, *Toughness and subcritical crack growth in Nb/Nb₃Al layered materials.* Materials Research Society Symposium Proceedings, 1996. **434**(Layered Materials for Structural Applications): p. 243-248.

20. Badrinarayanan, K., A.L. McKelvey, K.T. Venkateswara Rao and R.O. Ritchie, *Fracture and fatigue-crack growth behavior in ductile-phase toughened molybdenum disilicide: effects of niobium wire vs. particulate reinforcements.* Metallurgical and Materials Transactions A: Physical Metallurgy and Materials Science, 1996. **27A**(12): p. 3781-3792.

21. Bencher, C.D., A. Sakaida, K.T.V. Rao and R.O. Ritchie, *Toughening mechanisms in ductile niobium-reinforced niobium aluminide (Nb/Nb₃Al) in situ composites.* Metallurgical and Materials Transactions A: Physical Metallurgy and Materials Science, 1995. **26A**(8): p. 2027-33.

22. Odette, G.R., B.L. Chao, J.W. Sheckherd and G.E. Lucas, *Ductile phase toughening mechanisms in titanium aluminide (TiAl)-titanium-niobium laminate composite.* Acta Metallurgica et Materialia, 1992. **40**(9): p. 2381-9.

23. Heathcote, J., G.R. Odette, G.E. Lucas, R.G. Rowe and D.W. Skelly, *On the micromechanics oflow temperature strength and toughness of intermetalic/metallic microlaminate comosites.* Acta mater., 1996. **44**(11): p. 4289-4299.

24. Heathcote, J., G.R. Odette, G.E. Lucas and R.G. Rowe, *Mechanical properties of metal-intermetallic microlaminate composites.* Materials Research Society Symposium Proceedings, 1996. **434**(Layered Materials for Structural Applications): p. 101-112.

25. Heathcote, J., G.R. Odette and G.E. Lucas, *A finite element study on constrained deformation in an intermetallic/metallic microlaminate composite.* Materials Research Society Symposium Proceedings, 1996. **434**(Layered Materials for Structural Applications): p. 183-188.

26. Rohatgi, A., D.J. Harach, K.S. Vecchio and K.P. Harvey, *Resistance-curve and fracture behavior of Ti-Al₃Ti metallic-intermetallic laminate (MIL) composites.* Acta Mat., 2003. **51**: p. 2933-2957.

27. Menig, R., M.H. Meyers, M.A. Meyers and K.S. Vecchio, *Quasi-static and dynamic mechanical response of Strombus gigas (conch) shells.* Mater. Sci. & Eng., 2001. **A297**: p. 203-211.

28. Menig, R., M.H. Meyers, M.A. Meyers and K.S. Vecchio, *Quasi-static and Dynamic mechanical response of Haliotis Rufescens (Abalone Shells).* Acta Materialia, 2000. **48**: p. 2383-2398.

29. Anton, D.L. and D.M. Shah, *Ductile phase toughening of brittle intermetallics.* Materials Research Society Symposium Proceedings, 1990. **194**(Intermet. Matrix Compos.): p. 45-58.

30. Harach, D.J. and K.S. Vecchio, *Microstructure evolution in metal-intermetallic laminate (MIL) composites synthesized by reactive foil sintering in air.* Metallurgical and Materials Transactions A: Physical Metallurgy and Materials Science, 2001. **32A**(6): p. 1493-1505.

31. Alman, D.E., J.C. Rawers and J.A. Hawk, *Microstructural and failure characteristics of metal-intermetallic layered sheet composites.* Metallurgical and Materials Transactions A: Physical Metallurgy and Materials Science, 1995. **26A**(3): p. 589-99.

32. Xia, Z., J. Liu, S. Zhu and Y. Zhao, *Fabrication of laminated metal-intermetallic composites by interlayer in-situ reaction.* Journal of Materials Science, 1999. **34**(15): p. 3731-3735.

33. Alman, D.E., C.P. Dogan, J.A. Hawk and J.C. Rawers, *Processing, structure and properties of metal-intermetallic layered composites.* Materials Science & Engineering, A: Structural Materials: Properties, Microstructure and Processing, 1995. **A192/193**: p. 624-32.

34. Maupin, H.E. and J.C. Rawers, *Metal-intermetallic composites formed by reaction-sintering elemental powders.* Journal of Materials Science Letters, 1993. **12**(8): p. 540-1.

35. Rawers, J.C., D.E. Alman and J.A. Hawk, *Overview: layered metal/intermetallic composites formed by SHS reactions.* International Journal of Self-Propagating High-Temperature Synthesis, 1993. **2**(1): p. 12-24.

36. Rawers, J.C. and H.E. Maupin, *Metal-intermetallic composites formed by reaction-sintering metal foils.* Journal of Materials Science Letters, 1993. **12**(9): p. 637-9.

37. Alman, D.E., *Fabrication, structure and properties of aluminum-aluminide layered composites.* Materials Research Society Symposium Proceedings, 1996. **434**(Layered Materials for Structural Applications): p. 255-260.

38. Alman, D.E. and C.P. Dogan, *Intermetallic sheets synthesized from elemental Ti, Al, and Nb foils.* Metallurgical and Materials Transactions A: Physical Metallurgy and Materials Science, 1995. **26A**(10): p. 2759-62.

39. Dong Seok Chung, Y.T., Manabu Enoki and Teruo Kishi, *Formation behavior of aluminide layers during the fabrication of Nb/Nb-aluminide laminate materials from Nb and Al foil.* J. Japan Inst. Metals, 1999. **63**(8): p. 1043-1052.

40. Chung, D.-S., M. Enoki and T. Kishi, *Microstructural analysis and mechanical properties of in situ Nb/Nb-aluminide layered materials.* Science and Technology of Advanced Materials, 2002. **3**(2): p. 129-135.

41. Lesuer, D.R., C.K. Syn, O.D. Sherby, J. Wadsworth, J.J. Lewandowski and W.H. Hunt, Jr., *Mechanical behavior of laminated metal composites.* International Materials Reviews, 1996. **41**(5): p. 169-197.

42. Evans, A.G., *Perspective on the development of high-toughness ceramics.* Journal of the American Ceramic Society, 1990. **73**(2): p. 187-206.

43. Ritchie, R.O., *Mechanisms of fatigue-crack propagation in ductile and brittle solids.* International Journal of Fracture, 2000. **100**(1): p. 55-83.

44. Ritchie, R.O., *Mechanisms of fatigue crack propagation in metals, ceramics and composites: role of crack tip shielding.* Materials Science & Engineering, A: Structural Materials: Properties, Microstructure and Processing, 1988. **A103**(1): p. 15-28.

45. Heuer, A.H., *Transformation toughening in ZrO_2-containing ceramics.* J. Am. Ceram. Soc., 1987. **70**(10): p. 689-698.

46. Murugesh, L., K.T.V. Rao, L.C. DeJonghe and R.O. Ritchie, *Fracture and fatigue behavior in niobium aluminide (Nb_3Al) + niobium intermetallic composites.* Materials Research Society Symposium Proceedings, 1992. **273**(Intermetallic Matrix Composites II): p. 433-8.

47. Brooks, D., R.J. Lederich and W.O. Soboyejo, *An investigation of ductile and brittle reinforcement on the fracture behavior of molybdenum disilicide composites.* Fatigue Fract. Ordered Intermet. Mater. I, Proc. Symp., 1994: p. 55-74.

48. Flinn, B.D., C.S. Lo, F.W. Zok and A.G. Evans, *Fracture resistance characteristics of a metal-toughened ceramic.* Journal of the American Ceramic Society, 1993. **76**(2): p. 369-75.

49. Sigl, L.S., P.A. Mataga, B.J. Dalgleish, R.M. McMeeking and A.G. Evans, *On the toughness of brittle materials reinforced with a ductile phase.* Acta Metallurgica, 1988. **36**(4): p. 945-53.

50. Krstic, V.V. and P.S. Nicholson, *Toughening of glasses by metallic particles.* Journal of the American Ceramic Society, 1981. **64**(9): p. 499-504.

51. Soboyejo, W.O., F. Ye, L.C. Chen, N. Bahtishi, D.S. Schwartz and R.J. Lederich, *Effects of reinforcement morphology on the fatigue and fracture behavior of $MoSi_2$/Nb composites.* Acta Materialia, 1996. **44**(5): p. 2027-41.

52. Murugesh, L., K.T.V. Rao and R.O. Ritchie, *Crack growth in a ductile-phase-toughened niobium/niobium aluminide(Nb_3Al) in situ intermetallic composite under monotonic and cyclic loading.* Scripta Metallurgica et Materialia, 1993. **29**(8): p. 1107-12.

53. Mataga, P.A., *Deformation of crack-bridging ductile reinforcements in toughened brittle materials.* Acta Metallurgica, 1989. **37**(12): p. 3349-59.

54. Flinn, B.D., M. Ruhle and A.G. Evans, *Toughening in composites of alumina reinforced with aluminum.* Acta Metallurgica, 1989. **37**(11): p. 3001-6.

55. Zok, F., O. Sbaizero, C.L. Hom and A.G. Evans, *Mode I fracture resistance of a laminated fiber-reinforced ceramic.* J. Am. Ceram. Soc., 1991. **74**(1): p. 187-193.

56. J.D. Embury, F.Z., D.J. Lahaie and W. Poole. *The properties of interfaces in composites*. in *Intrinsic and extrinsic fracture mechanisms in Inorganic composite systems*. 1995: MRS.

57. Deve, H.E. and M.J. Maloney, *On the toughening of intermetallics with ductile fibers: role of interfaces.* Acta Metallurgica et Materialia, 1991. **39**(10): p. 2275-84.

58. Cao, H.C., B.J. Dalgleish, H.E. Deve, C. Elliott, A.G. Evans, R. Mehrabian and G.R. Odette, *A test procedure for characterizing the toughening of brittle intermetallics by ductile reinforcements.* Acta Metallurgica, 1989. **37**(11): p. 2969-77.

59. Rawers, J. and K. Perry, *Crack initiation in laminated metal-intermetallic composites.* Journal of Materials Science, 1996. **31**(13): p. 3501-3506.

60. Enoki, M., A. Ohta, D.S. Chung, M. Watanabe and T. Kishi, *Crack propagation behavior of Ti/Ti-Al layered materials.* Nippon Kinzoku Gakkaishi, 2000. **64**(11): p. 1076-1081.

61. Rawers, J.C. and D.E. Alman, *Fracture characteristics of metal/intermetallic laminate composites produced by reaction sintering and hot pressing.* Composites Science and Technology, 1995. **54**(4): p. 379-84.

62. Manabu Enoki, K.S., Byung-Nam Kim and Teruo Kishi, *Crack Propagation of Ni/NiAl Laminate Materials.* J. Japan Inst. Metals, 1999. **63**(7): p. 838-843.

63. Rowe, R.G., D.W. Skelly, M.R. Jackson, M. Larsen and D. Lachapelle, *Advanced aircraft engine microlaminated intermetallic composite turbine technology.* Materials Research Society Symposium Proceedings, 1996. **434**(Layered Materials for Structural Applications): p. 3-13.

64. Kajuch, J., J. Short and J.J. Lewandowski, *Deformation and fracture behavior of Nb in Nb_5Si_3/Nb laminates and its effect on laminate toughness.* Acta Metallurgica et Materialia, 1995. **43**(5): p. 1955-67.

65. Rigney, J.D., *Fracture of laminated and in situ niobium silicide-niobium composites.* Materials Research Society Symposium Proceedings, 1996. **434**(Layered Materials for Structural Applications): p. 227-241.

66. Bannister, M. and M.F. Ashby, *The deformation and fracture of constrained metal sheets.* Acta Metallurgica et Materialia, 1991. **39**(11): p. 2575-82.

67. Pickard, S.M. and A.K. Ghosh, *Bridge toughening enhancement in double-notched MoSi2/Nb model composites.* Metallurgical and Materials Transactions A: Physical Metallurgy and Materials Science, 1996. **27A**(4): p. 909-21.

68. Xiao, L. and R. Abbaschian, *On the flow behavior of constrained ductile phases.* Metallurgical Transactions A: Physical Metallurgy and Materials Science, 1993. **24A**(2): p. 403-15.

69. McNaney, J.M., R.M. Cannon and R.O. Ritchie, *Fracture and fatigue-crack growth along aluminum-alumina interfaces.* Acta mater., 1996. **44**(12): p. 4713-4728.

70. Huang, Y. and H.W. Zhang, *The role of metal plasticity and interfacial strength in the cracking of metal/ceramic laminates.* Acta Metallurgica et Materialia, 1995. **43**(4): p. 1523-30.

71. Dalgleish, B.J., K.P. Trumble and A.G. Evans, *The strength and fracture of alumina bonded with aluminum alloys.* Acta Metallurgica, 1989. **37**(7): p. 1923-31.

72. He, M.Y., F.E. Heredia, D.J. Wissuchek, M.C. Shaw and A.G. Evans, *The Mechanics of crack growth in layered materials.* Acta metall. mater., 1993. **41**(4): p. 1223-1228.

73. Shaw, M.C., D.B. Marshall, M.S. Dadkhah and A.G. Evans, *Cracking and damage mechanisms in ceramic/metal multilayers.* Acta metall. mater., 1993. **41**(11): p. 3311-3322.

74. Cao, H.C. and A.G. Evans, *On crack extension in ductile/brittle laminates.* Acta metall. mater., 1991. **39**(12): p. 2997-3005.

75. Hwu, K.L. and B. Derby, *Fracture of metal/ceramic laminates-II. Crack growth resistance and toughness.* Acta Materialia, 1999. **47**(2): p. 545-563.

76. Hwu, K.L. and B. Derby, *Fracture of metal/ceramic laminates-I. Transition from single to multiple cracking.* Acta Materialia, 1999. **47**(2): p. 529-543.

77. Dalgleish, B.J., M.C. Lu and A.G. Evans, *The strength of ceramics bonded with metals.* Acta Metallurgica, 1988. **36**(8): p. 2029-35.

78. Lesuer, D.R., J. Wadsworth, R.A. Riddle, C.K. Syn, J.J. Lewandowski and W.H. Hunt, Jr., *Toughening mechanisms in Al/Al-SiC laminated metal composites.* Materials Research Society Symposium Proceedings, 1996. **434**(Layered Materials for Structural Applications): p. 205-211.

79. Fox, M.R. and A.K. Ghosh, *Structure, strength and fracture resistance of interfaces in NiAl/Mo model laminates.* Mater. Sci. & Eng., 1999. **A259**: p. 261-268.

80. Ma, Q., M.C. Shaw, M.Y. He, B.J. Dalgleish, D.R. Clarke and A.G. Evans, *Stress redistribution in ceramic/metal multilayers containing cracks.* Acta metall. mater., 1995. **43**(6): p. 2137-2142.

81. Westbrook, J.H. *Structural intermetallics: their origins, status and future*. in *Struct. Intermet., Proc. Int. Symp., 1st*. 1993: TMS.

82. Anton, D.L. and D.M. Shah, *High temperature ordered compounds for advanced aero-propulsion applications.* Materials Research Society Symposium Proceedings, 1989. **133**(High-Temp. Ordered Intermet. Alloys 3): p. 361-71.

83. Larsen, J.M., W.C. Revelos and M.L. Gambone, *An overview of potential titanium aluminide composites in aerospace applications.* Materials Research Society Symposium Proceedings, 1992. **273**(Intermetallic Matrix Composites II): p. 3-16.

84. Adharapurapu, R.R., K.S. Vecchio, F. Jiang and A. Rohatgi, *Effects of ductile laminate thickness, volume fraction and orientation on fatigue-crack propagation in Ti-Al$_3$Ti metal-intermetallic laminate (MIL) composites.* Submitted to Metallurgical and Materials Transactions A, 2004.

85. Cox, B.N., *Extrinsic factors in the mechanics of bridged cracks.* Acta metall. mater., 1991. **39**(6): p. 1189-1201.

86. Cox, B.N. and D.B. Marshall, *Concepts for bridged cracks in fracture and fatigue.* Acta metall. mater., 1994. **42**(2): p. 341-363.

87. Erdogan, F. and P.F. Joseph, *Toughening of ceramics through crack bridging by ductile particles.* Journal of the American Ceramic Society, 1989. **72**(2): p. 262-70.

88. Ashby, M.F., F.J. Blunt and M. Bannister, *Flow characteristics of highly constrained metal wires.* Acta Metallurgica, 1989. **37**(7): p. 1847-57.

89. Bannister, M., H. Shercliff, G. Bao, F. Zok and M.F. Ashby, *Toughening in brittle systems by ductile bridging ligaments.* Acta Metallurgica et Materialia, 1992. **40**(7): p. 1531-7.

90. Zok, F. and C.L. Hom, *Large-scale bridging in brittle matrix composites.* Acta Metallurgica et Materialia, 1990. **38**(10): p. 1895-904.

91. Harvey, K.P., K. S. Vecchio, Unpublished work, 2003.

92. Wu, X.-R. and A.J. Carlsson, *Weight Functions and Stess Intensity Factor Solutions*. First Edition ed. 1991: Pergamon Press.

93. Evans, A.G. and R.M. McMeeking, *On the toughening of ceramics by strong reinforcements.* Acta metall., 1986. **34**(12): p. 2435-2441.

SECTION 4: EMBEDDED PIEZOELECTRIC SENSORS IN MIL COMPOSITES

Introduction

Many of the existing embedded sensor concepts have been applied predominantly to polymer materials (e.g. [1, 2]). One of the primary reasons for the popularity of polymer matrices from the point of view of embedding sensors is that the polymers offer the advantage of low processing temperatures (maximum 300-400°C). Consequently, one does not have to generally worry about damaging the sensors (except polymeric sensors such as piezoelectric PVDF) or degrading their performance due to the temperature encountered during the embedding procedure.

On the other hand, embedding sensors within metallic materials invariably requires high temperatures that easily exceed 600°C (e.g. for aluminum matrix) and maybe in the range of ~1000°C (for steels, superalloys etc.). Consequently, only a few researchers have tried to embed sensors within metallic structures. In one approach, Asanuma et al. [3-7] have developed a two-step inter-phase forming/ hot pressing technique to embed glass optical fibers in an aluminum matrix. Although molten aluminum can react with the glass optical fiber, the optical fiber survived the fabrication process since the molten metal (a Cu-Al eutectic) was in contact with the optical fiber for only a short time (5 minutes or so). Further, the best results were obtained when the hot pressing step was carried out in a low vacuum rather than in air. In another approach, Paolozzi et al. [8] used an aluminum-coated optical fiber and embedded it in an aluminum matrix during casting. Again, the optical fiber survived the fabrication process owing to the short duration for which the fiber was in contact with the molten metal.

In the present research, MIL composites were fabricated in open air with the aim of embedding piezoelectric sensors within these composites. As described elsewhere [9, 10], MIL composites are generally fabricated by reacting alternate layers of Ti and Al at temperatures between 660°C and 750°C with the reaction occurring typically over 6-8 hours. The molten Al reacts with Ti to form Al_3Ti, resulting in a final structure comprising alternate layers of residual Ti and Al_3Ti (see Figure 4-1). Clearly, any attempt to embed sensors within such a metallic composite structure needs to ensure that the sensors survive the entire fabrication process that lasts hours instead of

minutes [7, 8]. The motivation for embedding piezoelectric sensors within MIL composites was that a network of piezoelectric sensors could be used to locate external impacts on the structure, such as those caused by projectiles. Additionally, piezoelectric sensors could be connected in an electrical shunt circuit to dissipate the vibration energy of a structure in the form of electrical heating. Although the use of piezoelectric sensors for impact detection [2, 11-13] or energy dissipation [14-17] is not new, the matrix in these as well as in most of the other reports, is polymer based. In the present paper, we will describe techniques to safely process piezoelectric sensors at high temperatures in metals, in the presence of molten aluminum, for extended duration of time, and without damaging the sensors or degrading their performance. The algorithms developed for impact location detection and the results on vibration damping are also described.

Experimental Procedure

Sample Fabrication

The basic materials used in the fabrication of the MIL composite were 0.508 mm (0.020") thick Ti-6-4 alloy sheets and 0.610 mm (0.024") thick 1100 Al alloy sheets. The fabrication of the composite with embedded piezoelectric sensors can be divided into five steps:

Step 1: Several Ti-6-4 alloy sheets and 1100 Al alloy sheets were stacked alternately and reacted to form two MIL composite plates, each approximately 8.255 mm (0.325") thick. This fabrication process has been described in detail elsewhere [9, 10].

Step 2: Four 19.05 mm diameter (0.75") holes were machined out in an un-reacted stack (total height ~3.81 mm (~ 0.150")) of alternately placed Ti-6-4 sheets and 1100 Al alloy sheets. A close-fitting titanium ring, with a hole machined in its wall, was inserted in each of the four holes in the sheets. Rectangular slots were machined in the sheets, adjacent to each of the holes and a steel tube placed in the slot. One end of the steel tube was inserted into the hole in the titanium ring, while the other end of the tube extended outside the stack. Figure 4-2 shows a schematic of the assembly. Thus, at the end of the second step, one has an un-reacted stack of Ti and Al sheets with titanium rings and steel tubes placed in their appropriate locations.

Step 3: The assembly of the second step was compressed in a load frame at ~600°C for several hours to diffusion bond the Ti and Al layers, and then cooled down.

Step 4: The piezoelectric sensors were carefully placed in their respective holes. Individual lead wires of a sensor were passed through a two-hole alumina tube placed within the steel tube (see Figures 4-3a and 4-3b). The sensors are then sealed in the cavity using a high-temperature cement paste (Ceramabond 571, Aremco Products, USA) which is then cured for several hours at room temperature followed by curing at ~100°C.

Step 5: One pre-reacted plate (from step 1) was placed on each side of the stack containing the sensors (step 4), and then processed in the same manner as in step 1. A photograph of the finished sample is shown in Figure 4-4.

The piezoelectric sensors chosen in this work were 36° Y-cut LiNbO3 crystals (Boston Piezo-optics, Massachusetts, USA) since their Curie temperature (~1200°C [18]) is higher than the maximum temperature (750°C) encountered during the fabrication. The crystals were 12.7 mm (0.5") in diameter and 19.81 mm (0.78") tall with a co-axial electrode pattern. In a preliminary experiment, a LiNbO3 crystal was mounted on a steel plate that was then impacted by a steel rod (see Figure 4-5a). The output from the crystal was recorded via digital oscilloscope. Subsequently, the crystal was heated in a furnace and subjected to the temperature profile similar to what it would encounter during the fabrication of the MIL composites. Following this heat treatment, the crystal was remounted on the steel plate and its output recorded for the identical mechanical impulse as before.

Triangulation Algorithm for Impact Location Detection

In the triangulation scheme developed here, the value of the wave speed in the MIL composite plate is not required, but is assumed constant for the purpose of triangulation calculations. The transducer signals were captured by a 4-channel, 25 MHz bandwidth per channel, digital oscilloscope. The triangulation scheme was implemented in a MATLAB script that computes the difference in the arrival times of the signals at the sensors. Instead of manually providing an

initial guess of the impact location, the computer program itself determines an initial guess of the impact location and then iteratively determines the exact impact location. A detailed description the methodology is given in [19].

Vibration Damping using Shunt Circuit

Two types of shunt circuits; resistive and a resistor-inductor-capacitor (RLC) circuit, were investigated for vibration damping of the MIL plate. Each of the four embedded piezoelectric sensors was connected in its individual, but identical, electrical circuit. The mechanical input to the plate was provided by an acoustic speaker. The 3rd damping mode of the MIL plate was analyzed. A detailed description the experimental methodology is given in [19].

Results & Discussion

Figure 4-5b shows the output of a $LiNbO_3$ piezoelectric sensor before and after heat treatment. The sensor output shows that the performance of the $LiNbO_3$ crystals is not degraded after being subjected to high temperature heat treatment used in the present research.   The high Curie temperature of the $LiNbO_3$ crystals was instrumental in ensuring that their piezoelectric performance did not degrade even after exposure to 650-750°C for several hours. The proper height of the titanium ring inserts, as well as the stiff pre-reacted layers placed above and below the cavities, ensured that molten aluminum did not infiltrate the cavities. In initial trials when the cavities were not perfectly sealed, molten aluminum infiltrated the cavities and reacted with $LiNbO_3$ crystals, thus, completely destroying the sensors. Therefore, proper sealing of the cavities is absolutely essential for the success of this process. The high temperature cement, within which the $LiNbO_3$ sensors were encapsulated inside the cavity, acted as a back-up protection against any possible molten aluminum infiltration. The cement also acted as a medium through which the vibrations in the plate were transmitted to the $LiNbO_3$ sensors. Each sensor had two lead wires and each of these wires was passed through a hole in the double-holed alumina tube. This separation of lead wires ensured that the wires never came in contact with each other. The protective steel tube placed around the alumina tube ensured that even if the alumina tube cracked or broke during processing, molten aluminum could not infiltrate the tube and short the lead wires to the rest of the metallic plate. Finally, the load applied to the MIL

plate during processing was substantially lower than the failure strength of the LiNbO$_3$ crystals, thus, ensuring that the crystals did not fracture during processing.

Figure 4-4 shows the finished MIL sample and the locations of the embedded sensors are marked with an "X". Whether the LiNbO$_3$ crystals survived the processing or not was determined by hitting the plate and checking for output from each of the sensors, as well as by checking that the lead wires were electrically isolated from each other and the rest of the plate. The present approach of embedding sensors is more robust than those in the literature [3-8] since the processing temperature is higher and the duration at the high temperature is longer than encountered in the earlier approaches.

Triangulation based algorithm was developed to determine the impact location. Figure 4-6 shows the locations at which the MIL plate was impacted as well as the locations determined via the triangulation scheme. The correspondence between the actual and the calculated locations was quite good and the program was able to determine the impact location within an error of 10%.

RESULTS OF IMPACT LOCATION BY MODAL ANALYSIS FOR MIL?

Based on the analysis of Hagood and van Flowtow [20], the optimum resistor for the resistance shunt circuit that maximizes the damping was calculated to be 3Ω [19]. Similarly, the optimum capacitance, resistance and inductance for the case of a resonant shunt circuit with maximum damping were calculated to be 26.93 µF, 81 mΩ and 270 µH, respectively [19]. Figure 4-7 shows the shape of the 3rd mode of a completely free square plate, which, in the present work corresponds to a frequency of 1856.3 Hz for the MIL plate. Figure 4-8 compares the frequency response function of the MIL plate with and without damping circuit. It can be seen in Figure 4-8 that the MIL plate shows an increase in damping of ~30%, from 0.24% to 0.31%, with the inclusion of the piezoelectric sensors in a resistive shunt circuit. On the other hand, the damping ratio increases by ~90%, from 0.24% to 0.46%, if the piezoelectric sensors were, instead, connected in a resonant shunt circuit.

The present research overcomes the two main limitations with regards to embedding sensors in metallic materials; high processing temperature and the presence of molten metal. Owing to the above limitations, most of the embedded sensing work to date has been restricted to polymer composites. The processing techniques developed in this work open the door to embedding sensors within metallic materials, using Ti-Al$_3$Ti metallic-intermetallic composites as an example of the working material. As has been shown in the literature, Ti-Al$_3$Ti MIL composites have excellent mechanical properties [9, 10, 21]. Therefore, Ti-Al$_3$Ti MIL composites are excellent candidates for armor/non-armor structural applications. Additionally, in these applications, a network of embedded sensors within the MIL composites could be used for monitoring the health of the MIL structure, for determining the impact location of incident projectiles in armor applications and for damping the structural vibrations to provide a more "silent" structure.

Conclusions

Robust techniques were developed to embed piezoelectric crystals in metallic-intermetallic laminate composites. The techniques developed ensured that the sensors survived the high-temperature processing as well as were protected against the molten aluminum formed during the processing.

The embedded piezoelectric sensors were successfully used in conjunction with triangulation based algorithm to determine impact locations, thus, opening doors for the MIL composites in armor applications.

The embedded piezoelectric sensors were connected in a resistive shunt or a resonant shunt circuit so as to damp the mechanical vibrations of the MIL plate through electrical joule heating. Compared to the undamped plate, the damping ratio of the MIL plate increased by ~30% and ~90%, respectively, when it was connected in a resistive or resonant shunt circuits with optimized electrical elements.
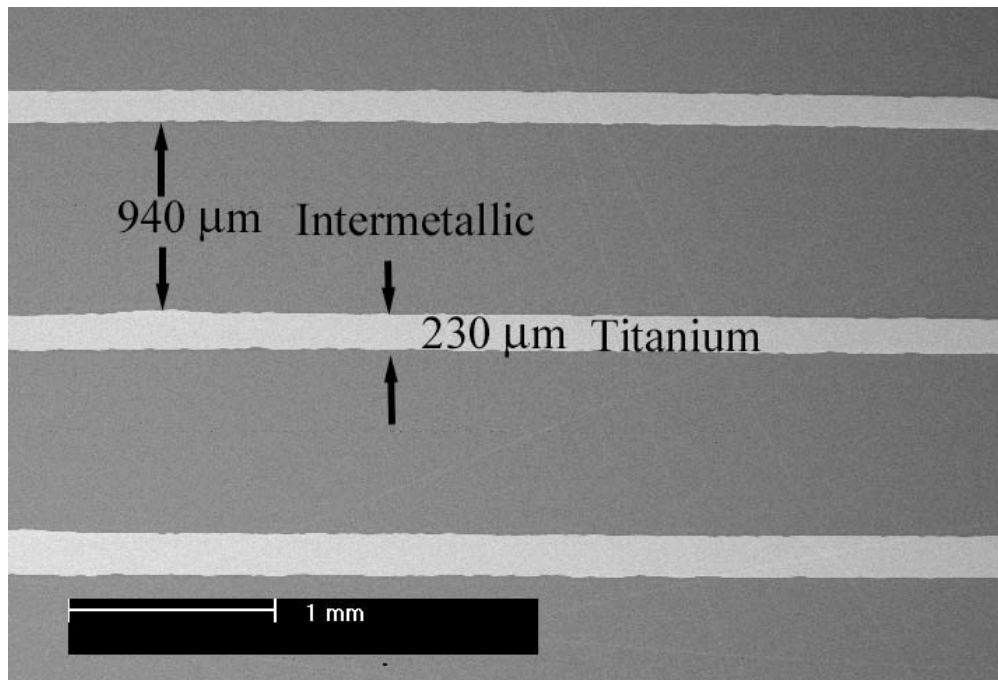
Figure 4-1:   A SEM image of typical TI-Al$_3$Ti metallic-intermetallic laminate (MIL) composite. The dark layers are Al$_3$Ti while the bright layers are titanium.
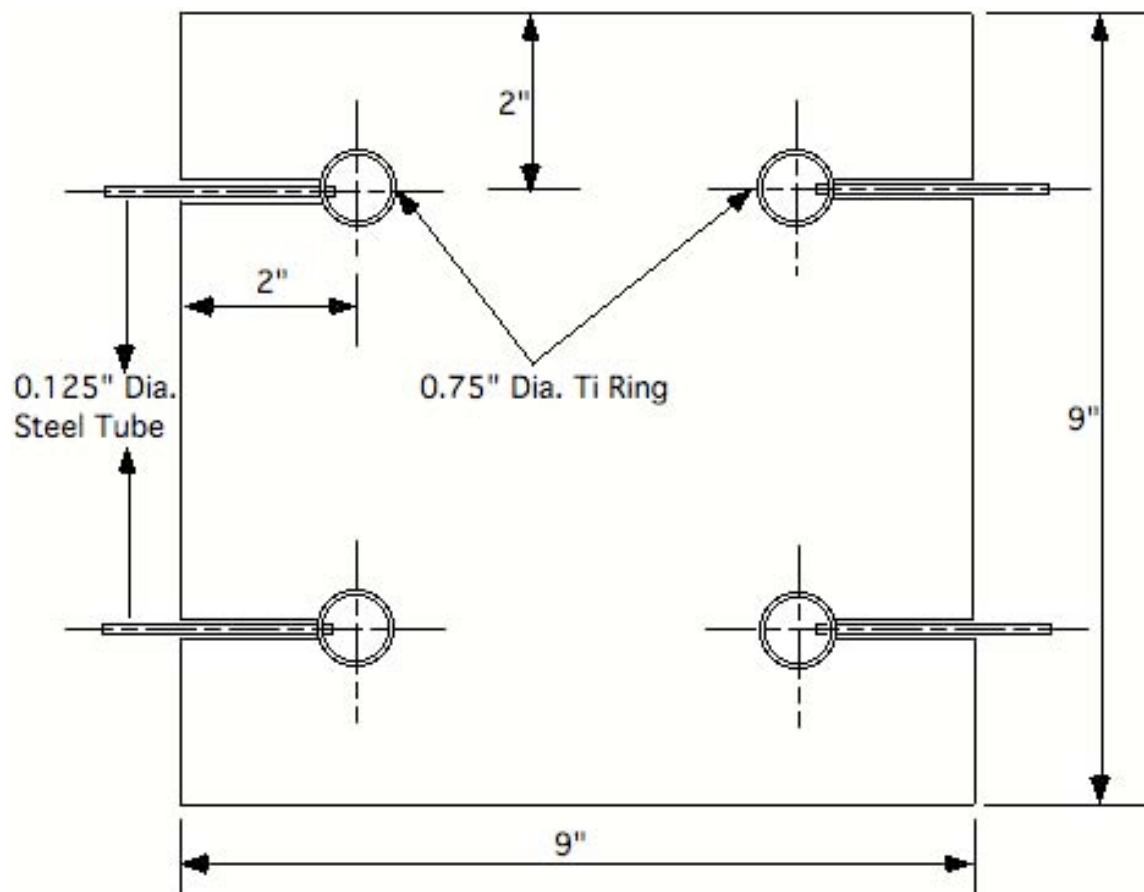
Figure 4-2: A schematic of the sensor layout in the MIL composite.
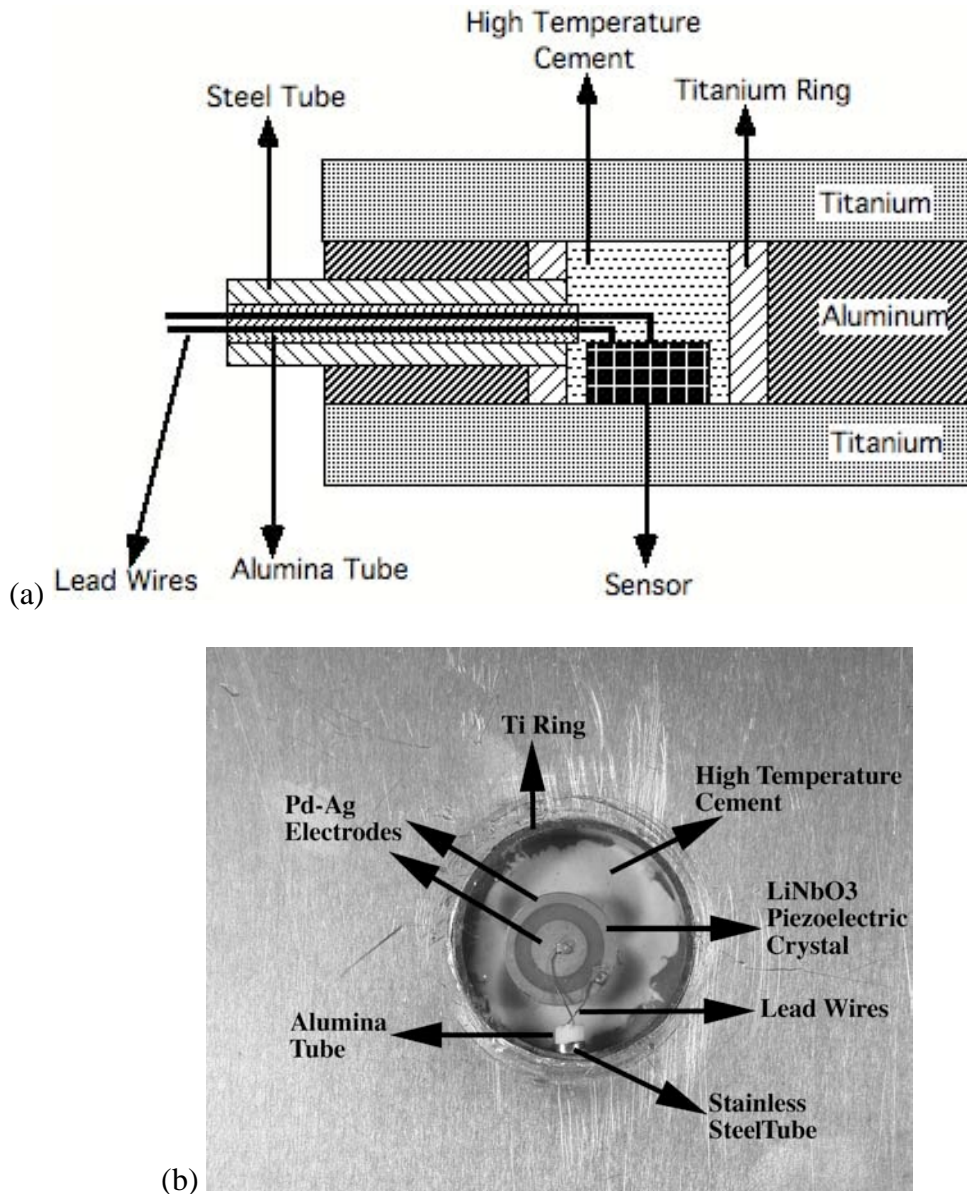
Figure 4-3: (a) A detailed schematic of the cross-section of sensor position within the cavity. (b) A top-view of the sensor within the cavity showing the titanium ring lining the cavity, the lead wires and the protective steel and alumina tubes.

Figure 4-4: A photograph of the finished MIL composite sample with sensors embedded at locations marked with a circle. The electrical leads of each of the sensors, coming out of their respective protective tubes, can be seen.

(a)

(b)
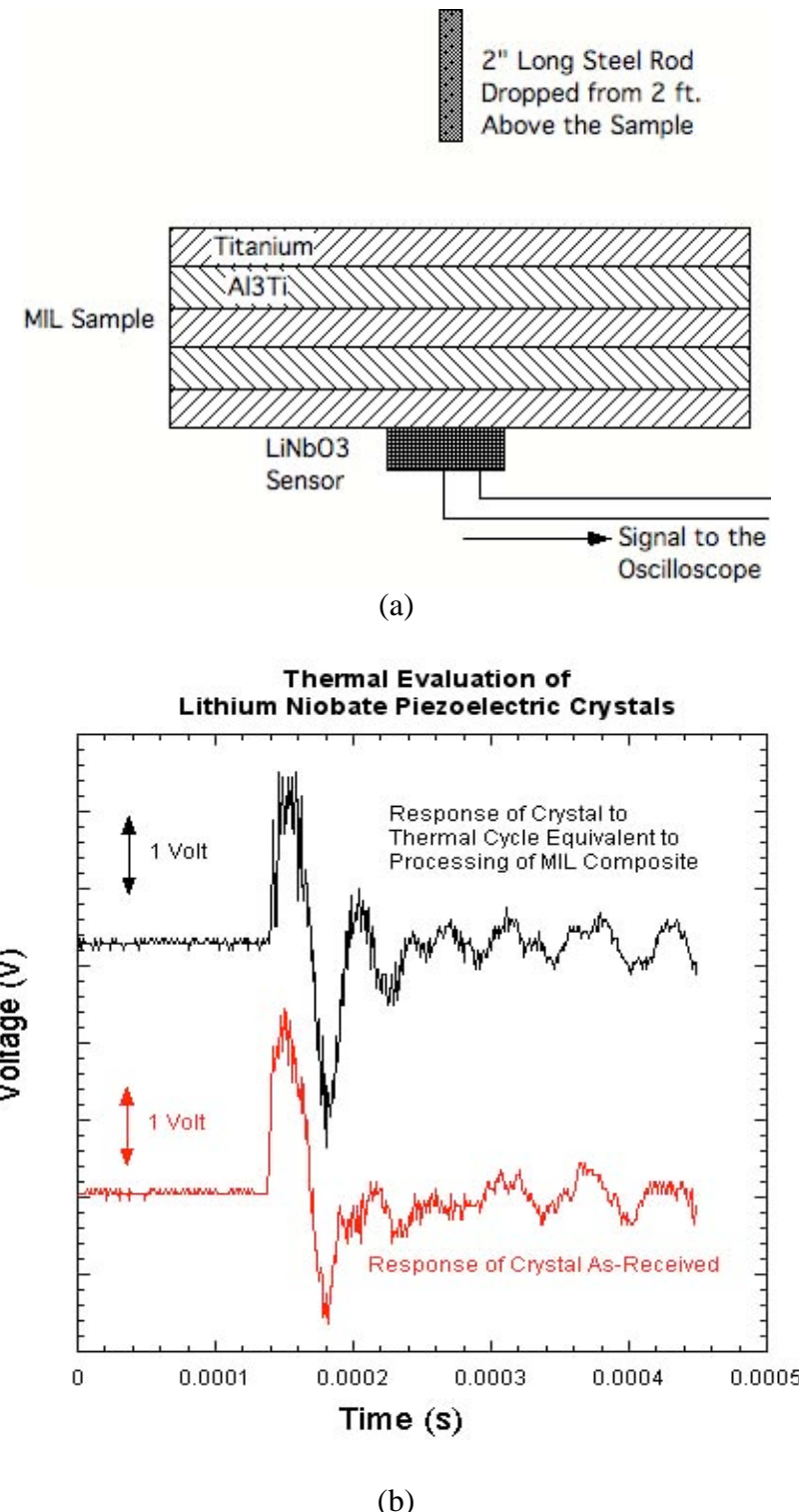
Figure 4-5:   (a) A schematic of the setup to check the output response of a piezoelectric sensor in the as-received condition and after exposing it to high temperature.   (b) Response of the piezoelectric sensor before and after exposure to high temperature.
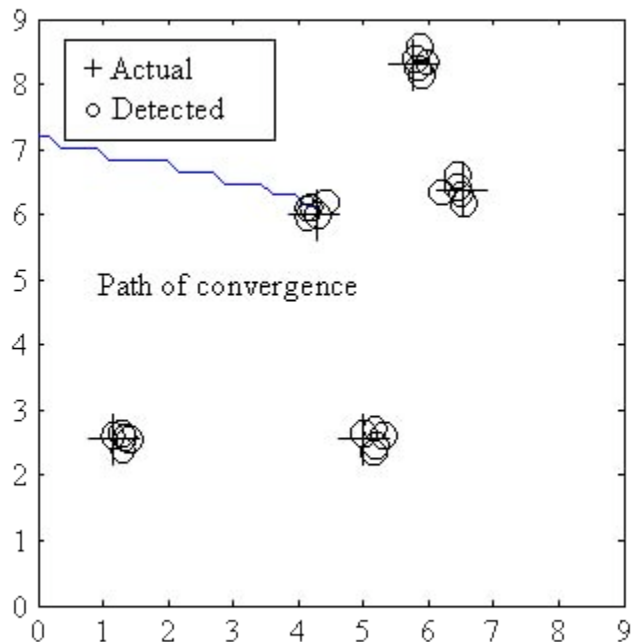
Figure 4-6.   Results of the determining impact location on the MIL plate via the triangulation scheme.

(a)

(b)

(c)
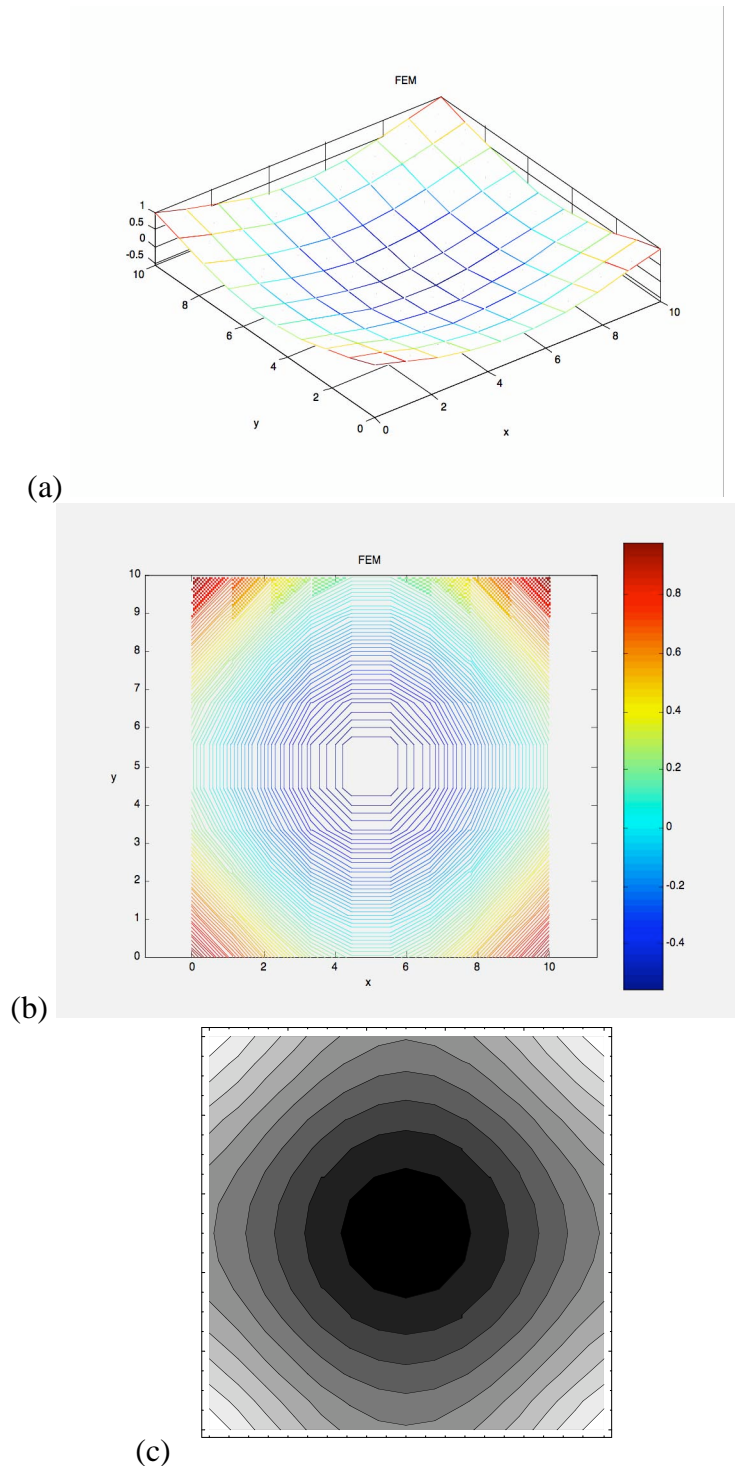
Figure 4-7. The 3rd mode shape of a completely free square plate: (a) FEM calculation, (b) numerical approximation based on FEM results, and (c) least squares approximation.
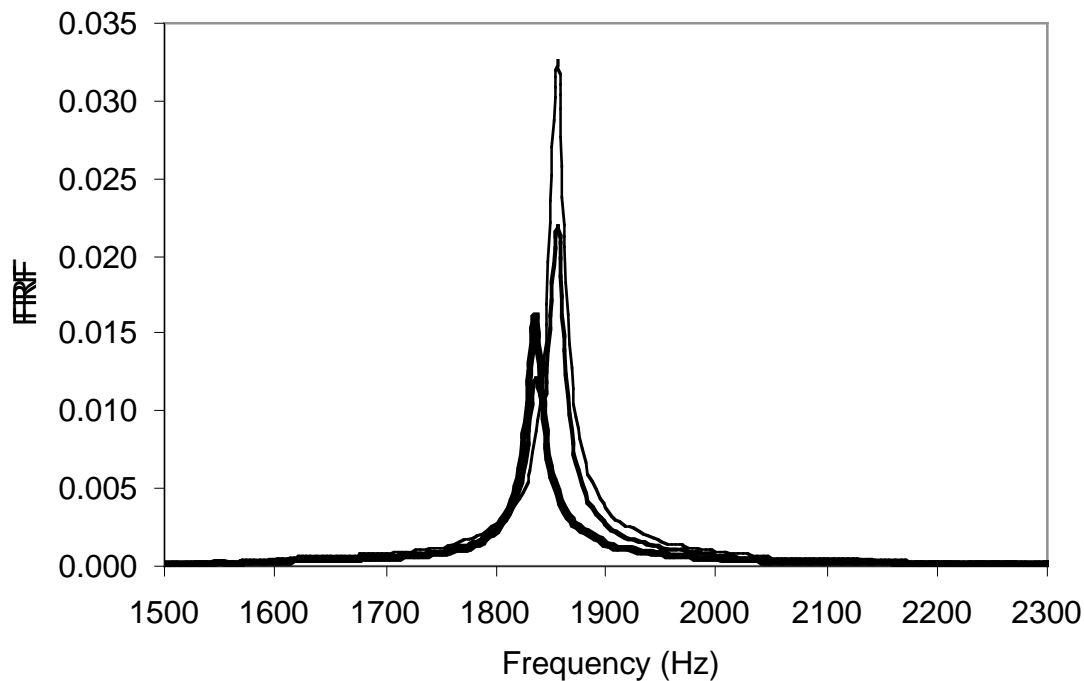
Figure 4-8. Frequency response functions of the MIL plate at Mode 3. The damping factor, ζ, is listed for each the experimental conditions; without any damping, with resistive shunt and with resonant shunt damping.

REFERENCES TO SECTION 4

1. Paolozzi A, Ivagnes M, Lecci U. In: 2nd International Workshop on Structural Health Monitoring, edited by Chang F-K, Proc. Conf. held in Stanford, CA, USA, 1999, 661, Technomic Publishing Co., Inc., Lancaster, PA, USA.

2. Seydel RE, Fu-Kuo C. In: SPIE-Int. Soc. Opt. Eng. Proceedings of Spie - the International Society for Optical Engineering, vol.3668, pt.1-2, 1999, pp.295-305. USA., Proc. Conf. held in Newport Beach, CA, 1999, 225,

3. Asanuma H. Journal of Metals 2000;52:21.

4. Asanuma H, Du H. In: Smart Materials and Structures. Proceedings of the 4th European Conference on Smart Structures and Materials in conjunction with the 2nd International Conference on Micromechanics, Intelligent Materials and Robotics. IOP Publishing. 1998, pp.629-34. Bristol, UK., edited by Tomlinson GR, Bullough WA, Proc. Conf. held in Harrogate, UK, 1998, 629, IOP Publishing.

5. Asanuma H, Kishi T, Ichikawa K, Du H, Maeno K, Prat C, Chandra T, Yu D. In: THERMEC'97, International Conference on Thermomechanical Processing of Steels and Other Materials., edited by Chandra T, Sakai T, Proc. Conf. held in Wollongong, NSW, Australia, 1997, 1177, TMS, Warrendale, PA, USA.

6. Asanuma H, Ichikawa K, Kishi T. Journal of Intelligent Material Systems & Structures 1996;7:307.

7. Asanuma H, Hirohashi M, Ichikawa K, Hao D. In: Proceedings of SPIE - the International Society for Optical Engineering, Proc. Conf. held in San Diego, CA, USA, 1995, 396, SPIE, USA.

8. Paolozzi A, Felli F, Caponero MA. In: 2nd International Workshop on Structural Health Monitoring, edited by Chang F-K, Proc. Conf. held in Stanford, CA, USA, 1999, 257, Technomic Publishing Co., Inc., Lancaster, PA, USA.

9. Harach DJ, Vecchio KS. Metallurgical and Materials Transactions A 2001;32A:1493.

10. Rohatgi A, Harach DJ, Vecchio KS, Harvey KP. Acta Materialia 2003;51:2933.

11. Dupont M, Osmont D, Gouyon R, Balageas D. In: SPIE-Int. Soc. Opt. Eng. Proceedings of Spie - the International Society for Optical Engineering, vol.3668, pt.1-2, 1999, pp.561-570. USA., Proc. Conf. held in Newport Beach, CA, 1999, 561,

12. Osmont D, Dupont M, Gouyon R, Lemistre M, Balageas D. In: SPIE-Int. Soc. Opt. Eng. Proceedings of Spie - the International Society for Optical Engineering, vol.4073, 2000, pp.130-7. USA., Proc. Conf. held in 2000,

13. Osmont D, Dupont M, Gouyon R, Lemistre M, Balageas D. In: SPIE-Int. Soc. Opt. Eng. Proceedings of Spie - the International Society for Optical Engineering, vol.3986, 2000, pp.85-92. USA., Proc. Conf. held in 2000,

14. Bohua S, Da H. Composite Structures 2001;53:437.

15. Wang SY, Quek ST, Ang KK. Smart Materials & Structures 2001;10:637.

16. Yang SM, Jeng CA. Smart Materials & Structures 1996;5:806.

17. Yang SM, Bian JJ. Smart Materials & Structures 1996;5:501.

18. Culshaw B. Smart Structures and Materials, Boston: Artech House, 1996. p.49.

19. Nguyen PH, Improving Structural Functionality Using Embedded Components, Master's thesis, University of California, San Diego, San Diego, 65, (2003).

20. Hagood NW, von Flotow A. Journal of Sound & Vibration 1991;146:243.